

200

## LIBRARY Michigan State University

This is to certify that the dissertation entitled

## FORWARD AND INVERSE MODELING USING MESHLESS METHOD FOR NDE APPLICATION

presented by

**XIN LIU** 

has been accepted towards fulfillment of the requirements for the

Ph.D.	degree inElectrical Engineering	
	Major Professor's Signature	
	Major Professor's Signature	-
	Ang 24, 2009	
	Date	

MSU is an Affirmative Action/Equal Opportunity Employer

PLACE IN RETURN BOX to remove this checkout from your record.

TO AVOID FINES return on or before date due.

MAY BE RECALLED with earlier due date if requested.

DATE DUE	DATE DUE	DATE DUE
	OCT 2 5 2011	
	500 4 5	

5/08 K:/Proj/Acc&Pres/CIRC/DateDue.indd

# FORWARD AND INVERSE MODELING USING MESHLESS METHOD FOR NDE APPLICATION

By

Xin Liu

#### **A DISSERTATION**

Submitted to
Michigan State University
in partial fulfillment of the requirements
for the degree of

**DOCTOR OF PHILOSOPHY** 

**Electrical Engineering** 

2009

#### **ABSTRACT**

# FORWARD AND INVERSE MODELING USING MESHLESS METHOD FOR NDE APPLICATION

Bv

#### Xin Liu

Nondestructive Evaluation (NDE) methods are used extensively in industry in inspecting and maintaining product quality. As new NDE sensors and systems are developed for new applications, the availability of a theoretical model that can simulate the system performance is extremely important for understanding the underlying physics and optimizing the system parameters. For most real world problems, where analytical solutions are not available, various computational methods have been developed. Among these, Finite Element Methods (FEM) are well known and used extensively for computing static and quasi-static electromagnetic fields associated with NDE applications. FEM offers a robust model, and the simulation results using fast solvers are stable and accurate. One of its disadvantages is the need for a computational mesh. Most of the test geometries in NDE are complex and high dimensional, and mesh construction in FE models is an extremely labor intensive and time consuming process. Furthermore, in electromagnetic problems that involve geometrical discontinuities and propagating tight cracks, the use of an underlying mesh creates difficulties in the treatment of discontinuities and decreases the accuracy of simulation results.

A major contribution in this dissertation is the development of Element-Free Galerkin (EFG) model, for NDE applications, which belongs to the newly developed class of Meshless Methods that do not involve the use of a mesh for discretizing the domain. Several improvements to the basic EFG model are proposed for electromagnetic field computations. One, two, and three-dimensional (1D, 2D, and 3D) models for Poisson and diffusion equations, describing static or low frequency quasi-static problems, are presented as examples to illustrate the validity of the EFG method. The model is also applied to real world problems for electromagnetic field calculations in aircraft skin inspection and the simulation results clearly demonstrate the feasibility and advantage of the method.

The implementation of EFG method for solving the inverse problem is also presented. The objective of the inverse problem is to estimate parameters characterizing defect profile, including location, size, and shape, based on the NDE measured signals. New formulations for model based inversion using EFG method as forward model is developed in this dissertation. 1D parametric and 2D non-parametric inversion techniques using State Space search and gradient-based search method are presented along with preliminary results on simulated data. The major advantage of EFG technique over FEM in inverse problem solutions is the elimination of re-meshing in each iteration, which saves computational time while maintaining accuracy of solutions.

The challenge of high dimensionality in 3D inverse problems is also addressed by extending the iterative State Space search approach described for 2D problems. Preliminary results validating these modifications are presented.

To my husband, daughter, and parents

#### **ACKNOWLEDGEMENTS**

I would like to express my sincere appreciation to Dr. Lalita Udpa for her continuous guidance and encouragement throughout my Ph.D study. I am grateful for her intellectual, financial support, inspiration, invaluable advice, and all the trust that helps me to get into and survive in the world of engineering. Dr. Lalita Udpa teaches me everything, from the basic English writing to the attitude and passion in research. Dr. Lalita Udpa is a lifelong role model in my professionalism.

I would like to express my sincere gratitude to my committee members: Dr. Satish Udpa, Dr. Fang Z. Peng, and Dr. Neil Wright for taking the time to serve on my committee and for providing invaluable comments and suggestions to enhance the quality of the dissertation.

I would like to express my gratitude to all my collaborators for the helpful discussion, guidance, providing data and samples. I thank each person related to this work directly or indirectly for the successful completion of the dissertation.

I would particularly like to thank my husband and colleague, Dr. Yiming Deng for his support, encouragement, and love. I would like to thank my beloved parents, all my friends and colleagues in NDEL. Thank you!

## **TABLE OF CONTENTS**

LIST	LIST OF TABLES		viii
LIST	OF FIG	URES	ix
CHA	PTER 1.	INTRODUCTION	1
1.1	Introduc	tion to Nondestructive Testing	1
1.2	Eddy Cu	urrent Testing	2
1.3		and Inverse Problems	
1.4	Need for	r Modeling	7
1.5	Introduc	tion to Meshless Methods	10
1.6	Research	h Objectives	12
		BASIC ELECTROMAGNETICS FOR EDDY	
CURI	RENT M	ODELING	15
2.1	Introduc	tion	15
2.2		l's Equation	
2.3		armonic Fields and Potential Functions	
2.	3.1 Magn	etic Vector Potential	17
2.	3.2 Electr	ic Scalar Potential	17
2.4	Weak Fo	orm and Galerkin Method	18
CHA	PTER 3.	ELEMENT FREE GALERKIN METHOD	21
3.1	Introduc	tion	21
3.2		Least Square Approximation	
3.3		ry Conditions	
3.4		Function	
3.5		nuities Approximation	
3.6	The Ortl	hogonal Basis	33
CHA	PTER 4.	FORWARD MODEL VALIDATION	38
4.1	Introduc	tion	38
4.2		lem	
4.3		lem	
CHA	PTER 5.	FORWARD MODEL IMPLEMENTATION	47
5.1	Introduc	tion	47

5.2	Mathematical Formulation	
5.3	Magneto Optic Imaging Application	50
5.3.	1 Introduction to MOI in Airframe Inspection Application	51
5.3.		
5.3.	Numerical Results I – Fastener hole without crack	57
5.3.	4 Numerical Results II - Fastener hole with 5 mm second layer tight crack	60
5.3.	· · · · · · · · · · · · · · · · · · ·	
CHAP.	TER 6. INVERSE PROBLEM USING EFG METHOD	.65
6.1	Introduction	
6.2	1D Problems – Parametric Approach	
6.2.		
6.2.		
6.2.		
6.3	Inversion based on State Space Search Techniques for 2D Problem	
6.3.	<b>▲</b>	
6.3.		
6.3.		
6.3.	4 Initial Results	82
6.3.	5 Choice of Cost Function	86
6.3.		
6.4	Inversion based on Gradient Search using Adjoint Equation for 2D Problem	91
6.4.	1 The Inversion Scheme in 2D	92
6.4.	2 Results	95
6.4.	3 Effect of Noise Level	.101
6.4.	4 Conclusion	.108
СНАР	TER 7. 3D INVERSE PROBLEM USING EFG METHOD	109
7.1	Introduction	.109
7.2	Problem Statement	.110
7.3	3D State Space Representation	.111
7.4	Search Procedure	
7.5	The Detailed Search Procedure	.114
7.6	Initial Results	.117
7.7	Conclusion	
СНАР	TER 8. CONCLUSIONS AND FUTURE WORK	126
8.1	Original Contributions to the Field	126
8.2	Future Work	
TO HO HOUSE	DENICES	130
KEPE	RENCES	127

### **LIST OF TABLES**

Table 1 Boundary conditions	56
Table 2 Summary of simulation results	57
Table 3 Summary of simulation results	61

#### **LIST OF FIGURES**

Figure 1.1 A generic NDE system
Figure 1.2 System of eddy current testing
Figure 1.3 The system approach to illustrate the forward and inverse problem
Figure 3.1 EFG coupled with finite elements along essential boundaries
Figure 3.2 Domain of influence (a) circular; (b) square
Figure 3.3 The weight functions over 1D domain of influence
Figure 3.4 The asymmetry of the domain of influence
Figure 3.5 Domain of influence of node adjacent to material discontinuity (rectangula domain)
Figure 4.1 The comparison of exact and EFG solution with 1 <sup>st</sup> , 2 <sup>nd</sup> order polynomia basis
Figure 4.2 The comparison of exact and EFG solution with 3 <sup>rd</sup> order polynomial basis .4:
Figure 4.3 The comparison of exact solution with various order orthogonal basis42
Figure 4.4 Modeling geometry for 2D problem
Figure 4.5 Induced eddy current plot using EFG method by polynomial basis function (a) 1 <sup>st</sup> order (b) 2 <sup>nd</sup> order
Figure 4.6 Induced eddy current plot using EFG method by orthogonal basis function (a 2 <sup>nd</sup> order (b) comparison with Figure 4.5 (a)
Figure 4.7 The convergence rate using polynomial basis and orthogonal basis40
Figure 5.1 (a) The schematic of the MOI system (b) an experimental image 52
Figure 5.2 (a) The MOI 308 system (b) using of MOI system
Figure 5.3 MOI simulation geometry (both for FEM and EFG). (a) 3-D view, (b) 2-D top view and (c) side view of the multilayer plate with a 6mm diameter fastener hole54
Figure 5.4 2D cross-section view of (a) FEM mesh and (b) EFG discretization of the solution domain

Figure 5.5 (a) 3D view, (b) 2D top view and (c) 2D side view of the normal component of
the magnetic flux density with FEM and (d), (e), (f) with EFG5
Figure 5.6 Binary results obtained by thresholding simulation results in Figure 5.5. (a FEM (b) EFG and (c) experimental image
Figure 5.7 (a) 3D view, (b) 2D top view, and (c) 2D side view of the normal componer
of the magnetic flux density with FEM and (d), (e), (f) with EFG6
Figure 5.8 Binary results obtained by thresholding simulation results in Figure 5.7. (a FEM (b) EFG
Figure 6.1 Schematic representation of the iterative approach of the inverse problem6
Figure 6.2 Definition of the defect parameters for 1D crack6
Figure 6.3 Cost function versus (a) $r$ , (b) $z$ and (c) $\theta$
Figure 6.4 Initial guess (dotted line), the true defect (solid line) and the prediction (dashed line). (a) crack perpendicular to the current (b) crack at an angle of 5 degrees with the current direction
Figure 6.5 The EFG model Geometry (a) 3D View (b) cross-section view7
Figure 6.6 Examples of States (Defects)
Figure 6.7 the tree structure
Figure 6.8 (a) Input signal (b) initial guess of top surface defect (c) initial guess of bottor surface defect
Figure 6.9 Candidate defect shapes used in the search in layer 28
Figure 6.10 (a) True defect profile and (b) initial guess of a top surface defect (c) initial guess of a bottom surface defect (d) reconstructed results for top surface defect8
Figure 6.11 (a) True defect profile and (b) initial guess of a top surface defect (c) initial guess of a bottom surface defect (d) reconstructed result for bottom surface defect 8
Figure 6.12 True defect profile (a) top surface (b) bottom surface8
Figure 6.13 Reconstructed top surface defect profiles (a) with old cost function (b) wit new cost function
Figure 6.14 Reconstructed bottom surface defect profiles (a) with old cost function (by with new cost function
Figure 6.15 (a) The desired defect profile. (b) the initial guess9

Figure 6.16 The updating status of the defect profile	99
Figure 6.17 True defect	102
Figure 6.18 The signal corrupted with (a) 5.0%. (b) 10.0%. (c) 15.0%. (d) 25.0%. (f) 30.0% random noise	
Figure 6.19 (a) to (f) The reconstructed defect profile (dashed lines) when the corrupted with (a) 5.0%. (b) 10.0%. (c) 15.0%. (d) 20.0%. (e) 25.0% random noise	. (f) 30.0%
Figure 7.1 The model geometry (a) 3D view, (b) 2D top view and (c) cr view.	
Figure 7.2 3×3 state space in each layer with three sub-state space	113
Figure 7.3 The candidate state space for sub-state in Figure 7.2 (a)	113
Figure 7.4 Plot of estimated defect region using real, imaginary and absolute d	ata,115
Figure 7.5 The ideal signal of Bz (a) real part (b) imaginary part	117
Figure 7.6 Initial guess of a top surface defect (a) cross-section view (b) top vi	ew118
Figure 7.7 Initial guess of a bottom surface defect (a) cross-section view (b) to	p view.119
Figure 7.8 The reconstructed defect profile from top to bottom layer	120
Figure 7.9 The cost function vs. node	122
Figure 7.10 The reconstructed defect profile from bottom to top layer	123
Figure 7.11 The cost function vs. node	124

#### **CHAPTER 1. INTRODUCTION**

#### 1.1 Introduction to Nondestructive Testing

Nondestructive Testing (NDT) or Nondestructive Evaluation (NDE) methods are widely used by a number of industries to control and maintain product quality, prevent catastrophic failure and improve reliability. It can be defined as the assessment of structural integrity of a material or component without any physical damage it [1]. NDT/NDE plays a crucial role in assuring safety and reliability in the operation of aircraft, gas pipeline, bridge, nuclear power plant etc.

These inspection procedures enable us to locate a flaw or defect and also provide information about defect such as size, shape, and orientation. Furthermore, NDE can also be used to characterize material properties. Some of the commonly used NDT techniques include ultrasonic (UT) [2], radiographic [3], electromagnetic (ET), and thermographic [4] etc.

The implementation of NDT includes the major components as illustrated in Figure 1.1 [5]. An input transducer is used to inject energy (excitation source) into the test specimen. The nature of the interaction between the energy and the test specimen is a function of several variables, including the type of the energy, material properties, defects, inhomogeneities and so on. The receiver transducer will capture the response of the material-energy interaction and the resulting signal is processed, recognized and analyzed to determine the existence and the properties of a defect in the test specimen.

1

A number of energy sources including electromagnetic, ultrasonic and thermographic have been extensively used in a variety of applications. Commonly used electromagnetic techniques for NDT include magnetic flux leakage [6] and eddy current methods [7]. Eddy current methods have been widely used to detect cracks, seams, pits and other surface and subsurface flaws in conducting test specimen. This dissertation mainly focuses on electromagnetic methods which are based on principles of eddy current testing described in the next section.

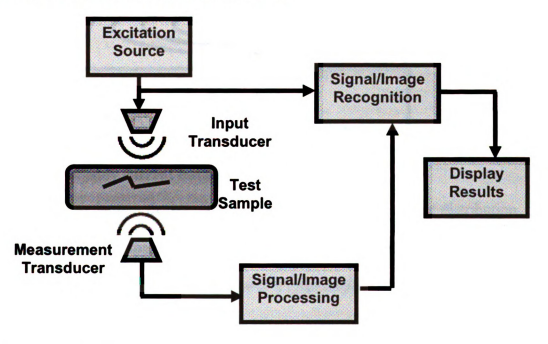


Figure 1.1 A generic NDE system

#### 1.2 Eddy Current Testing

Eddy current testing (ECT) is an electromagnetic technique and based on Michael Faraday's laws of electromagnetic induction discovered in 1831. A conventional eddy current testing system is shown in Figure 1.2 [8]. It includes a coil or a set of coils

excited by a time varying current. The time varying magnetic field generated induces eddy currents inside the conducting specimen (Faraday's Law). The eddy current also generates a magnetic field (Ampere's Law) which opposes the field produced by the source current (Lenz's Law).

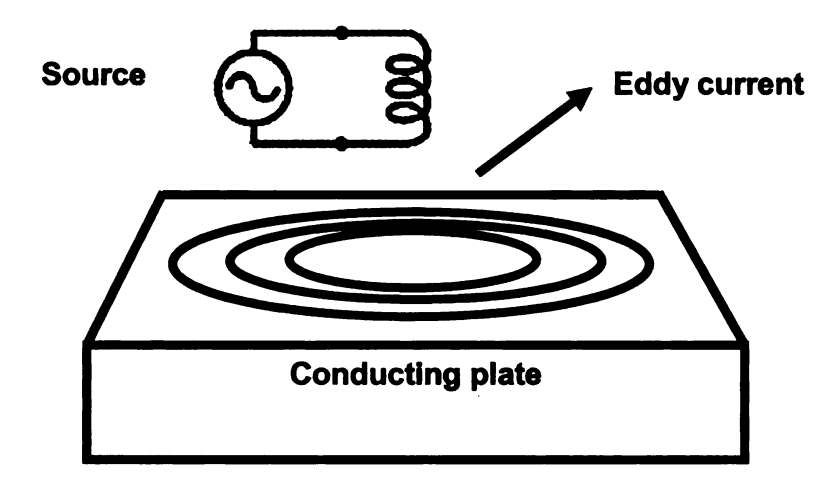


Figure 1.2 System of eddy current testing

The existence of defects in the test specimen changes the eddy current distribution which in turn alters the net magnetic flux linking the coil. Consequently the presence of a defect is detected as a change of the probe coil impedance [8].

Eddy current techniques are widely used in the inspection of aircraft structures composed of aluminum layers for detecting hidden cracks and corrosion. A major limitation of eddy current inspection technique is it can detect only surface or near surface defects because of the skin effect, which is related to the depth of penetration of fields. It can be shown that the eddy current density is maximum on the surface and decays with the depth inside the conducting plate. The amplitude of fields at a depth x could be expressed as

$$A_{x} = A_{0}e^{-\frac{x}{\delta}} \tag{1.1}$$

where  $A_0$  is the amplitude of field on the surface of an infinite conducting plate.

And  $\delta$  is the skin depth given by [9]

$$\delta = \sqrt{\frac{1}{\pi f \sigma \mu}}$$

(1.2)

 $\sigma$ : the conductivity of the plate.

 $\mu$ : the permeability of the plate.

f: the frequency of the excitation.

The eddy currents are affected by the test specimen and experimental operating conditions. The test specimen parameters that vary with electrical conductivity, magnetic permeability, thickness, shape etc. The experimental operation conditions include the design of the excitation coil, operating frequency, lift-off and so on. Several variations of the basic ECT have been developed in recent years. The newly developed inspection methods based on ECT are Magneto Optic Imaging (MOI) and Giant Magneto-Resistance (GMR) sensor which essentially are sensors that can measure the fields associated with induced currents. Details of these two techniques are provided in the next chapter.

#### 1.3 Forward and Inverse Problems

In NDE, forward and inverse problems are two essential areas of research. The forward problem involves simulating the system performance given an excitation source and predicting the measured signal on a flawed test specimen. In contrast, the inverse problem involves estimating the defect parameters based on the information in the measured signal [10], [11], [12].

A systems approach to illustrate both the forward and inverse problems is shown in Figure 1.3 [13]. In Figure 1.3 (a), the input and the system transfer function are known, and the output is to be determined, which is forward problem. In Figure 1.3 (b), the system and output are known, and the input is to be determined, which is the problem of signal inversion. One approach is to assume a set of possible input (defects) as a priori, and from the measured output, the true input signal (defect) is estimated using a model based approach or other techniques such as maximum posteriori probability estimation. In Figure 1.3 (c), the input and output are known, but the system is to be determined, which is also an inverse problem also known as system identification problem.

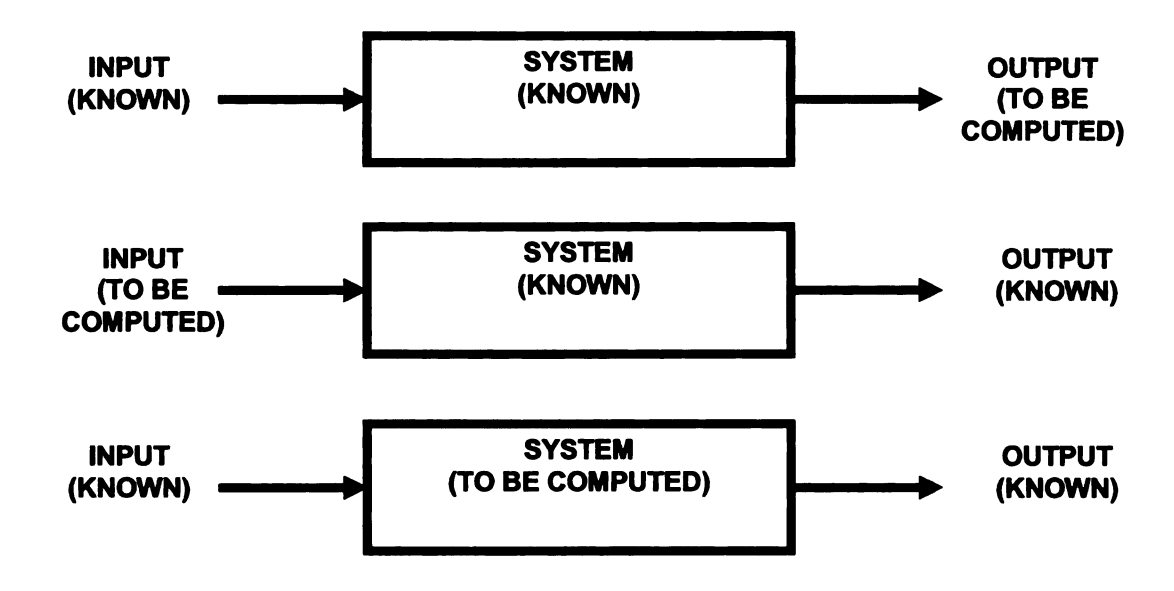


Figure 1.3 The system approach to illustrate the forward and inverse problem

The mathematical term of well-posed problem starts from a definition given by Hadamard [14] by the following three properties:

- (a) Existence: there exists a globally-defined solution for all reasonable data.
- (b) Uniqueness: the solution is unique.
- (c) Continuity (stability): which means the solution depends continuously on the given input data.

A problem which is not well-posed is defined to be ill-posed.

Generally, the well-posed forward problems will lead to the availability of a stable accurate solution. While, the inverse problems are often ill-posed, which means the measured signals lacks the continuous and reliable dependence on the defect profiles, non-uniqueness is a major issue to be concerned, which means a measured signal can correspond to more that one defect profiles. These challenges lead to the development of various constrained techniques to find the optimal inverse solution from the set of

possible solutions. Both the details of the forward problem and inverse problem will be described in the following chapters.

#### 1.4 Need for Modeling

Research in both forward and inverse problem depends strongly on the availability of a good forward model that can simulate the system performance. Firstly, the model is useful in visualization the material-energy interaction which is important for us to understand the underlying physical principles. Secondly, by providing quantitative values of field distribution, a numerical model can be used to adjust and improve the system parameters such as operating frequency, excitation source, sensor, probe parameters and so on. Thirdly, when the measured signal is not available or not adequate, the output of the forward model can be substituted for training data in developing signal inversion schemes.

The main uses of computational models are summarized below:

- 1. Solve forward problem
- 2. Understand the underlying physics of material-energy interaction
- 3. Visualize fields, such as induced currents, reflected waves
- 4. Optimize the system design and operational parameters
- 5. Testbed for generating defect signatures
- 6. Model based probability of detection (POD) estimation
- 7. Model based inverse problem

All electromagnetic phenomena, including ECT, are best described using Maxwell's equations. The nature of NDE applications leads to problems with high dimensionality, nonlinear material properties and complicated solution domain and boundary. Often, these problems involve dynamic geometries and the solution may be a function of time and position. These complications have led to development of various types of models, which include analytical and numerical modeling.

Analytical modeling derived from Maxell's equations played an important role before the development of computers. Today, the computer aided analytical modeling is also valuable for validation based on some assumptions for simplification. The drawback is that analytical approaches can only handle simple domain geometries and hence have limited applications.

In contrast, numerical modeling can simulate problems with complex geometries, high dimensionality, nonlinear, anisotropic and inhomogeneous material properties.

Numerical models, by virtue of the massive time and memory resources of computers are far more powerful than the analytical models.

Recently, the development and implementation of the numerical modeling have become a major research focus in NDE [15]. Several numerical modeling methods have been developed for solving different governing equations, such as Finite Difference Method (FDM), Finite Element Method (FEM), Boundary Element Methods (BEM), Boundary Integral Methods (BIM) and Volume Integral Methods (VIM). Each method has its own advantages and limitations and is appropriate for different kinds of numerical problems [7], [16], [17], [18].

FDM is the simplest numerical modeling method to solve partial differential equations (PDE). The advantage is its relatively ease and simple form for replacing the partial derivatives by appropriate difference formulation. It is widely applied for direct current, quasi-static, transient fields, and linear problems. The limitation is that FDM has poor convergence property for irregular geometries due to its regular discretization. Also, it is rather difficult to model distributed parameters such as the current densities, conductivities and permeability [18].

FEM evolved in the late 1950s as a numerical technique in structural analysis and quickly developed as a major numerical modeling method in various engineering fields to solve PDE [19], [20], [21]. Because of its accuracy and efficiency in modeling, it was applied to electromagnetic NDE in late 1970s, especially for direct current, low frequency fields, and permanent magnet problems [7]. Compared with FDM, FEM has many advantages including its ease to impose the essential boundary conditions and model complex geometries. FEM can handle higher order approximation and lead to faster convergence and better accuracy. FEM has already been developed for various 2D and 3D eddy current NDE problems [8]. The drawbacks of FEM include large computer resources needed, especially for nonlinear and time-dependent problem. Also, it is not well suited for open region problems [16].

Differential equations are commonly used for describing low frequency

electromagnetic field problems, such as electrical machines and eddy current testing. However, in the area of antennas and electromagnetic wave propagation, integral equations [22], [25] are more commonly used. BEM and VIM methods are based on the integral equations [16], [17].

BEM solves Maxwell's equations by using the given boundary conditions to discretize the surface in integral equations, rather than calculating all the values in solution domain. In the post-processing, the integral equation is used again to calculate the required physical quantity at any point in the solution domain. Hence BEM is more efficient than other models with regard to computer resources and ensures good accuracy of solutions. It can be used to solve the fields in linear homogeneous problems when the Green's function is available. The drawback is that its global stiffness matrix is a full matrix in contrast to sparse banded matrix encountered in FEM, and hence requires more computational time [16].

In the case of inhomogeneous and nonlinear problems, VIM is generally introduced to discretize the volumetric domain before solution. In VIM, the field is determined at a point by summing the effects of the sources at all points, convolved with the Green's function. The advantage is it only necessary to construct a mesh over the test sample and solve for the currents in the test sample. But this method also require the Green's function for the problem to be available and its global stiffness matrix is a full matrix instead of banded matrix in FEM, which requires more computational time for solver [17].

#### 1.5 Introduction to Meshless Methods

The traditional FEM is a well established technique that has been successfully applied to ECT modeling. The fundamental idea in FEM is to approximate a continuous function over the entire solution domain by piecewise continuous

approximations, usually polynomials, over a set of sub-domains called finite elements (FE). The interconnecting structure of the elements via nodes is called a finite element mesh. The reliance of FEM on a mesh leads to some characteristic disadvantages. Generation of a mesh for a complex 3D geometry is generally difficult and time consuming [26]. For example, in electromagnetic problems that involve geometrical discontinuities and propagating tight cracks, the use of a dense underlying mesh leads to a high dimensional matrix equation and large computational error.

In recent years, an alternate numerical approach, known as meshless method [26] has been developed that eliminates some of the disadvantages of FEM. In meshless methods, the unknown function is approximated entirely in terms "local" functions defined on a set of nodes. In this approach, elements and the usual relationship between nodes and elements are not necessary to construct a discrete set of equations, which obviates the need for generating a mesh in the solution domain. Consequently meshless methods are especially useful in the problems with discontinuities or propagating cracks.

The initial idea of meshless methods dates back to the smooth particle hydrodynamics (SPH) method for modeling astrophysical phenomena [27] (Gingold and Monaghan, 1977). The research into meshless methods has become very active after the publication of the Diffuse Element Method [28] by Nayroles, Touzot & Villon (1992). Several so-called meshless methods, including: Element Free Galerkin (EFG) by Belytschko, Lu, and Gu (1994); Reproducing Kernel Particle Method (EKPM) [29] by Liu, Chen, Uras, and Chang (1996); the Partition of Unity Finite Element Method (PUFEM) [30] by Babuska and Melenk (1997); hp-cloud method

[31] by Duarte and Oden 1996; Natural Element Method (NEM) [32] by Sukumar, Moran, and Belytschko (1998); Meshless Galerkin methods using Radial Basis Functions (RBF) [33] by Wendland (1999) have also been reported in the literature. The major differences in meshless methods come from the techniques used for interpolation.

The principal attractive features of meshless methods for NDT are the possibility of:

- (i) Working with a cloud of points that describes the underlying structure exactly instead of relying on a tessellation of the domain in forward problems
- (ii) Lack of need for remeshing in solving inverse problems or probe scanning Element-Free Galerkin Method (EFG) is one kind of meshless methods, which employs moving least square approximation with Galerkin formulation. The EFG method is now widely applied to problems in fracture mechanics and electromagnetics [26], [33].

#### 1.6 Research Objectives

The major objective of this dissertation is the development of an efficient numerical model based on the EFG method for solving the forward problem and a scheme for model-based solution of the inverse problem. Although the EFG method is shown to be convenient and robust in electromagnetic field calculations, the theoretical basis is not completed developed. Some improvements to the basic EFG

method are proposed and discussed for enhancing accuracy of solutions to forward problems. Our preliminary 1D, 2D and 3D results of the improved EFG formulations are shown to be promising. These improvements include:

- Selection of weight function and the regularity of the influence radius of the nodes [41]
- 2. Selection of orthogonal basis functions [42]
- 3. Effect of different formulations for applying boundary conditions and the formulation of the penalty function [43]
- 4. Treatments of discontinuities in the interface with visibility criterion [34]

Using the forward EFG model, new approaches for solving inverse problems are also developed in this dissertation. The major advantage of using EFG model in inverse problems is that re-meshing at each iteration is eliminated resulting in reduced computational time and increased accuracy of solutions.

The inversion schemes implemented in this work are:

- 1. 1D parametric inversion of tight cracks
- 2. 2D nonparametric inversion based on state space search
- 3. 2D nonparametric inversion based on gradient search
- 4. 3D nonparametric inversion based on modified state space search

The dissertation consists of the following chapters. Chapter 2 briefly introduces the necessary electromagnetic theoretical background. Chapter 3 describes the formulation and improvements of the forward EFG method in details. Chapter 4 shows results of 1D and 2D model validations of the EFG method in electromagnetic modeling problems. Chapter 5 presents the 3D implementations of the EFG method in

simulating MOI and GMR inspections. Chapter 6 includes the introduction of inverse problems and the preliminary numerical results of the application of EFG method for 1D and 2D defect reconstruction. Chapter 7 presents the modifications for the 3D inversion using state space search technique and preliminary results are included for validating the approach. Chapter 8 covers the conclusions and future work.

# CHAPTER 2. BASIC ELECTROMAGNETICS FOR EDDY CURRENT MODELING

#### 2.1 Introduction

A brief introduction to the basic electromagnetic background for the eddy current NDE is presented in this chapter. Eddy current NDE phenomenon is governed by Maxwell's equations.

#### 2.2 Maxwell's Equation

All electromagnetic phenomena, including ECT, are best described using Maxwell's equations. The differential form of these equations is expressed as follows:

$$\nabla \times \mathbf{E} = -\frac{\partial \mathbf{B}}{\partial t} \tag{2.1}$$

$$\nabla \times \boldsymbol{H} = \boldsymbol{J} + \frac{\partial \boldsymbol{D}}{\partial t}$$

(2.2)

$$\nabla \cdot \mathbf{D} = \rho$$

(2.3)

$$\nabla \cdot \mathbf{B} = 0$$

(2.4)

along with the continuity equation derived from equation (2.2):

$$\nabla \cdot \boldsymbol{J} + \frac{\partial \rho}{\partial t} = 0$$

(2.5)

where the variables are:

E: electric field intensity (volt/meter)

H: magnetic field intensity (ampere/meter)

D: electric flux density (coulumn/meter<sup>3</sup>)

B: magnetic flux density (tesla)

J: electric current density (ampere/meter<sup>3</sup>)

 $\rho$ : electric charge density (coulomb/meter<sup>3</sup>)

#### 2.3 Time-Harmonic Fields and Potential Functions

When the excitation energy (source) is varying sinusoidally with time and we are interested in the steady state response, the solution can be considered in the frequency domain and the Maxwell's equations (2.1) and (2.2) can be rewritten in terms of the excitation frequency:

$$\nabla \times \boldsymbol{E} = -j\omega \boldsymbol{B}$$

(2.6)

$$\nabla \times \boldsymbol{H} = \boldsymbol{J} + j\omega \boldsymbol{D}$$

(2.7)

The governing partial differential equation is usually solved in terms of potential functions, which could be the magnetic vector potential and/or the electric scalar potential introduced below:

#### 2.3.1 Magnetic Vector Potential

We define magnetic vector potential A as the following identity:

$$\nabla \cdot \nabla \times \mathbf{A} \equiv 0$$

(2.8)

From equation (2.4) and (2.8), B can be expressed as the curl of magnetic vector potential A.

$$\boldsymbol{B} = \nabla \times \boldsymbol{A}$$

(2.9)

#### 2.3.2 Electric Scalar Potential

The electric scalar potential V is defined by the identity:

$$\nabla \times \nabla V = 0$$

(2.10)

And from equation (2.1) and (2.9), we get:

$$\nabla \times (\boldsymbol{E} + \frac{\partial \boldsymbol{A}}{\partial t}) = 0$$

(2.11)

When combining equation (2.10), we obtain:

$$\boldsymbol{E} = -\frac{\partial \boldsymbol{A}}{\partial t} - \nabla V \tag{2.12}$$

By introducing the definition of the magnetic vector potential and electric scalar potential, the governing equations, can be fully rewritten using an A-V formulation and solved using numerical modeling methods.

#### 2.4 Weak Form and Galerkin Method

The electromagnetic problems discussed in this dissertation are boundary-value problems described by a governing differential equation in a solution domain  $\Omega$ :

$$Lu = f$$
 in  $\Omega$  (2.13)

together with the homogeneous boundary conditions on the boundary S that encloses the domain:

$$\frac{\partial u}{\partial n} = 0 \qquad \text{on} \quad S_1$$

$$u = 0 \qquad \text{on} \quad S_2$$

$$(2.14)$$

(2.15)

where L is a differential operator, f is the excitation source or force function, u is the unknown quantity, and  $S = S_1 \cup S_2$  is the boundary of domain  $\Omega$ . In

electromagnetics, the governing differential equations can range from simple Poission equations to diffusion and scalar/vector wave equations.

Ideally, one desired to obtain an exact solution for the boundary-value problems, while in most practical engineering applications, only approximate solution is tractable. Generally, the approximate solution is defined by the expansion

$$u^{h}(x) = \sum_{j=1}^{n} v_{j} c_{j}$$
(2.16)

where  $v_j$  is the shape function defined over the entire domain,  $c_j$  is the coefficients to be determined, and n is the total number of discretization nodes. In FEM and EFG, u is written as  $u^h = \sum_{i=1}^n \Phi_i u_i$ , where  $\Phi_i$  is shape function and  $u_i$ 

is the nodal value. Substituting  $u^h$  for u in equation (2.13) will result in a nonzero residual of the form

$$r = Lu^h - f \neq 0$$
 in  $\Omega$ 

Instead of solving for  $u^h$  directly, the weak form seeks a solution that satisfies the equation in an average sense, which is called a weak form. Therefore, the optimal approximation for  $u^h$  is the one that reduces the residual r to the least value at all points in domain  $\Omega$ . So a weighted residual form is considered as

$$R_i = \int_{\Omega} w_i r d\Omega = 0 \tag{2.17}$$

where  $R_i$  defines the weighted residual integrals and  $w_i$  is the weighting function.

In Galerkin method, the weighting functions are chosen to be the same as the shape functions used in the approximation expansion. This usually leads to the most accurate solution. Particularly, in FEM and EFG, the weighting function is  $w_i = \Phi_i$ .

So equation (2.17) can be written as

$$R_i = \int_{\Omega} (\Phi_i \cdot L \sum_{i=1}^n \Phi_i u_i - \Phi_i \cdot f) d\Omega = 0$$
(2.18)

Equation (2.18) can be expressed by the linear algebraic equation

$$[G][u] = [F] \tag{2.19}$$

with  $G_{ij} = \int_{\Omega} (\Phi_i \cdot L\Phi_j) d\Omega$  and  $F_i = \int_{\Omega} \Phi_i \cdot f d\Omega$ . [G] is called the stiffness matrix, [F] is the load (or source) vector.

For each local integral, the EFG method involves higher order terms than conventional FEM, which thereby yields more accurate solution.

#### CHAPTER 3. ELEMENT FREE GALERKIN METHOD

#### 3.1 Introduction

In Element free Galerkin method, a set of nodes is used to construct the discrete system of equations approximating the solution. However, in order to implement the Galerkin procedure, it is necessary to compute the integrals over the solution domain; this is done by defining the support of the basis functions using either a set of quadrature points or a background mesh.

Consider u(x) is a continuous function to be approximated. The theoretical foundation of the approximation in the EFG method is the moving least squares (MLS) approximation, which relies on three components: (i) a weight function, (ii) a polynomial basis, and (iii) a set of position-dependent coefficients. The weight function is nonzero only over a small subdomain of a node, which is defined as the domain of influence. The domain of influence plays an important role in the performance of EFG method in terms of accuracy of the solution.

In the following sections, we will present the basic formulation of EFG method using MLS approximation. The modifications developed for efficient implementation of boundary conditions and interface conditions, selection of weight function and use of higher order orthogonal basis functions are discussed in detail.

#### 3.2 Moving Least Square Approximation

The MLS is a method to obtain a differentiable approximate function in the domain using known function values at discrete points through a weighted least squares fit.

In MLS approximation, the interpolant  $u^h(x)$  is given by [34]

$$u^{h}(x) = \sum_{j=0}^{m} p_{j}(x)a_{j}(x) = p^{T}(x)a(x)$$
(3.1)

where m+1 is the number of terms in the basis function,  $p_j(x)$  are monomial basis functions, and  $a_i(x)$  are coefficients that depend on position x.

When x and  $\overline{x}$  are not superposed, Lancaster and Salkauskas (1981) defined the local approximation by:

$$u^{h}(x,\overline{x}) = \sum_{j=0}^{m} p_{j}(\overline{x})a_{j}(x) = p^{T}(\overline{x})a(x)$$
(3.2)

where x is the approximation point,  $\overline{x}$  is a particular node. For example, in two dimensions,  $u^h(x)$  can be expressed in terms of either a linear or a quadratic basis as:

$$u^{h}(x,y) = a_{0}(x,y) + a_{1}(x,y)x + a_{2}(x,y)y$$
 (linear basis)
$$(3.3)$$

$$u^{h}(x,y) = a_{0}(x,y) + a_{1}(x,y)x + a_{2}(x,y)y + a_{3}(x,y)x^{2} + a_{4}(x,y)xy + a_{5}(x,y)y^{2}$$
 (quadratic basis)

(3.4)

The coefficients  $a_j(x)$  are determined by minimizing the weighted error between local approximation and the nodal values  $u_j$ , i.e., by minimizing the following quadratic form:

$$J = \sum_{j=1}^{n} w(x - x_j) (u^h(x, x_j) - u_j)^2$$

$$= \sum_{j=1}^{n} w(x - x_j) [\sum_{i=0}^{m} p_i(x_j) a_i(x) - u_j]^2.$$
(3.5)

Here  $w(x-x_j)$  is a weight function with compact support, n is the number of nodes in the neighborhood of x where the weight function does not vanish. In matrix notation, Equation (3.5) can be rewritten as

$$J = (\mathbf{Pa} - \mathbf{u})^T \mathbf{W}(\mathbf{x})(\mathbf{Pa} - \mathbf{u})$$
(3.6)

where  $u^T = (u_1, u_2, \dots, u_n)$  are the unknowns

$$\mathbf{P} = [p_i(\mathbf{x}_j)]_{m \times n}, \tag{3.7}$$

$$W(x) = diag[w(x - x_1), w(x - x_2), \dots, w(x - x_n)].$$
(3.8)

The minimization of J with respect to a(x) leads to

$$B(x)a(x) - C(x)u = 0,$$
(3.9)

where

$$\boldsymbol{B}(\boldsymbol{x}) = \boldsymbol{P}^T \boldsymbol{W}(\boldsymbol{x}) \boldsymbol{P}, \tag{3.10}$$

$$C(x) = \mathbf{P}^T \mathbf{W}(x). \tag{3.11}$$

It follows that

$$a(x) = B^{-1}(x)C(x)u.$$
(3.12)

Substituting (3.12) into (3.2), and letting  $\bar{x} = x$ , the MLS approximation can be written as

$$u^{h}(\mathbf{x}) = \sum_{j=1}^{n} \Phi_{j}(\mathbf{x}) u_{j}$$
(3.13)

where the shape functions  $\Phi_j$  are given by

$$\Phi_{j}(\mathbf{x}) = \sum_{i=0}^{m} p_{i}(\mathbf{x}) (\mathbf{B}^{-1}(\mathbf{x}) C(\mathbf{x}))_{ij} = \mathbf{p}^{T} \mathbf{B}^{-1} C_{j}$$
(3.14)

# 3.3 Boundary Conditions

In a numerical solution, it is necessary to choose a solution domain with a surrounding boundary to simulate a particular problem. Therefore, it is essential for the numerical model to consider the physical processes in the boundary region. The boundary conditions are very important for the existence and uniqueness of the numerical solutions. Different boundary conditions may result in very different simulation results. Improper sets of boundary conditions may introduce erroneous influences on the simulation system, hence imposing the proper set of boundary conditions is very important.

It should be noted that the shape function derived in equation (3.14) does not satisfy the Kronecker delta criterion at nodal locations: i.e.  $\Phi_j(x_k) \neq \delta_{jk}$ ; therefore,  $u^h(x_j) \neq u_j$ , which means when the MLS approximation is evaluated at a particular point in the space, the value obtained is not the actual value of the field being approximated, although they are related. This makes it difficult to impose essential boundary conditions in EFG. In order to address this, special techniques have been applied such as Lagrange multipliers [34], modified variational principles [44], or coupling with standard finite elements [45] at the boundary. Note that the construction of the shape function is theoretically identical in both two and three dimensions. Although all these techniques are workable, each technique has its own advantages and limitations.

Generally, Dirichlet type boundary conditions can be imposed through the use of Lagrange multipliers. Furthermore, it is the most accurate method for imposing Dirichlet boundary conditions and useful in relatively small problems, such as 1D or smaller 2D geometries, where the cost to solve the problem is not big. But it adds to the complexity in that the resulting stiffness matrix will have an increased size and

will no longer be positive definite or banded, which may lead to slower convergence.

The proof of this statement is shown in the following.

With Lagrange multipliers method for boundary condition, the original linear algebraic equation (2.19) is changed to

$$\begin{bmatrix} G & K \\ K^T & 0 \end{bmatrix} \begin{Bmatrix} u \\ \lambda \end{Bmatrix} = \begin{Bmatrix} F \\ q \end{Bmatrix}$$
(3.15)

with  $G_{ij}=\int_{\Omega}(\Phi_i\cdot L\Phi_j)d\Omega$ ,  $K_{ij}=-\int_{\Gamma}\Phi_i\cdot N_k d\Gamma$ , u is the unknown,  $\lambda$  is the Lagrange multiplier,  $F_i=\int_{\Omega}\Phi_i\cdot fd\Omega$ ,  $q_k=-\int_{\Gamma}N_k\cdot u_0 d\Gamma$ , and  $N_k$  is the shape function associated with the Lagrange multipliers. While the original stiffness matrix G is sparse, positive definite and banded, the new sub-matrix K is a full matrix associated with the boundary elements. So the overall stiffness matrix is no longer positive definite or banded, resulting in an increased number of unknowns and an awkward structure for the iterative solver.

Modified variational principle method can result in a banded equation; it can also reduce the number of unknowns and therefore reduce the computational costs, but it sometimes yields unstable solutions as shown in [47].

In the coupled FEM-EFG [48] approach, the elements are placed around the boundary of the domain as shown in Figure 3.1 [48]. The essential boundary conditions are applied to FEM nodes. In the implementation of this method we use finite elements as background mesh to perform the quadrature of the weak form. In this approach the FEM nodes adjacent to the essential boundaries are already

available and easy to apply boundary condition. The limitation of the coupled FEM-EFG approach is that the modified shape function has a discontinuity in the derivative at the interface, which affects the accuracy.

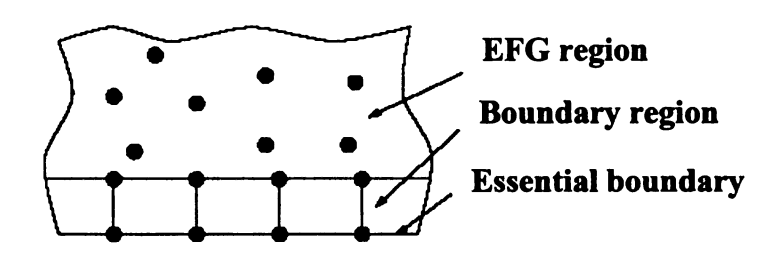


Figure 3.1 EFG coupled with finite elements along essential boundaries

An alternate method based on the constrained variational principle is proposed in this dissertation, which is the penalty function method originally by Suzhen Liu and Qingxin Yang [43]. Consider the typical linear boundary value problem where the linear algebraic equation using EFG method is obtained in the equation (2.19)

$$[G][u] = [F] \tag{3.16}$$

Each element in the final discrete equations with penalty boundary condition is obtained as:

$$G_{ij} = \int_{\Omega} (\Phi_i \cdot L\Phi_j) d\Omega + \alpha \int_{\Gamma} \Phi_i \Phi_j d\Gamma$$
(3.17)

$$F_{i} = \int_{\Omega} \Phi_{i} \cdot f d\Omega + \alpha \int_{\Gamma} u_{0} \Phi_{i} d\Gamma.$$
(3.18)

where  $\Gamma$  is the associated boundary region,  $\alpha$  is the penalty parameter, and  $u_0$  is the boundary value. With the penalty function method, the stiffness matrix is positive definite and banded which translates into a reduced matrix size of the problem.

The selection of penalty parameter has a great effect on the accuracy of solutions. If  $\alpha$  is too small, the boundary condition term is negligible and the boundary condition is not imposed effectively; if  $\alpha$  is too large, diagonal elements corresponding to boundary nodes and some off diagonal elements associated with the boundary nodes become very large making the stiffness matrix ill-conditioned and the convergence slower. Although the penalty methods are very simple to implement,  $\alpha$  much be chosen appropriately.  $\alpha$  is determined to lie typically in the range from  $10^5$  to  $10^{20}$ . Detailed research was conducted on some test problems in the following chapter.

# 3.4 Weight Function

The weight function plays an important role in the performance of EFG method in terms of the accuracy of solutions, complexity of computation (coding) and rate of convergence.

The selection of the weight function within the domain of influence is not restrictive, but it must conform to the following conditions:

- 1. The weight function should be positive valued;
- 2. The weight function should be relatively large for the nodes  $x_i$  close to  $\bar{x}$ ,

and small for more distant nodes. In other words, it should be decrease in magnitude with the distance from  $\bar{x}$  to  $x_j$ .

The weight function is continuous together with its derivatives up to the desired degree.

In the numerical modeling, the solution domain is fully covered by the domains of influence of all nodes. The shape of the domain of influence is arbitrary; a circular or rectangular domain is typically used according to the domain geometry. Figure 3.2 shows two examples of the domain of influences.

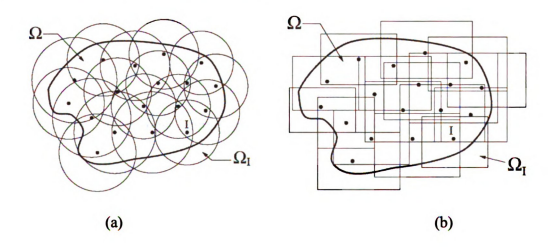


Figure 3.2 Domain of influence (a) circular; (b) square

In a 2D domain of influence, the weight function is derived and expressed at any given point as [40]

$$w(x - x_j) = w_x \cdot w_y = w(r_x) \cdot w(r_y),$$
(3.19)

where  $w(r_i)$ , for i = x, y, are typically either Gaussians, exponentials or cubic splines. These functions take the following form, respectively

$$w(r) = \begin{cases} 1 - e^{-(r-1)^2} & \text{for } r \le 1 \\ 0 & \text{for } r > 1 \end{cases}$$
 (Gaussian),
$$(3.20)$$

$$w(r) = \begin{cases} e^{-(r/\beta)^2} & \text{for } r \le 1 \\ 0 & \text{for } r > 1 \end{cases}$$
 (Exponential),

(3.21)

$$w(r) = \begin{cases} \frac{2}{3} - 4r^2 + 4r^3 & \text{for } r \le \frac{1}{2} \\ \frac{4}{3} - 4r + 4r^2 - \frac{4}{3}r^3 & \text{for } \frac{1}{2} < r \le 1 \\ 0 & \text{for } r > 1 \end{cases}$$
 (Cubic splines),

(3.22)

where  $\beta = 0.5$  yields best convergence for the exponential weight, and  $r_i$ , for i = x, y, are calculated as

$$r_{x} = \left| x - x_{j} \right| / d_{mx} , \quad r_{y} = \left| y - y_{j} \right| / d_{my} ,$$

$$d_{mx} = d_{\max} \cdot c_{x} , \quad d_{my} = d_{\max} \cdot c_{y} .$$

$$(3.23)$$

Figure 3.3 shows one example of weight function over a 1D domain of influence.

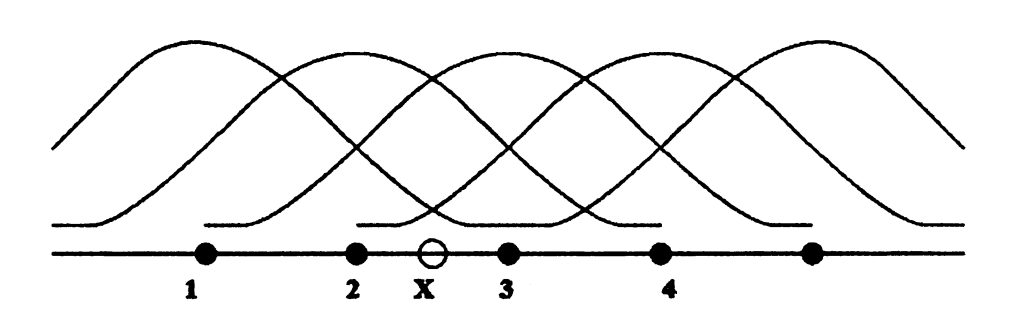


Figure 3.3 The weight functions over 1D domain of influence

In the above equations,  $d_{\max}$  is a scaling factor,  $(c_x, c_y)$  is the difference between node  $x_j$  and its nearest neighbor. It is important that  $d_{\max}$  is carefully chosen. If  $d_{\max}$  is too small, then too few nodes are in the local domain of influence, and the matrix B becomes singular; if  $d_{\max}$  is too large, then too many nodes are present in the local domain of influence, and the local character of approximation will be affected, the accuracy will decrease and the calculation time will increase. In general, the optimum choice of  $d_{\max}$  is 1.4 to 3.5.

The continuity of the shape function is tightly related to the weight function. When the weight function  $w(r_i)$  and its (k-1) derivatives are continuous, the shape function  $\Phi_j(x)$  and its (k-1) derivatives are also continuous. In 3D, the definition of weight function is a natural extension of that presented for 2D solution domain.

In the previous work, uniformly distributed background nodes were used. Further the symmetric weight function makes the domain of influence symmetric as well. When modeling large solution domain, non-uniformly distributed nodes are used for efficiency, so the domain of influence is asymmetric. Hence the asymmetric weight function should be modified and implemented accordingly so that it is continuous. For example, when the cubic splines weight function is applied, it is itself continuous as well as its 1<sup>st</sup> and 2<sup>nd</sup> order derivatives, even when it is asymmetric. In the case of Gaussian and Exponential weight function, they are both higher order weight functions and hence continuous as well. Figure 3.4 shows the asymmetry of the domain of influence.

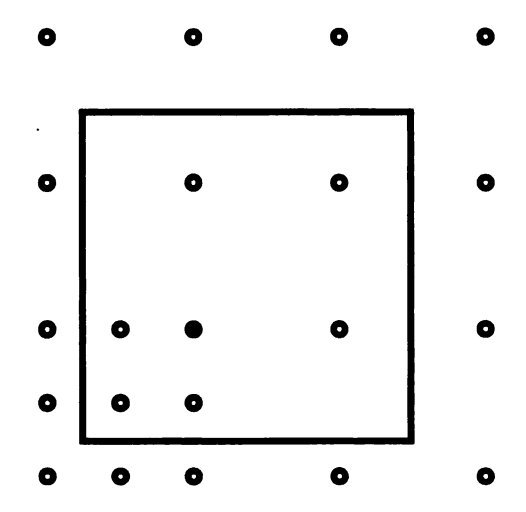


Figure 3.4 The asymmetry of the domain of influence

## 3.5 Discontinuities Approximation

In NDE applications the test geometry typically involves multiply connected regions with each region characterized by its own material properties, such as conductivity and permeability. This results in a discontinuity of the normal component of current density at the interface boundaries which in turn implies that the derivatives of the shape function or the shape function itself will be discontinuous at the interface. Since continuity of shape functions is inherited from continuity of the

weight function, it is necessary to introduce discontinuity into the weight function.

One technique used to realize this is by using the visibility criterion [40].

The visibility criterion is illustrated in Figure 3.5, for the rectangular domain. If there is no material discontinuity, the domain of influence is the total area of the square. However, in the presence of a discontinuity, the domain of influence of node  $x_j$  shrinks to the area covered by dashed horizontal line, and the weight function vanishes outside of that area. This procedure directly results in the discontinuity of weight function, which in turn introduces the discontinuity of shape function and its derivatives.

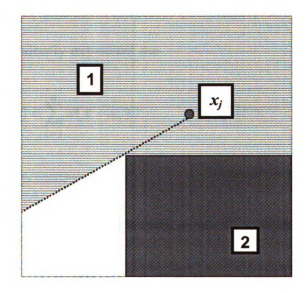


Figure 3.5 Domain of influence of node adjacent to material discontinuity (rectangular domain)

#### 3.6 The Orthogonal Basis

From equation (3.14), we can see that the basis function is one factor in the overall shape function and hence affects the accuracy of solution. In theory, increasing the order of basis functions improves the accuracy of solution. But in the EFG method it is often seen that higher order ( $m \ge 4$ ) polynomial basis functions suffers from a lack of convergence procedure because the associated shape function matrix becomes ill-conditioned. The 1D proof of this statement is presented below.

In the EFG method, the shape function defined in equation (3.14) involves the inversion of matrix B, which is defined in (3.10). Here W is the matrix of weight function and P is the basis function coefficient vector.

$$\boldsymbol{B}(\boldsymbol{x}) = \boldsymbol{P}^T \boldsymbol{W}(\boldsymbol{x}) \boldsymbol{P} \tag{3.25}$$

So **B** can be equivalently expressed as:

$$B(x) = \sum_{i=1}^{n} w(x - x_i)[1, x_i, \dots, x_i^m]^T [1, x_i, \dots, x_i^m].$$
(3.26)

Each element in matrix B is written in the form of an inner product:

$$\langle p_l(x), p_k(x) \rangle = \sum_{i=1}^n w(x - x_i) x_i^l x_i^k$$
, where  $l, k = 0, 1, \dots, m$  (3.27)

So

$$B(x) = \begin{bmatrix} \langle p_1(x), p_1(x) \rangle & \cdots & \langle p_1(x), p_m(x) \rangle \\ \cdots & \cdots & \cdots \\ \langle p_m(x), p_1(x) \rangle & \cdots & \langle p_m(x), p_m(x) \rangle \end{bmatrix}$$

(3.28)

Rewrite the inner product in integral form, we get

$$\langle p_l(\mathbf{x}), p_k(\mathbf{x}) \rangle = \int_{\Omega} \sum_{i=1}^n w(\mathbf{x} - \mathbf{x}_i) \mathbf{x}^l \mathbf{x}_i^k d\mathbf{x}$$
(3.29)

When  $L^2(a,b)$  space is unit of  $L^2(-1,1)$  space, which means the solution domain is [-1, 1], then matrix B is Hilbert matrix, which is ill-conditioned and difficult to invert numerically.

$$B(x) = H = \begin{bmatrix} 1 & 1/2 & \cdots & 1/(m+1) \\ 1/2 & 1/3 & \cdots & 1/(m+2) \\ \cdots & \cdots & \cdots \\ 1/(m+1) & 1/(m+2) & \cdots & 1/(2m+1) \end{bmatrix}$$
(3.30)

For the general  $L^2(a,b)$  space, the structure of matrix B is similar to Hilbert matrix, which is ill-conditioned and hard to invert. This makes calculation of shape function difficult. This is the reason that the higher order (m  $\geq$  4) polynomial basis functions lead to lack of convergence in EFG procedure.

Choosing an orthogonal basis [42] can solve this problem. The definition of orthogonal basis is shown below:

Vector  $p(x) = [p_1(x),...,p_j(x),...,p_m(x)]^T$  is an orthogonal basis, if the inner product satisfies

$$\langle p_l(\mathbf{x}), p_k(\mathbf{x}) \rangle = \sum_{i=1}^{N} w(\mathbf{x} - \mathbf{x}_i) p_l(\mathbf{x}_i) p_k(\mathbf{x}_i) = \begin{cases} 0 & (l \neq k) \\ C_l \neq 0 & (l \neq k) \end{cases}$$
(3.31)

Therefore, its shape matrix becomes

$$B(x) = \begin{bmatrix} \langle p_1(x), p_1(x) \rangle & & & \\ & \ddots & & \\ & & \langle p_m(x), p_m(x) \rangle \end{bmatrix}$$
(3.32)

The recursive relationship of orthogonal basis is given by,

$$\begin{cases}
p_{1}(x) = 1 \\
p_{2}(x) = (x - \alpha_{2})p_{1}(x) \\
p_{k+1}(x) = (x - \alpha_{k+1})p_{k}(x) - \beta_{k}p_{k-1}(x)
\end{cases}$$
(3.33)

where k = 1, 2, ..., m. The parameters  $\alpha$ ,  $\beta$  are obtained as,

$$\begin{cases}
\alpha_{k+1} = \frac{\langle x p_k(x), p_k(x) \rangle}{\langle p_k(x), p_k(x) \rangle} \\
\beta_k = \frac{\langle p_k(x), p_k(x) \rangle}{\langle p_{k-1}(x), p_{k-1}(x) \rangle}
\end{cases}$$
(3.34)

where k = 0,1,...,m-1. Substituting equations (3.32)-(3.34) into (3.13), the shape functions are then expressed as:

$$\Phi_i(x) = \sum_{j=1}^m \frac{w(x - x_i)p_j(x_i)}{\langle p_j(x), p_j(x) \rangle} p_j(x)$$
(3.35)

The partial differential form of the shape function is

$$\frac{d\Phi_{i}(x)}{dx} = \sum_{j=1}^{m} \frac{\frac{dw(x - x_{i})}{dx} p_{j}(x_{i}) p_{j}(x)}{\left\langle p_{j}(x), p_{j}(x) \right\rangle}$$

$$+ \sum_{j=1}^{m} \frac{w(x - x_{i}) p_{j}(x_{i}) \frac{dp_{j}(x)}{dx}}{\left\langle p_{j}(x), p_{j}(x) \right\rangle}$$

$$- \sum_{j=1}^{m} \frac{w(x - x_{i}) p_{j}(x_{i}) p_{j}(x) \frac{d\left\langle p_{j}(x), p_{j}(x) \right\rangle}{dx}}{\left\langle p_{j}(x), p_{j}(x) \right\rangle^{2}}$$

$$(3.36)$$

And the partial differential of inner product form is

$$\frac{d\langle p_j(x), p_j(x)\rangle}{dx} = \left[\sum_{i=1}^N w(x - x_i) \left[p_j(x_i)\right]^2\right] = \sum_{i=1}^N \frac{dw(x - x_i)}{dx} \left[p_j(x_i)\right]^2$$
(3.37)

These equations (3.31)-(3.37) indicate that the computations in EFG method eliminate the need for inversion of the shape function matrix when the orthogonal bases are used. This in turn makes the implementation of EFG method simpler [48], increases the accuracy of the solution by allowing higher order bases and also converges in fewer numbers of iterations.

## CHAPTER 4. FORWARD MODEL VALIDATION

#### 4.1 Introduction

In Chapter 3, the basic formulation of EFG method and modifications to improve its performance have been proposed. The improved formulation will be validated by static and quasi-static electromagnetic field computation via comparison against analytical models and the conventional EFG. Results of performance of the forward model on both 1D and 2D problems are presented in this chapter.

The implementation of static and low frequency electromagnetic fields is the basis of eddy current inspection of conducting test specimen. To simulate this underlying physics of material-energy interaction, the fields are typically expressed in terms of potentials and the governing equations which are Poisson or diffusion equations are solved together with appropriate boundary and interface conditions. In the following, we will analyze the application of the improved EFG formulation to the numerical solution of these equations.

In general, consider a domain of interest denoted by  $\Omega$  that is bounded by  $S_1 \cup S_2 = \partial \Omega$ , where  $S_1$  is the Dirichlet boundary and  $S_2$  is the Neumann boundary.

### 4.2 1D Problem

A 1D electrostatic Poisson problem for the potential function u is described as follows:

$$\begin{cases} \nabla^2 u = -x & (\Omega: 0 < x < 1) \\ u(0) = 0 & u'(1) = 0 \end{cases}$$

(4.1)

To obtain the discrete system equations, it is necessary to use a weak form of the equilibrium equation and boundary conditions. Galerkin method is used for the choice of test function and Lagrange multipliers are applied for incorporating boundary conditions. The final discrete function can be obtained by substituting the trial functions u(x) and test function into the weak form, yielding the system of linear algebraic equations.

The exact solution is  $u(x) = \frac{1}{2}x - \frac{1}{6}x^3$  for comparison with the numerical solutions.

Figure 4.1 shows the exact solution and the numerical solution using EFG method with 1<sup>st</sup> and 2<sup>nd</sup> order polynomial basis. Although the solution with 2<sup>nd</sup> order polynomial basis convergences, it starts to show some instability as explained in Chapter 3, that the higher order polynomial basis produces numerical oscillations of the solution.

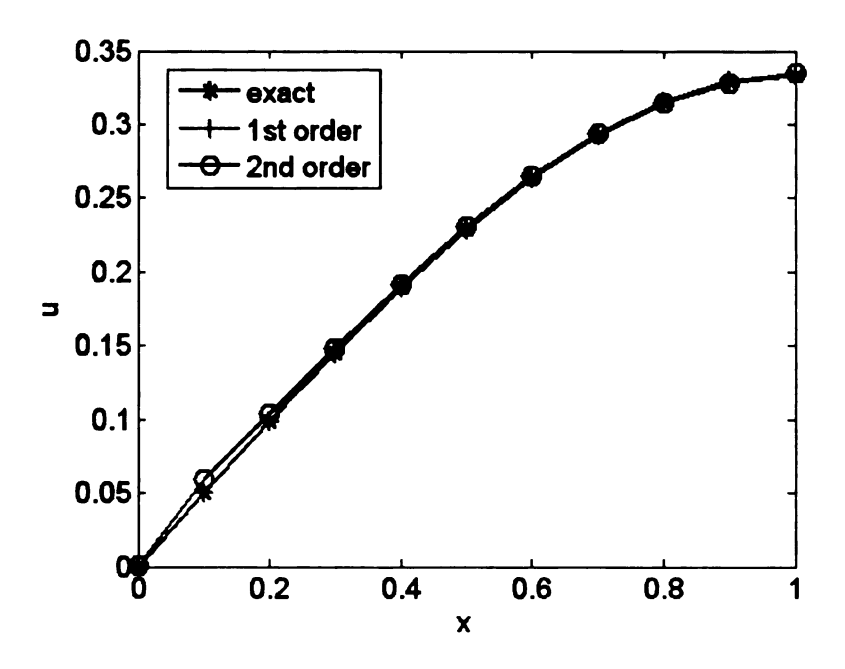


Figure 4.1 The comparison of exact and EFG solution with 1<sup>st</sup>, 2<sup>nd</sup> order polynomial basis

Figire 4.2 shows the exact solution as well as the solution using EFG method with 3<sup>rd</sup> order polynomial basis. The numerical solution no longer converges. It means the oscillations become more severe so that the numerical solution is invalid.

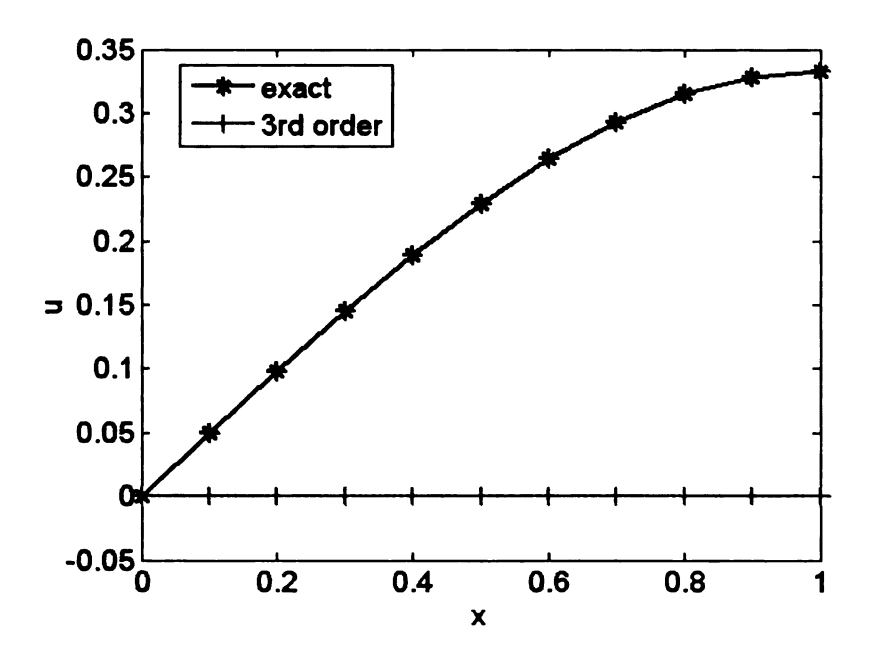


Figure 4.2 The comparison of exact and EFG solution with 3<sup>rd</sup> order polynomial basis

In Figure 4.3, the numerical solution using EFG method with orthogonal basis function is presented. The order of the basis function varies from 1 to 4 and the numerical solutions are seen to be stable and convergent, which demonstrates the effectiveness of higher order orthogonal basis functions.

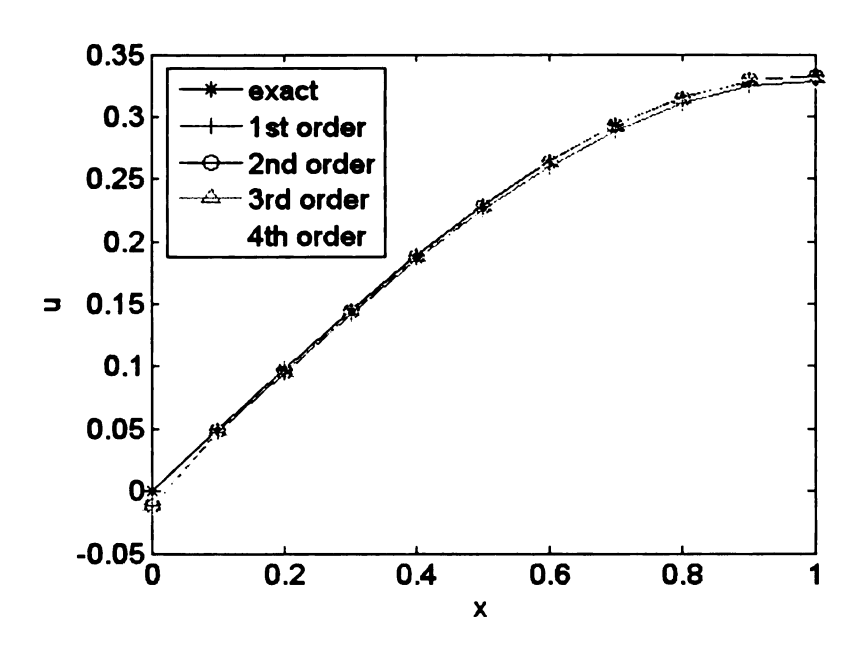


Figure 4.3 The comparison of exact solution with various order orthogonal basis

## 4.3 2D Problem

The 2D eddy current modeling geometry is shown in Figure 4.4. Assume an infinite-size 2D conducting plate with a tight (zero width) crack along y direction (length = 1.0 cm) placed as shown. A time-varying harmonic current source is applied using a thin foil in the x direction.

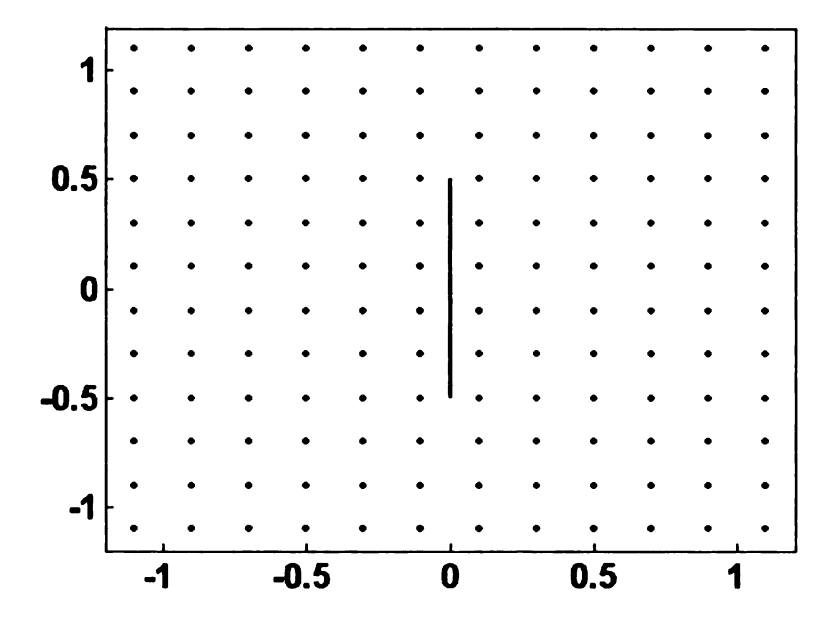


Figure 4.4 Modeling geometry for 2D problem

The induced current will be strictly along -x direction in the absence of crack. The induced currents will bend around the corners in the presence of the crack. This geometry is typically encountered in 2D eddy current problems. The plot of the induced eddy current predicted by the model is shown in Figure 4.5.

Figure 4.5 (a) shows the induced eddy current with the crack obtained using 1<sup>st</sup> order polynomial basis function and (b) shows the image obtained using 2<sup>nd</sup> order polynomial basis function. Due to the complexity of the problem, the EFG model using 2<sup>nd</sup> order polynomial basis function is no longer convergent and solution is incorrect.

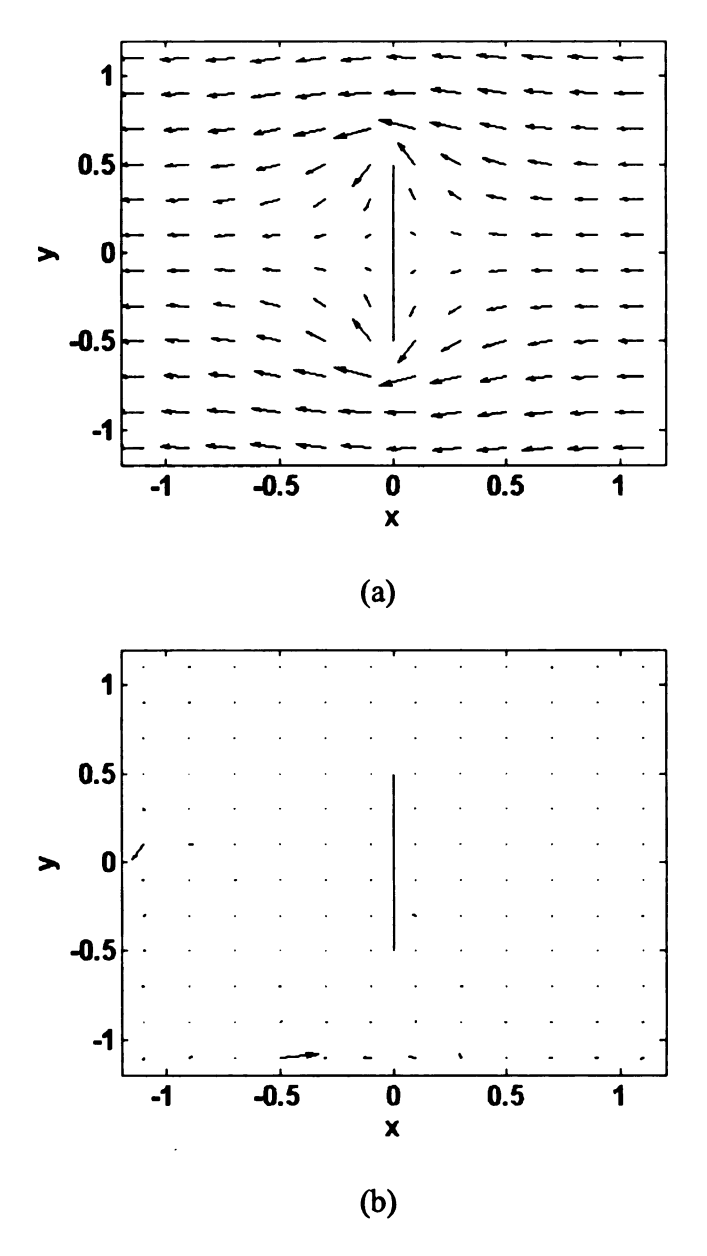


Figure 4.5 Induced eddy current plot using EFG method by polynomial basis function (a) 1<sup>st</sup> order (b) 2<sup>nd</sup> order

Figure 4.6 (a) shows the induced current plot using EFG method with 2<sup>nd</sup> order orthogonal basis and (b) shows the difference compared with Figure 4.5 (a). It is clear that the EFG model with 2<sup>nd</sup> order orthogonal basis function still converges and only

minor differences are observed at the boundaries compared with the 1<sup>st</sup> order polynomial basis function.

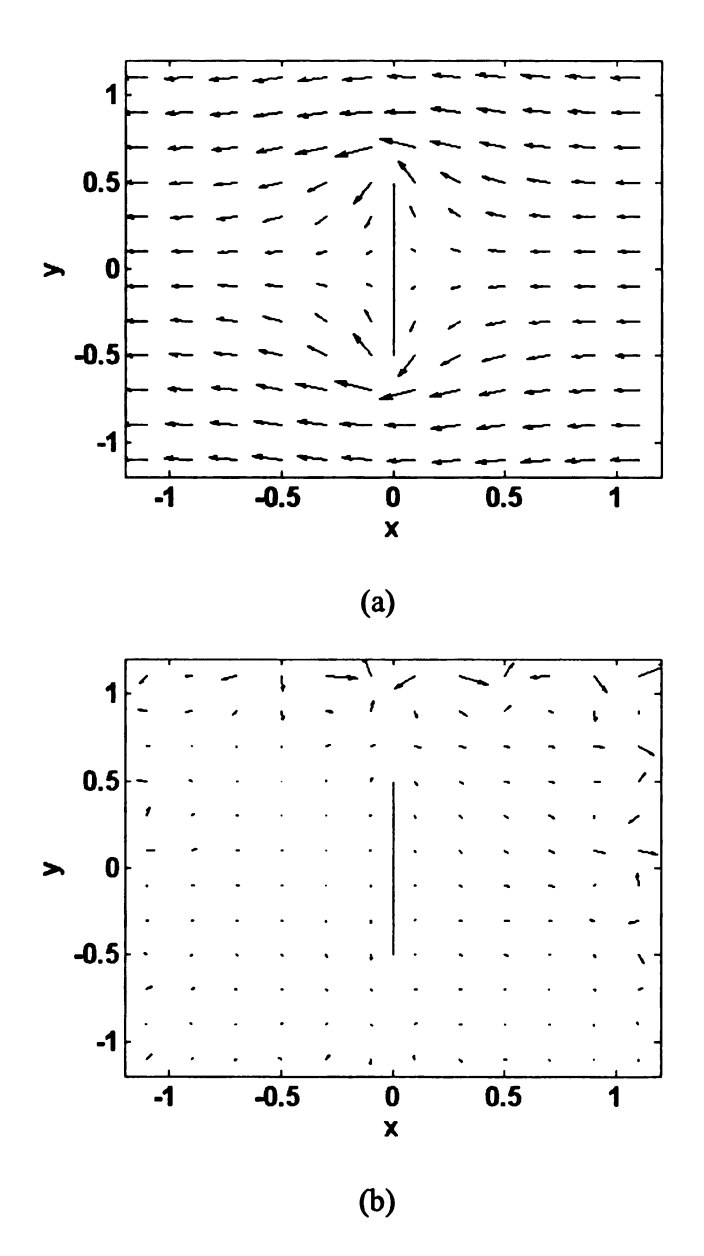


Figure 4.6 Induced eddy current plot using EFG method by orthogonal basis function (a)  $2^{nd}$  order (b) comparison with Figure 4.5 (a)

Figure 4.7 shows the iteration error in each step using 1<sup>st</sup> order polynomial basis and 2<sup>nd</sup> order orthogonal basis. From the following figure, we can conclude that the EFG model developed in this dissertation with orthogonal basis converges faster than the one with conventional polynomial basis.

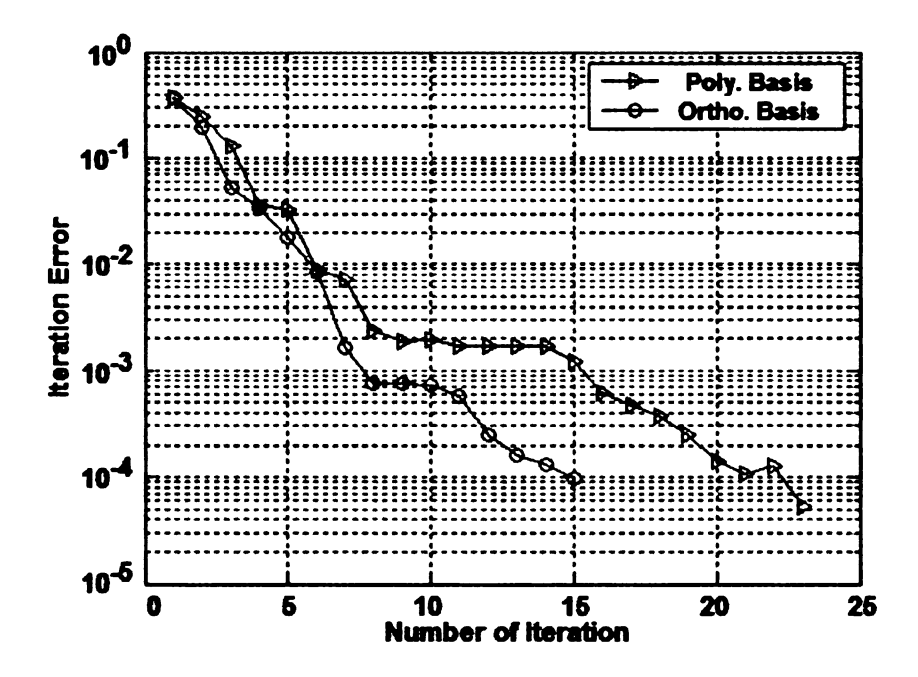


Figure 4.7 The convergence rate using polynomial basis and orthogonal basis

For the 1D problem in section 4.2, the Lagrange Multipliers is used to impose the essential boundary condition, because of the small size of the solution domain. In the above 2D eddy current problem, the penalty method is used to impose the essential boundary condition. The size of the discrete matrix is reduced while the accuracy is retained.

## **CHAPTER 5. FORWARD MODEL IMPLEMENTATION**

### 5.1 Introduction

This chapter presents the application of the EFG method to electromagnetic field computations in a 3D NDE test geometry. In quasi-static frequency range, the governing equations can be simplified to a diffusion equation in terms of magnetic vector potential and electric scalar potential. The numerical results are validated via comparison against experimental data and results obtained using conventional FEM.

#### 5.2 Mathematical Formulation

Let  $\Omega_1$  and  $\Omega_2$  be partitions of the solution domain, where  $\Omega_1$  denotes the conducting region and  $\Omega_2$  represents the surrounding free space. Let A be the magnetic vector potential in both  $\Omega_1$  and  $\Omega_2$ , and V be the electric scalar potential in  $\Omega_1$ .  $\mu$  and  $\sigma$  are the permeability and conductivity of the media respectively. Derived from Maxwell's equations, the governing diffusion equation for conventional eddy current problem in Cartesian coordinates can be written as [50]

$$\nabla \times \frac{1}{\mu} \nabla \times \mathbf{A} + j\omega \sigma \mathbf{A} + \sigma \nabla V = \mathbf{J}_s \text{ in } \Omega$$
 
$$\nabla \cdot (j\omega \sigma \mathbf{A} + \sigma \nabla V) = 0 \text{ in } \Omega_1$$
 (5.1)

(5.2)

where  $J_s$  is the assigned source current density.

To obtain the numerical solutions of equation (5.1) and (5.2), we first expand the potentials (magnetic vector potential and electric scalar potential) as a linear combination of shape functions associated with the nodes, we get:

$$A = \sum_{j} (A_{xj} \Phi_{j} \hat{\boldsymbol{a}}_{x} + A_{yj} \Phi_{j} \hat{\boldsymbol{a}}_{y} + A_{zj} \Phi_{j} \hat{\boldsymbol{a}}_{z})$$

$$V = \sum_{j} V_{j} \Phi_{j}$$

$$(5.3)$$

where  $A_{xj}$ ,  $A_{yj}$ ,  $A_{zj}$  are the three components of the magnetic vector potential at node j;  $V_j$  is the scalar potential;  $\Phi_j$  is the shape function, and  $\hat{a}_x$ ,  $\hat{a}_y$ ,  $\hat{a}_z$  are the Cartesian unit vectors.

Homogeneous Dirichlet boundary conditions are applied at external boundaries and current continuity condition  $J_n = \sigma(-j\omega A - \nabla V) \cdot \hat{n} = 0$  is applied on interfaces to obtain a unique solution. Because EFG shape function does not satisfy the Kronecker delta property, essential boundary condition can not be imposed directly as is done in FEM. As discussed earlier, the penalty method is used for this purpose.

To obtain a system of linear algebraic equations, the Galerkin method is used. Substituting the above expansions (5.3) and (5.4) into the governing equations (5.1) and (5.2), we get:

$$S_{1} + \alpha S = \sum_{j=1}^{3N} \left[ \int_{\Omega} \left( \frac{1}{\mu} (\nabla \times \boldsymbol{\Phi}_{i}) \cdot (\nabla \times \boldsymbol{\Phi}_{j}) + \frac{1}{\mu} (\nabla \cdot \boldsymbol{\Phi}_{i}) (\nabla \cdot \boldsymbol{\Phi}_{j}) + j\omega \sigma \boldsymbol{\Phi}_{i} \cdot \boldsymbol{\Phi}_{j} \right) d\Omega \right] A_{j}$$

$$+ \sum_{j=1}^{N} \left[ \int_{\Omega} \sigma \boldsymbol{\Phi}_{i} \cdot \nabla \Phi_{j} d\Omega \right] V_{j} + \alpha \sum_{j=1}^{3N} \left[ \int_{\Gamma_{k}} \boldsymbol{\Phi}_{i} \cdot \boldsymbol{\Phi}_{j} d\Omega \right] A_{j} + \alpha \sum_{j=1}^{N} \left[ \int_{\Gamma_{k}} \Phi_{i} \cdot \Phi_{j} d\Omega \right] V_{j}$$

$$= \sum_{j=1}^{3N} \int_{\Omega} J_{s} \cdot \boldsymbol{\Phi}_{j} d\Omega + \alpha \sum_{j=1}^{3N} \left[ \int_{\Gamma_{k}} u_{0} \cdot \boldsymbol{\Phi}_{j} d\Gamma \right] + \alpha \sum_{j=1}^{N} \left[ \int_{\Gamma_{k}} u_{0} \cdot \Phi_{j} d\Gamma \right]$$

$$= \sum_{j=1}^{3N} \int_{\Omega} J_{s} \cdot \boldsymbol{\Phi}_{j} d\Omega + \alpha \sum_{j=1}^{3N} \left[ \int_{\Gamma_{k}} u_{0} \cdot \boldsymbol{\Phi}_{j} d\Gamma \right] + \alpha \sum_{j=1}^{N} \left[ \int_{\Gamma_{k}} u_{0} \cdot \Phi_{j} d\Gamma \right]$$

$$(5.5)$$

$$= \sum_{j=1}^{3N} \int_{\Omega} J_{s} \cdot \boldsymbol{\Phi}_{j} d\Omega + \alpha \sum_{j=1}^{3N} \left[ \int_{\Omega} \sigma \nabla \Phi_{j} \cdot \nabla \Phi_{j} d\Omega \right] V_{j} = 0$$

$$(5.6)$$

In (5.5),  $\alpha$  is the penalty parameter. Generally, the penalty parameter should be carefully chosen so that  $\alpha S_2$  equals  $10^4$  or  $10^5$  times greater than S at the boundary nodes in the equation (5.5).

Equations (5.5) and (5.6) can be written in matrix form as

$$GA = Q \tag{5.7}$$

where the matrix G is a complex and sparse matrix; A is the vector of unknowns; four unknowns are at each node, including the electric scalar potential and the three components of the magnetic vector potential; Q is the load vector incorporating the current source.

Equation (5.7) is solved using (TF) QMR [53]. Only non-zero entries of G need to be stored in the iterative solution procedure. Compared with Lagrange multipliers, the matrix obtained using penalty function is of a reduced size and positive definite,

which makes the convergence faster.

The solution of (5.7) is then used to compute various measurable physical quantities such as flux density B, and induced eddy current density in the area of interest.

# 5.3 Magneto Optic Imaging Application

Magneto-optic imaging (MOI) is a relatively new sensor application of bubble memory technology to NDT and produces easy-to-interpret, real-time analog images [49]. In this technique, an induction foil is used induce eddy currents in the specimen and a magneto-optic sensor is used to detect the magnetic flux density associated with the induced currents. However, since the MOI data is binary, the information provided is qualitative in nature. A theoretical model that can simulate the MOI system can provide a more quantitative value of the magnetic fields and is hence useful for the optimization of the magneto-optic (MO) sensor and system [51], [52]. A linear FE model utilizing the  $A-\nu$  formulation was initially developed for this purpose. However the inclusion of infinitesimal air gaps between layers and the tight crack makes mesh generation very cumbersome and decreases the accuracy of FEM solutions. A more accurate EFG model is implemented and applied to MOI inspection geometry.

#### 5.3.1 Introduction to MOI in Airframe Inspection Application

In aircraft industry, for the airframes to stay in service much longer than the designed life, thousands of fasteners and bonded joints on the fuselage need to be inspected. In order to cover the large inspection area, fast, accurate and cost effective NDT inspection methods are clearly needed. Some of the challenges encountered in ECT are:

- (1) Detection of corrosions or cracks in the multi-layer structures
- (2) Detection of cracks under the fastener (CUF)
- (3) Detection of surface and subsurface defects close to edges

Conventional eddy current inspection method is time consuming due to the small probe size and large inspection area. Furthermore, it requires well-trained operators for data interpretation. Development of new techniques for rapid and accurate inspection is of considerable interest to the aircraft industry. MOI provides analog images that are fast and easy to interpret.

Briefly, in MO inspection, an induction foil is used to induce eddy currents in the conducting sample. The magnetic fields associated with the induced eddy currents are detected using a MO sensor. Polarized light passed through the MO sensor undergoes a rotation of the plane of polarization in the presence of local magnetic fields. When the reflected light is viewed through an analyzer, an analog image of local magnetization is seen on a monitor. Figure 5.1 (a) shows a schematic of the MOI device and Figure 5.1 (b) shows an experimental image. However the MO image is binary because of the physical properties of the garnet film sensor and does not

provide a quantitative value of the measured signal. A simulation model for MO inspection of multilayer aircraft geometries for predicting the continuous valued magnetic flux density that produces the observed experimental MO images has been developed.

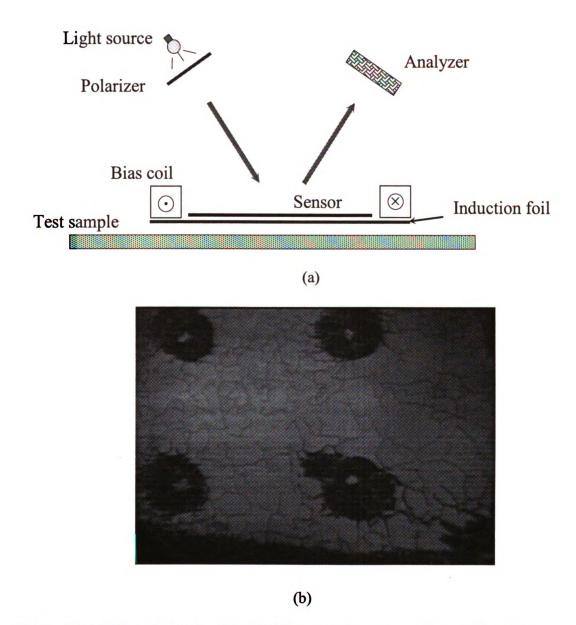


Figure 5.1 (a) The schematic of the MOI system (b) an experimental image

Figure 5.2 (a) shows a MOI 308 system and (b) shows inspection being performed using MOI system with ahead mounted display.



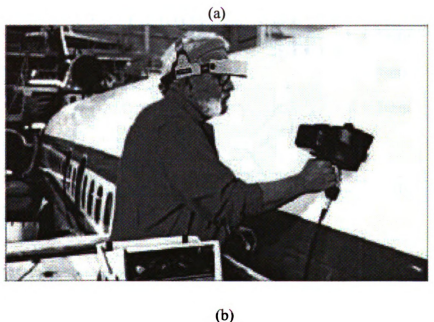


Figure 5.2 (a) The MOI 308 system (b) using of MOI system

#### 5.3.2 Modeling Geometry

A typical 3D MO inspection geometry used in both FEM and the EFG methods is shown in Figure 5.3.

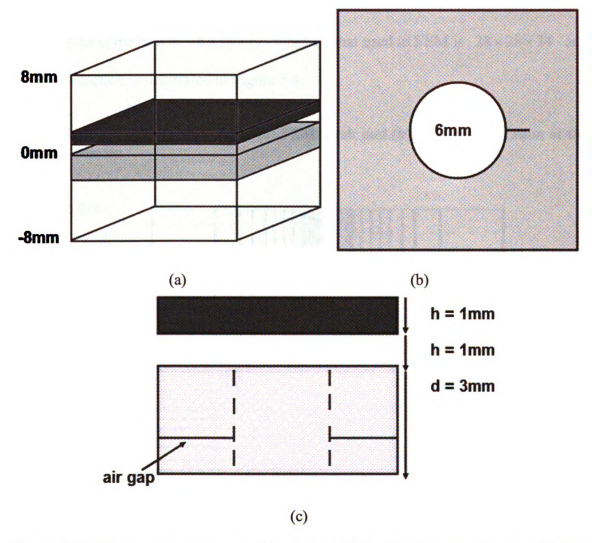
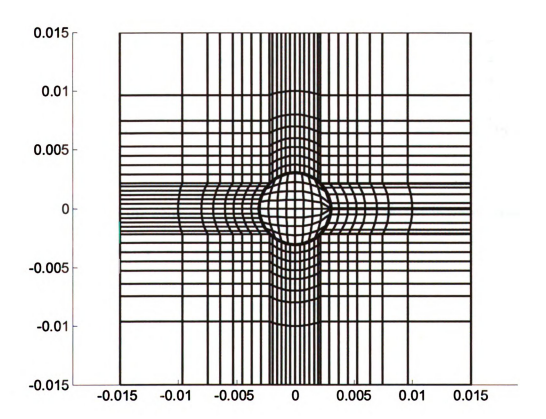


Figure 5.3 MOI simulation geometry (both for FEM and EFG). (a) 3-D view, (b) 2-D top view and (c) side view of the multilayer plate with a 6mm diameter fastener hole

The geometry consists of two layers of aluminum plates, of 3 mm total thickness and of infinite width & length. An infinitesimally small air gap exists between the two layers. An infinite inductive foil of 1 mm thickness, carrying a linear sinusoidal excitation current density of amplitude  $10^8 \, \text{A/m}^2$  and frequency 3 kHz is placed

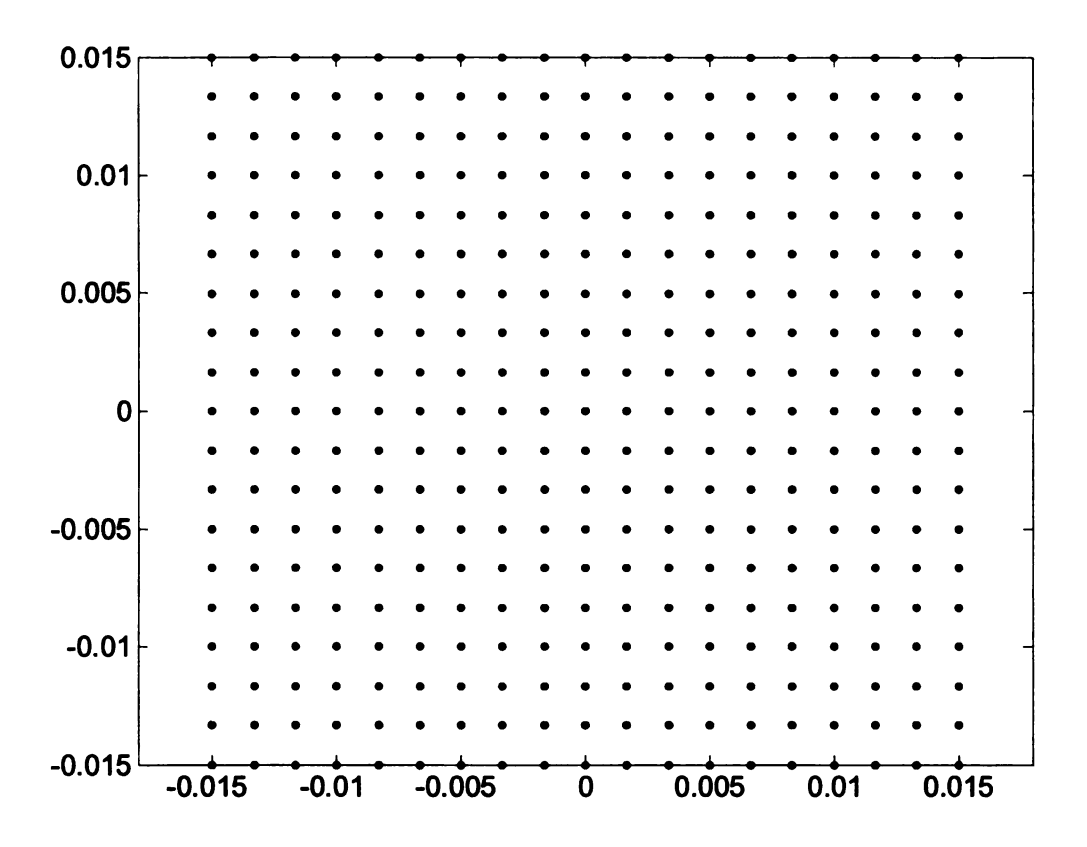
above the conducting multilayer plate at a distance of 1mm. The solution region is of dimensions [-12,12] mm  $\times [-12,12]$  mm  $\times [-8,8]$  mm. A fastener hole of 6 mm diameter is introduced extending through the two layers and a second layer tight crack of 5 mm radial length is also included. The number of nodes used for discretization using the EFG method is  $18 \times 18 \times 12$  whereas that used in FEM is  $28 \times 28 \times 24$  and the cross-section is illustrated in Figure 5.4.

Figure 5.4 2D cross-section view of (a) FEM mesh and (b) EFG discretization of the solution domain



(a)

Figure 5.4 continued



(b)
The boundaries of the solution region are chosen in air and the imposed boundary conditions are summarized in Table 1.

Table 1 Boundary conditions

Upper boundary	$A_x = A_y = A_z = 0, V = 0$
Lower boundary	$A_x = A_y = A_z = 0, V = 0$
Left boundary	$A_x = 0, V = 0, A_y, A_z$ are free
Right boundary	$A_x = 0, V = 0, A_y, A_z$ are free
Front boundary	$A_x = 0, V = 0, A_y, A_z$ are free
Rear boundary	$A_x = 0, V = 0, A_y, A_z$ are free

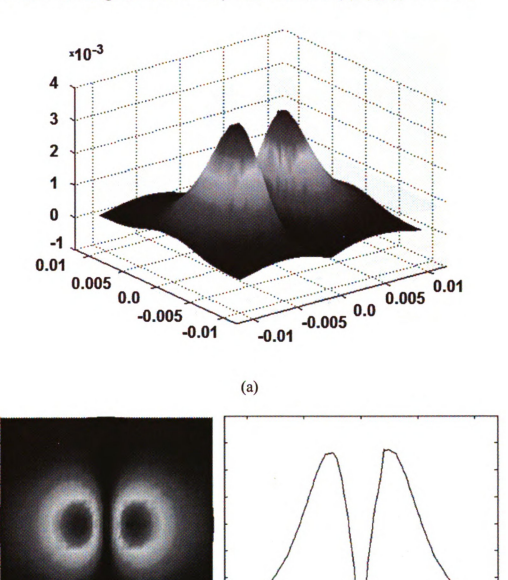
#### 5.3.3 Numerical Results I – Fastener hole without crack

Simulation results obtained using FEM and EFG for a defect free fastener hole are shown in Figure 5.5. The normal component of the magnetic flux density Bz is plotted at the MO sensor layer placed above the induction foil. A comparison of the computational time and mesh parameters are summarized in Table 2. Figure 5.6 shows a comparison of model predictions after thresholding and the experimental MO image.

Table 2 Summary of simulation results

	FEM	EFG
Peak value of magnetic	34.223	35.927
flux density (Gauss)		
Computation time (hours)	3	0.5
Number of nodes	28×28×24 = 18816	$18 \times 18 \times 12 = 3888$
Discretization complexity	complex (non-uniform	simple (uniformly
	elements)	distributed nodes)

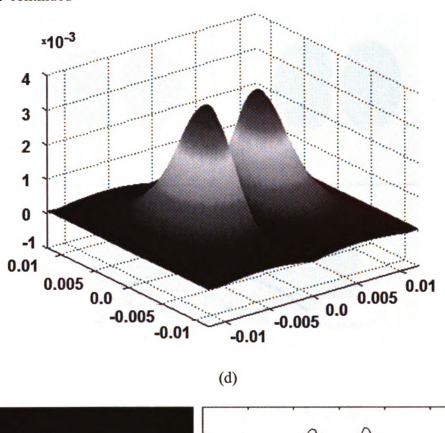
Figure 5.5 (a) 3D view, (b) 2D top view and (c) 2D side view of the normal component of the magnetic flux density with FEM and (d), (e), (f) with EFG

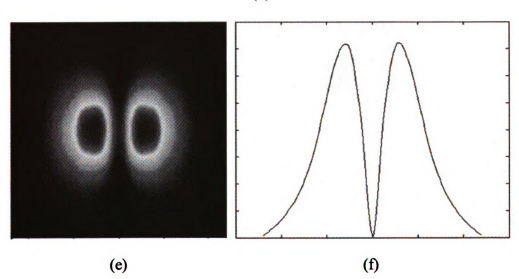


(c)

(b)

Figure 5.5 continued





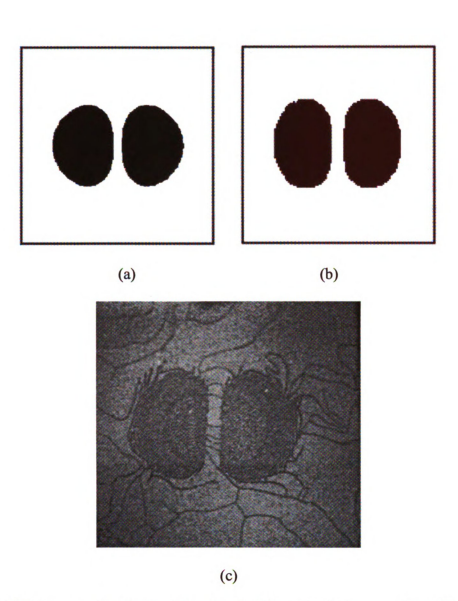


Figure 5.6 Binary results obtained by thresholding simulation results in Figure 5.5. (a) FEM (b) EFG and (c) experimental image

#### 5.3.4 Numerical Results II - Fastener hole with 5 mm second layer tight crack

Simulation results obtained using FEM and EFG for a fastener hole with 5 mm radial crack are shown in Figure 5.7. The normal component of the magnetic flux density is plotted at the MO sensor layer placed above the induction foil. A comparison of the computational time and mesh parameters are summarized in Table 3. Figure 5.8 shows a comparison of the model predictions after thresholding.

Table 3 Summary of simulation results

	FEM	EFG
Peak value of magnetic	35.467	37.779
flux density (Gauss)		
Computation time (hours)	3	0.5
Number of nodes	28×28×24 = 18816	18×18×12 = 3888
Discretization complexity	complex (non-uniform	simple (uniformly
	elements)	distributed nodes)

Figure 5.7 (a) 3D view, (b) 2D top view, and (c) 2D side view of the normal component of the magnetic flux density with FEM and (d), (e), (f) with EFG

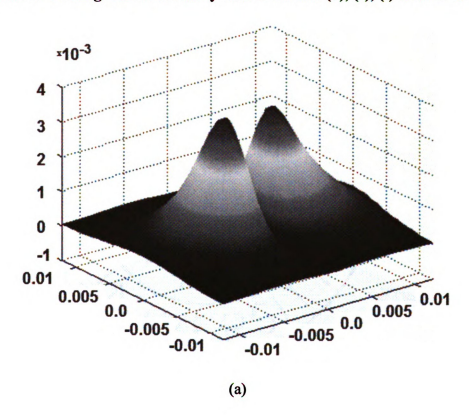
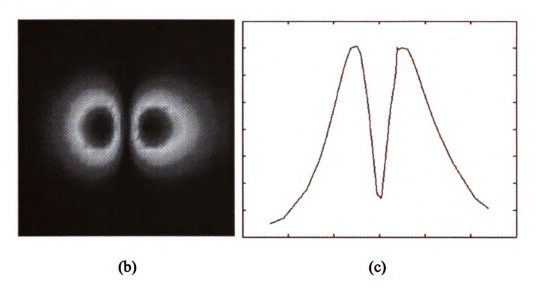


Figure 5.7 continued



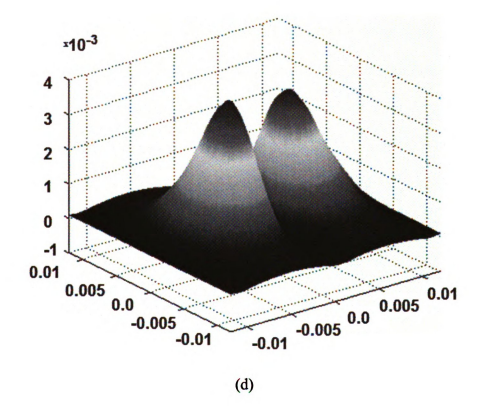
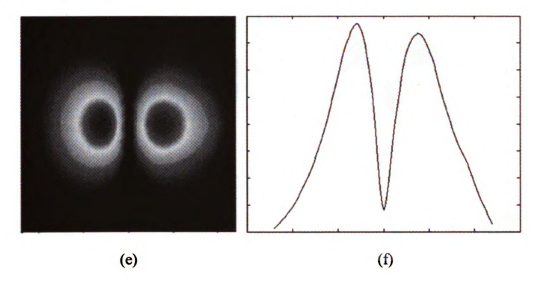


Figure 5.7 continued



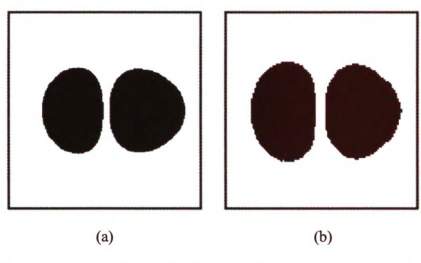


Figure 5.8 Binary results obtained by thresholding simulation results in Figure 5.7. (a) FEM (b) EFG

#### 5.3.5 Conclusion

The EFG method, gives us an efficient framework for modeling airframe geometry in its full complexity. A benefit of the EFG method is that it is inherently a high order scheme, which makes it more accurate than the conventional linear FEM. Another advantage of the EFG lies in its simplicity of domain discretization because it relies on only a cloud of nodes and does not require an underlying tessellation to describe the 3D domain. The infinitesimal air gaps between layers and the tight cracks are modeled by a layer of nodes alone. Initial results indicate that MO images predicted by the EFG model are much closer to the experimental images than those of the FE model with the same number of unknowns.

# CHAPTER 6. INVERSE PROBLEM USING EFG METHOD

### 6.1 Introduction

Inverse problem in NDE involves the estimation of true defect profile on the basis of the information contained in a measured NDE probe signal. As mentioned in chapter 1, inverse problems are generally ill-posed, and the full analytical solutions to these problems are seldom possible. Therefore, practical solutions employing a variety of constrained search techniques are used to find the optimal solution from the set of possible solutions. These techniques range from simple calibration procedure to pattern recognition algorithms such as neural networks. These approaches include direct and iterative procedures.

In the following, several well-known methods to solve inverse problem are reviewed:

Calibration methods [54] use calibration curves (or tables), which are obtained by generating a set of signal parameters either from experiments or numerical models for a variety of defect parameters to estimate (fit) a curve. The curve fitting technique can use polynomial approximation or other functional approximation method. These curves are then used to predict defect parameters for a given measured signal parameter.

Pattern recognition algorithms using neural networks involve mapping the measured signal directly to the defect profile [55]-[59]. In this case, signal inversion is treated as a function approximation problem and the mapping from the measured signal to the defect profile is learned by a neural network or other signal processing algorithm using training data.

Model-based solution to inverse problems [60], [61] employs a forward model that can predict the measured signal for a given defect profile in an iterative framework. The iteration starts with an initial estimation of the defect profile represented by the defect parameters, and forward problem is solved to determine the corresponding signal. The cost function defining the error between the measured and predicted signals is minimized iteratively by updating the defect profile. When the error is below a pre-defined threshold, the iteration ends and the updated defect parameters represent the desired solution.

Iterative methods generate accurate reconstruction solutions, however due to the high-dimensional (2D or 3D) numerical models in each iteration; they are computationally intensive and hence have limited practical applications. Previous work using FE model based iterative techniques for inverting conventional eddy current data has been reported by Li [60].

In this dissertation, the model based NDT inverse problem that uses the EFG model for simulating the physical process is proposed. The overall iterative approach using the forward model is shown in Figure 6.1.

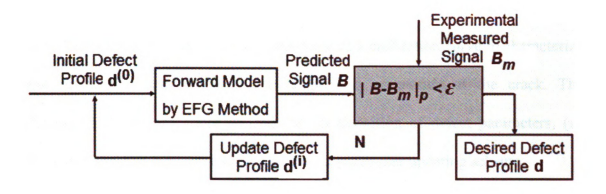


Figure 6.1 Schematic representation of the iterative approach of the inverse problem

From the above iteration loop, we can see that this approach consists of two parts: the development of a forward model of the underlying physical processes, which has been presented in previous chapters; and a scheme for updating of defect parameters to derive the desired profile. The different updating schemes are described in this chapter.

Three approaches are considered in this thesis.

- 1. Parametric calibration method for 1D problem
- 2. State space search method that can be used in 2D problem
- 3. Gradient based method using Adjoint equation for 2D problem

The formulation, implementation and preliminary results of each approach are presented here.

#### 6.2 1D Problems - Parametric Approach

The case of a 1D tight crack is considered in this section. The NDE inspection uses a linear induction foil to induce eddy currents and the normal component of

associated magnetic flux density is measured using a Giant magneto-resistance (GMR) sensor. This approach is based on the generation of a calibration curve to characterize a few crack parameters such as the length and orientation of the crack. The performance of this procedure depends on (i) definition of defect parameters, (ii) definition of the cost function and (iii) the defect parameter updating scheme.

#### 6.2.1 Problem Statement and Inversion Scheme

The tight crack is characterized by the parameters r, z and  $\theta$ ; where r corresponds to the radial distance of the crack center from the origin, z corresponds to the length of the crack perpendicular to current direction and  $\theta$  corresponds to the angle made by the crack with the linear current direction as shown in Figure 6.2. We denote these independent variables by vector X:

$$X = \{r, z, \theta\} \tag{6.1}$$

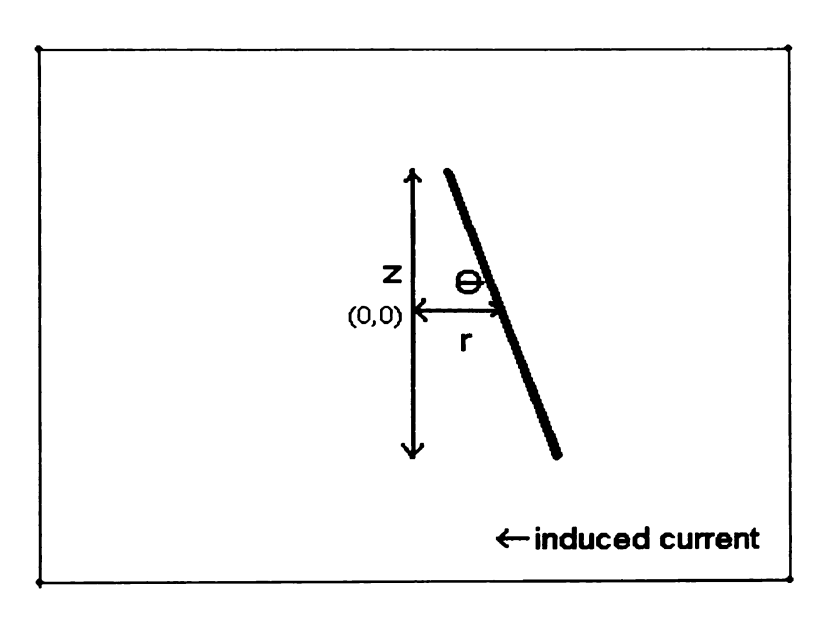


Figure 6.2 Definition of the defect parameters for 1D crack

Assuming a given initial value for  $X = \{r, z, \theta\}$ , the EFG model solves the forward problem for simulating the underlying physical phenomenon and generating the GMR signal. The desired solution is obtained by iteratively updating the parameters to minimize the error between the given experimental input signal and forward model prediction.

The EFG model uses the visibility criterion to model the crack. The update equation and the node discretization of the defect greatly save the computational cost.

The cost function, chosen as the square of the error between the experimental measurement and model predicted signals is given in equation (6.2).

$$F = \sum_{n=1}^{N} |B_n - B_{mn}|^2 \tag{6.2}$$

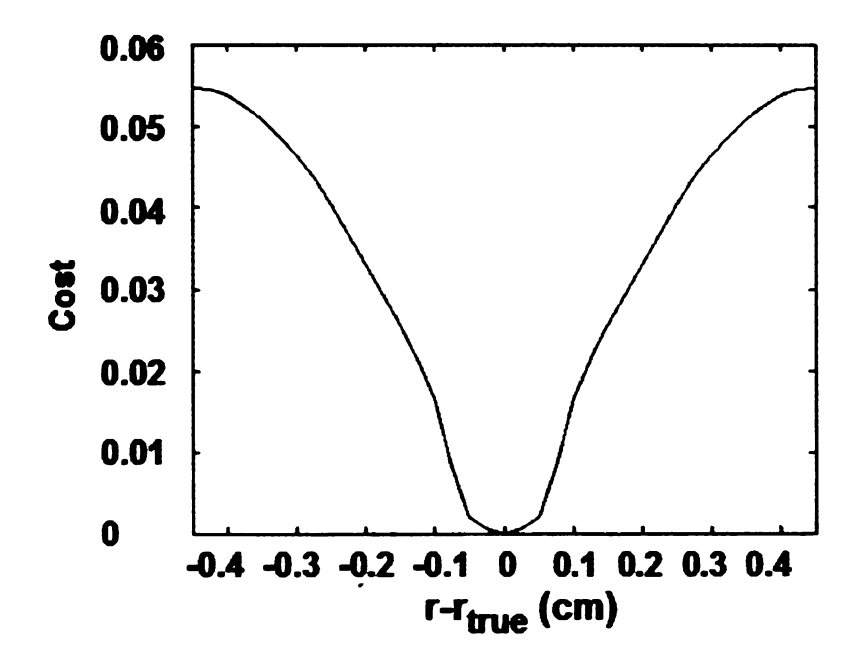
where  $B_n$  is the n-th point of the EFG predicted signal representing the magnitude of the normal component of magnetic flux,  $B_{mn}$  is the n-th point of the measured (or simulated) signal and N is the number of data points in B and  $B_m$ . The derivative of the cost function is approximated as:

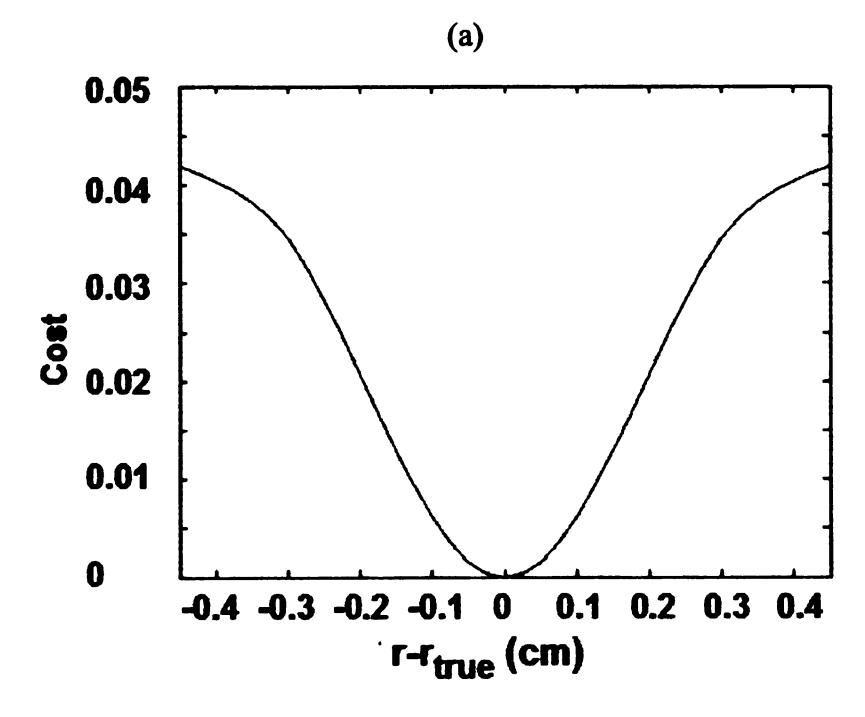
$$\frac{dF}{dX} = \frac{F(X + \Delta X) - F(X)}{\Delta X} \tag{6.3}$$

### 6.2.2 Inversion Results and Discussion

The results of inversion are presented here using simulated data instead of measured signal. The 2D geometry consisting of an infinite aluminum plate is excited by an infinite induction foil carrying a 3 kHz sinusoidal current along the x-direction. A database of tight cracks,  $X^i = \left\{r^i, z^i, \theta^i, i = 1, 2, 3, ...n\right\}$  are simulated and the predicted signals  $B_i$  are compared with the measured signal from a true defect  $B_{mi}$  to get cost function values  $F_i$  corresponding to the i-th crack  $X^i$ . Figures 6.3 (a), (b) and (c) show the normalized cost function versus the r, z and  $\theta$  parameters independently. The x-axis indicates the difference between predicted and true parameter values. When the x-axis is zero, the predicted defect parameter is exactly equal to the true defect parameter value. These curves are used for estimating the derivatives in equation (6.3).

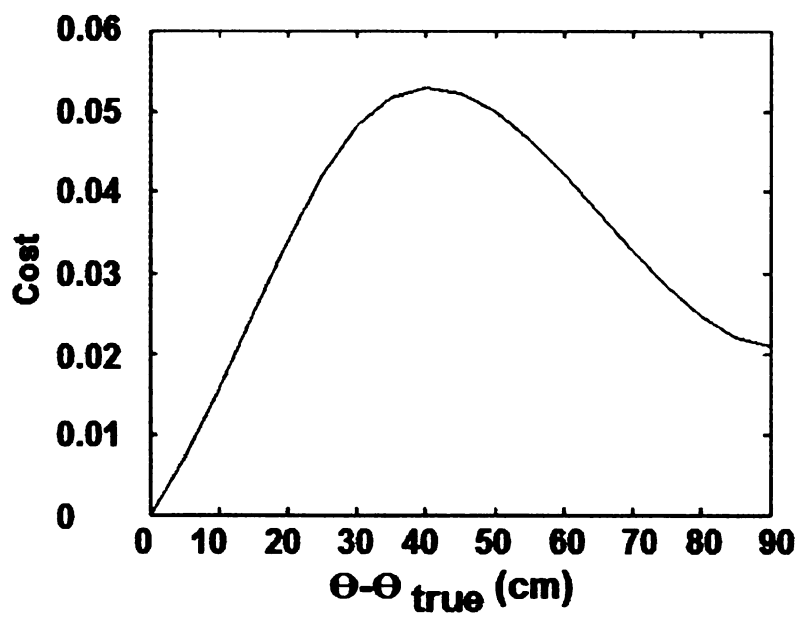
Figure 6.3 Cost function versus (a) r, (b) z and (c)  $\theta$ 





**(**b)

Figure 6.3 continued



In order to test the inversion scheme, a straight tight crack of infinite depth, zero width and length = 1.0 cm is introduced and the corresponding signal is used as the measured data  $B_m$ . The true and predicted cracks using this inversion scheme are shown in Figure 6.4. The regular grid of dots shows the nodes in the EFG model. Figure 6.4 (a) shows the initial guess (dotted line), the true defect (solid line), and the final prediction (dashed line) when the straight tight crack is along the direction

perpendicular to the linear current. Figure 6.4 (b) shows the corresponding results

when the crack is at an angle of 55 degrees with the current direction.

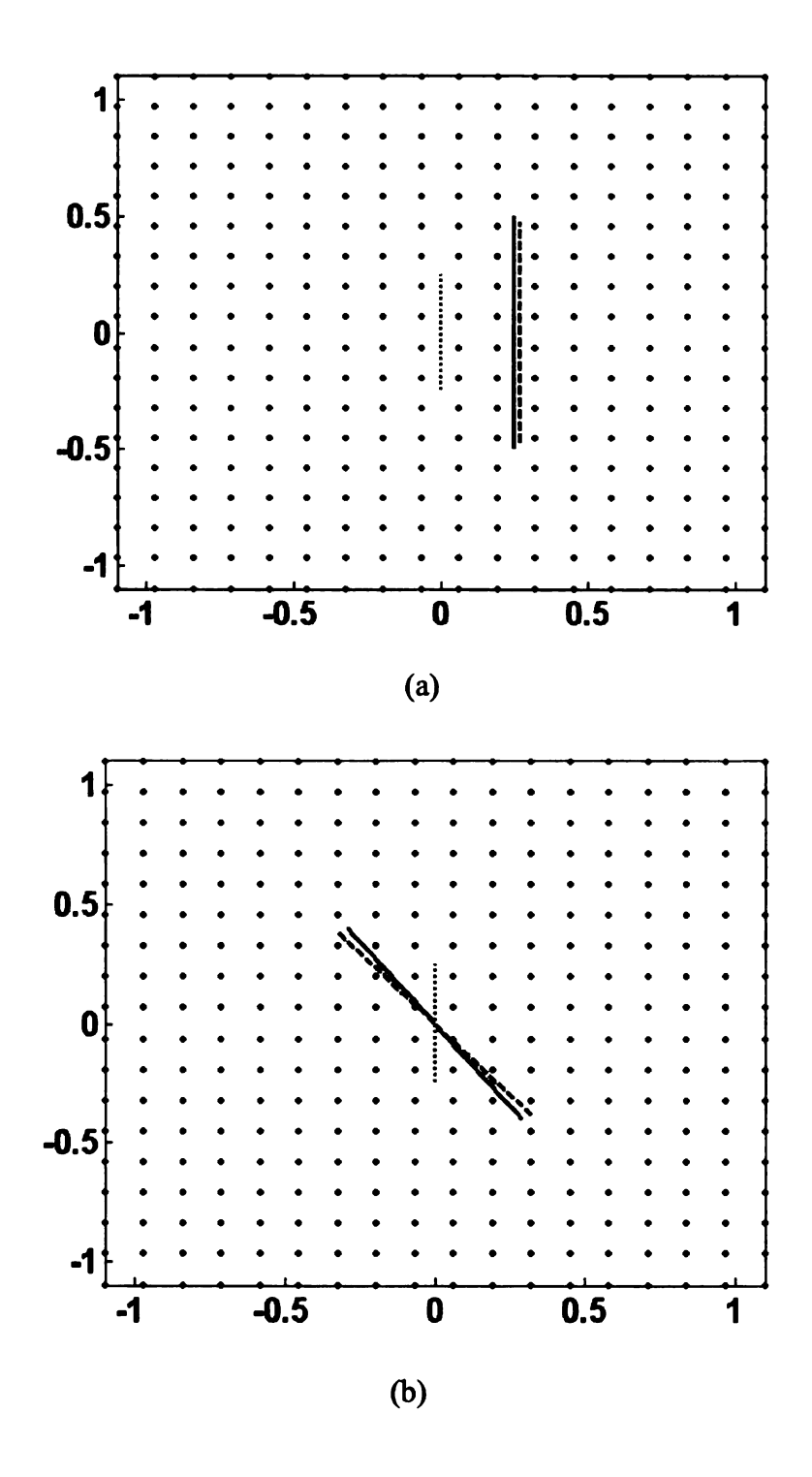


Figure 6.4 Initial guess (dotted line), the true defect (solid line) and the prediction (dashed line). (a) crack perpendicular to the current (b) crack at an angle of 55 degrees with the current direction

#### 6.2.3 Conclusion

A simple parametric inversion approach for reconstruction of a tight crack has been validated using EFG model. A calibration curve is applied to characterize the crack location, length and orientation. For this simplified problem, a simple uniform discretization in EFG model is sufficient. The inverse model is simple, fast and efficient.

## 6.3 Inversion based on State Space Search Techniques for 2D Problem

A model based inversion using EFG model and state space search method is presented in this section for 2D defect profile reconstruction. The iterative state space search method using the tree structure is developed for implementing the defect updating scheme. The inversion scheme is applied to characterize the cross-section of the defect in terms of both width and depth.

The performance is again evaluated using simulated input signals.

The approach proposed in this section comprises three major parts:

- (1) Problem representation defines the problem geometry and introduces the defect representation using state space
- (2) Search procedure uses the tree representation to search for the optimal defect
- (3) The dependence of results of cost function

# 6.3.1 Problem Representation

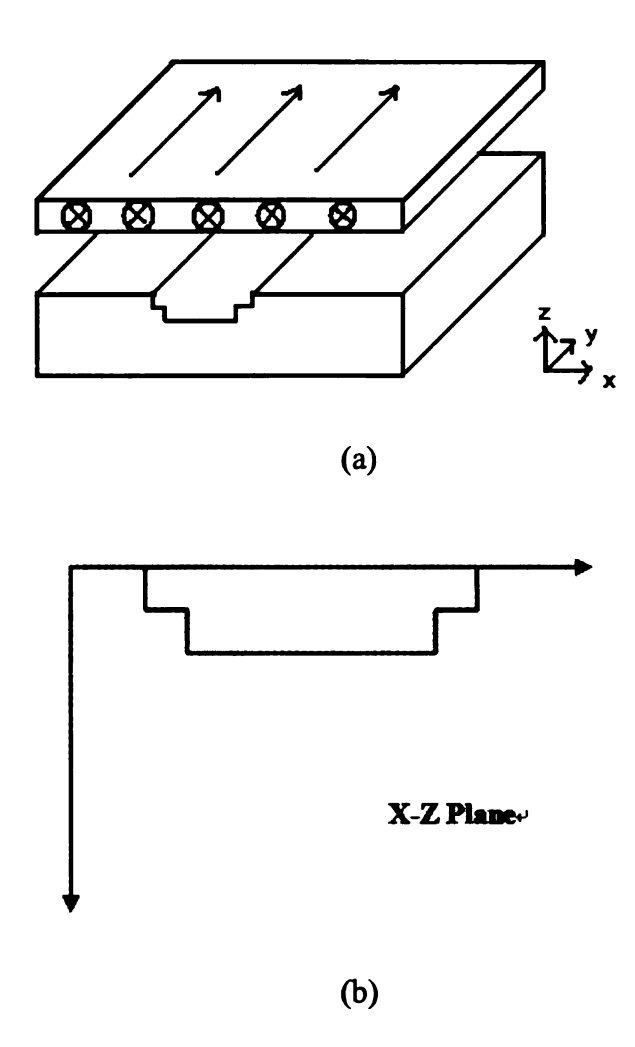


Figure 6.5 The EFG model Geometry (a) 3D View (b) cross-section view

The geometry for the inverse problem is shown in Figure 6.5. Figure 6.5 (a) shows the 3D geometry of an infinite conducting plate with a defect. The time-varying harmonic current in the y-direction is applied using a thin foil as the excitation source. Since the geometry extends to infinity in the y-direction this can be simplified to a 2D problem as shown in Figure 6.5 (b), which is the cross-section of the 3D geometry and defect profile.

In order to derive a state space [62]-[63] representation, the cross-section of the defect is discretized in terms of M discrete cells along the length and N layers of nodes along the depth into the test specimen. The state X is a M×N matrix with element 1 or 0, which represents presents or absence of a defect respectively in each cell. The set of all possible states ( $2^{MN}$ ) is the state space. Figure 6.6, shows three example states/defect profiles, where (a) and (b) are the surface defects and (c) is a sub-surface defect.

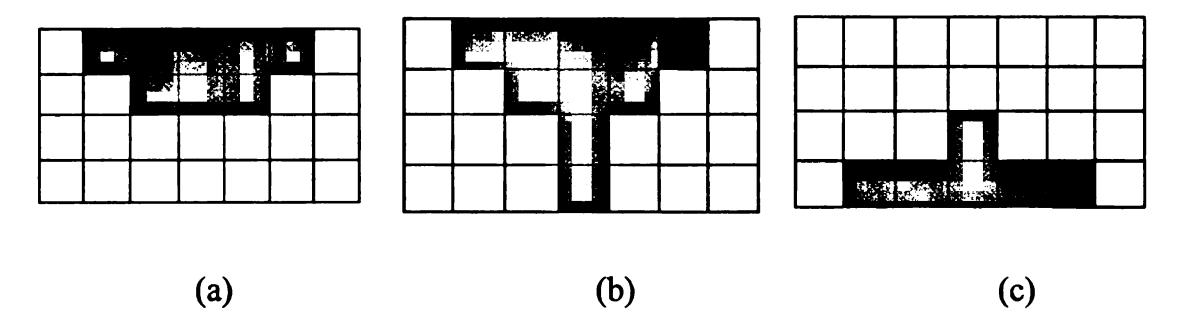


Figure 6.6 Examples of States (Defects)

An initial state describes a possible defect from which the iterative search will start.

An objective state is a defect representation that minimizes the cost function.

The search procedure is performed layer by layer. The best defect profile at each layer is obtained by minimizing the cost function, which is commonly defined as

$$F = \sum_{n=1}^{N} |B_n - B_{mn}|^2$$
(6.4)

where  $B_n$  is the model prediction of imaginary part of the normal component of magnetic flux,  $B_{mn}$  is the corresponding experimental signal and N is the number of data points in the signals. The cost function is computed for all the possible values

for cells in the current layer and the state, corresponding to the lowest cost function is selected in each layer.

#### 6.3.2 Tree Structure

In order to derive the solution to the inverse problem, we search for a simple best-fit defect state to minimize the difference between the signals corresponding to true and reconstructed defects. The exhaustive search procedure is summarized using a tree structure, which is shown in Figure 6.7.

The search is constrained by two assumptions, namely, (a) the defect grows vertically downwards. (b) the defect grows narrower with depth.

An initial node d<sup>(0)</sup> is chosen as the initial state in the tree structure. In each layer, the nodes are expanded, and the cost function of each node is computed and the node corresponding to the minimum cost function is selected and retained for expansion to the next layer. In Figure 6.7, the node inside the square represents the selected minimum cost nodes in each layer.

The tree expansion continues, until a leaf node is reached. The criterion to obtain the leaf node is based on the calculation of the cost function. As the tree expanded to a next layer, if the minimum cost function begins to increase, then the search stops, and the selected node in the current layer corresponds to the global minimum cost function and is labeled as the leaf node. Once a leaf node is obtained, the search procedure stops and the solution state is reached. In Figure 6.7, the cost function of the bottom layer gray node is seen to be greater than the minimum cost function of the

parent node in the previous layer. The node inside the square is the desired defect profile.

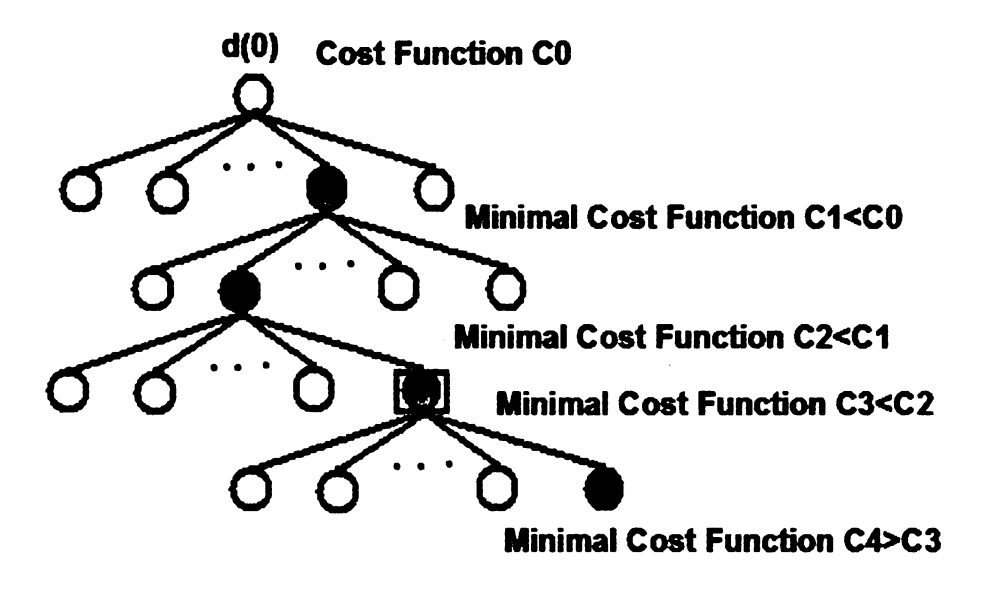


Figure 6.7 the tree structure

#### 6.3.3 The Search Procedure

The detailed search procedure is divided into the following steps:

- 1. Estimation of the initial state  $d^{(0)}$ . involves determining the defect location i.e. whether the crack is on the top or bottom surface.
- (a) Use simple peak detection algorithm to determine the defect location. The peak-to-peak separation in the input signal is used to estimate the defect length in the initial layer.

Figure 6.8 (a) Input signal (b) initial guess of top surface defect (c) initial guess of bottom surface defect

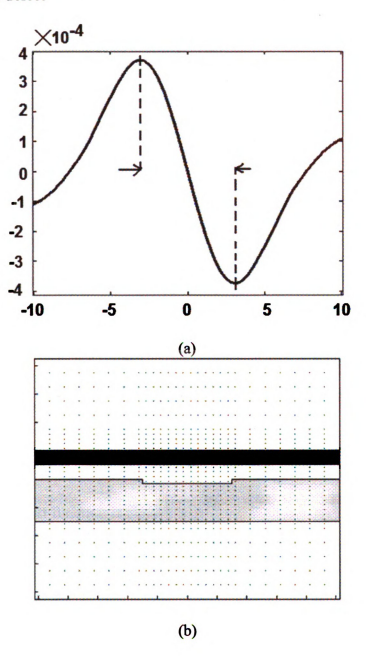
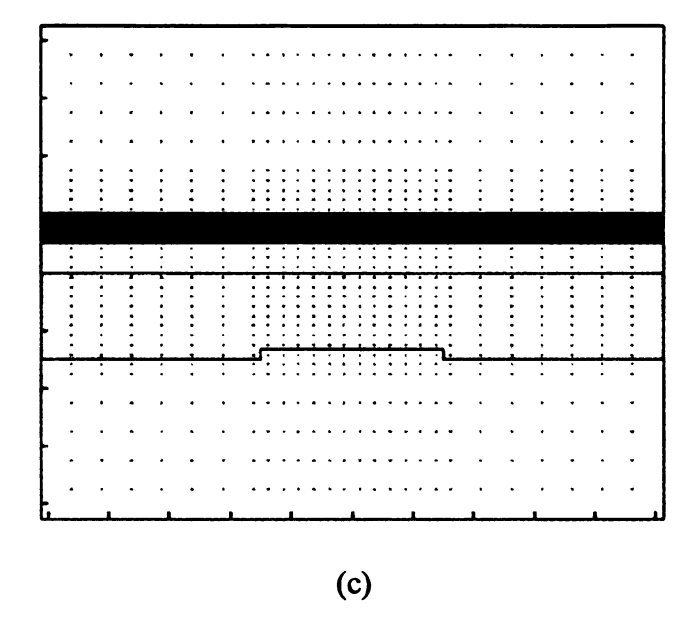


Figure 6.8 continued

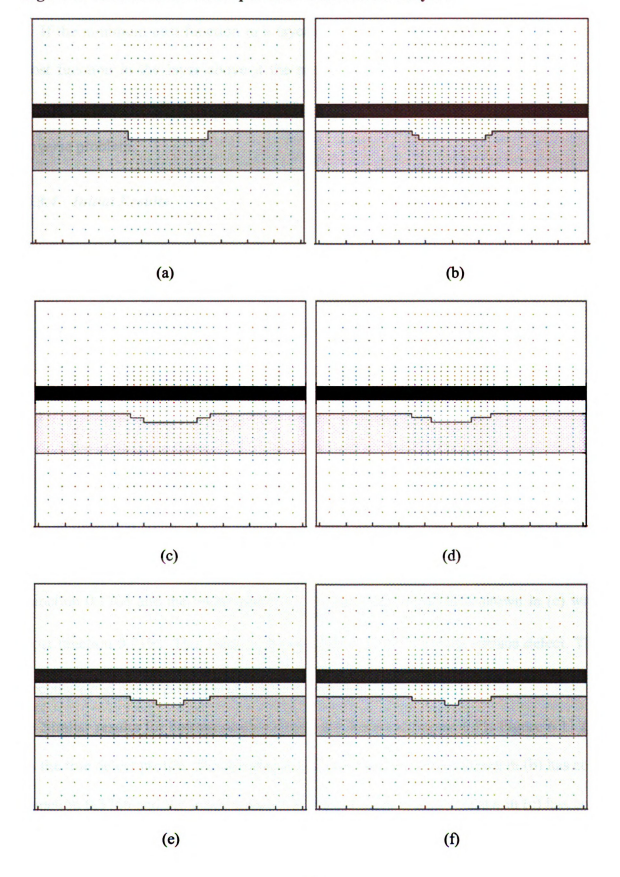


(b) In Figure 6.8, (a) represents the input signal, and the peak-to-peak separation of the signal is from -3 mm to 3 mm, which means the defect length of the initial state is -3 mm to 3 mm. The location of the defect of length 6 mm could be on the top or bottom surface as shown in Figures (b) and (c). These two defect geometries are simulated and the signals are generated. The cost functions are calculated and the model with lower cost function is chosen as d<sup>(0)</sup>.

# 2. Profiling the defect depth

Perform exhaustive search in the each layer. Generate the possible allowed defect shapes in current layer using the defect assumptions and estimate the defect boundary corresponding to the minimum cost function. As shown in Figures 6.9 (a) through (f), the possible defects are generated and modeled. Cost function associated with each node is computed.

Figure 6.9 Candidate defect shapes used in the search in layer 2



#### 3. Check for stopping criteria

If the minimum cost function in a layer is larger than the corresponding minimum cost function in the layer above it the search stops. The geometry with the global minimum cost function provides the desired defect profile or the solution to the inverse problem.

#### 6.3.4 Initial Results

The inversion strategy is implemented and the results corresponding to two defect profiles are presented. Linear excitation current of 3 kHz frequency is applied along the x-axis as shown in Figure 6.5 (a). The upper strip region is the current foil. The lower strip region represents a section of the aluminum plate. The background dots are the discretization nodes of the background mesh used in the EFG model. As before the units are in mms.

The cost function is defined as in equation (6.4).

The measured signal shown in Figure 6.8 (a) is obtained for the true defect profile in Figure 6.10 (a). The initial guess of a top surface defect is shown in (b) with cost function 0.1708 and the initial guess of a bottom surface defect is shown in (c) with cost function 0.3198. This leads to the estimation of d<sup>(0)</sup> as a top surface defect. The reconstructed defect profile is shown in Figure 6.10 (d).

Similar results for bottom surface defect are shown in Figure 6.11. Figure 6.11 (a) is the true defect profile. The initial guess of a top surface defect shown in (b) has cost function 0.3766 and the initial guess of a bottom surface defect shown in (c) has cost

function 0.1770, so that the initial defect profile is determined as a bottom surface defect.

When the given input signal is noise free, the reconstructed defect profile is exactly equal to the true profile.

Figure 6.10 (a) True defect profile and (b) initial guess of a top surface defect (c) initial guess of a bottom surface defect (d) reconstructed results for top surface defect

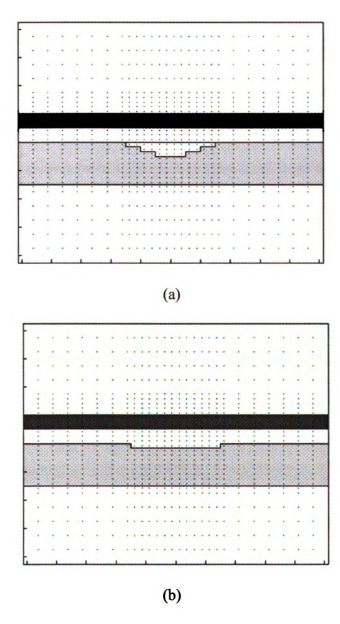


Figure 6.10 continued

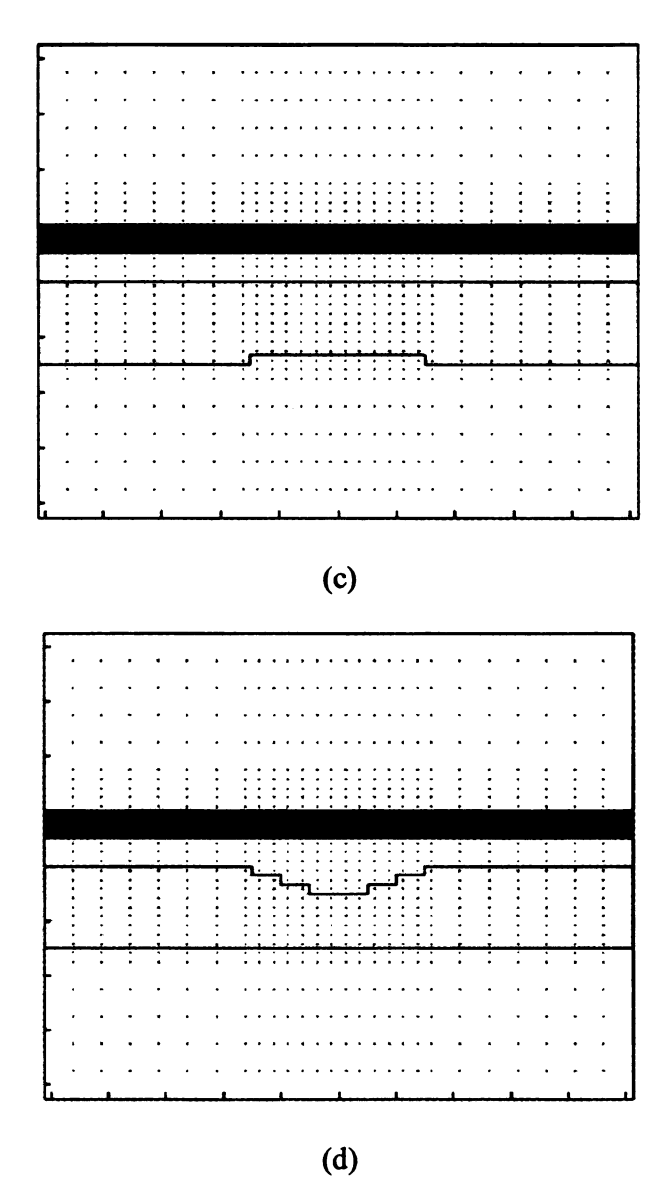


Figure 6.11 (a) True defect profile and (b) initial guess of a top surface defect (c) initial guess of a bottom surface defect (d) reconstructed result for bottom surface defect

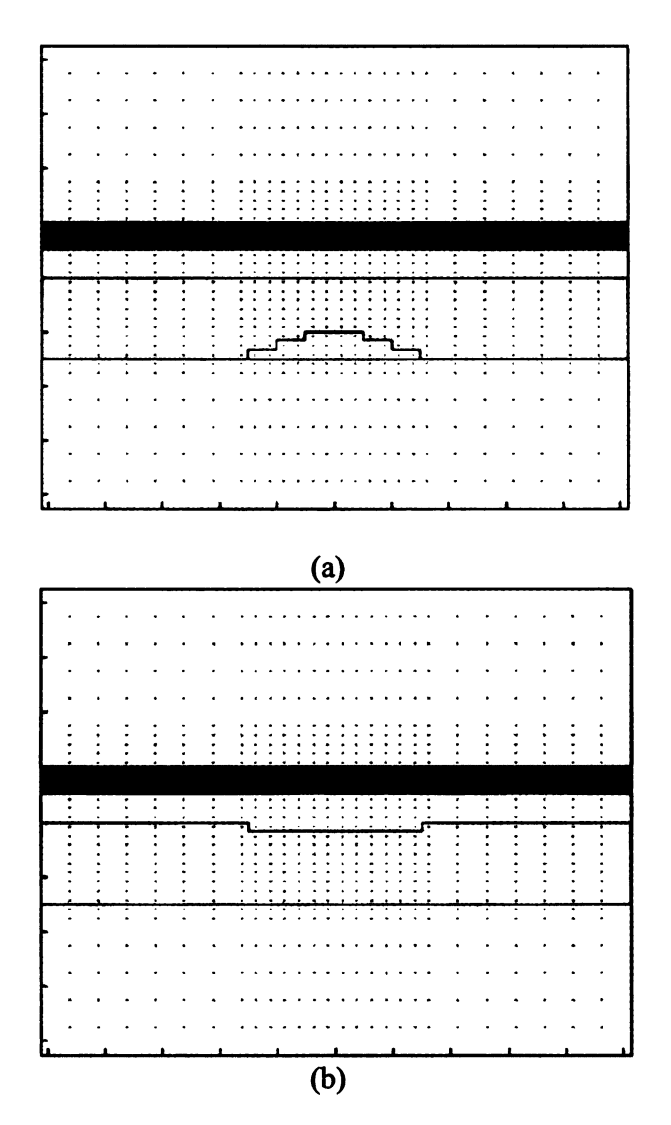
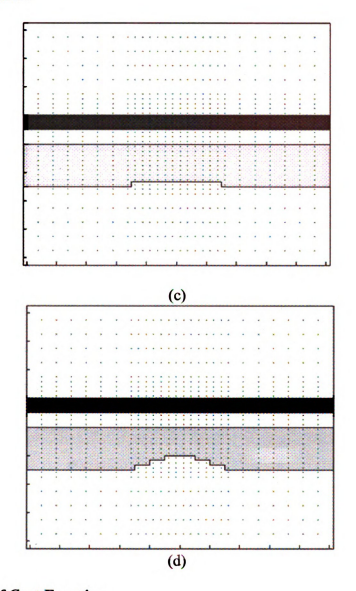


Figure 6.11 continued



#### 6.3.5 Choice of Cost Function

The objective of inverse problem is to estimate the "best" profile of the detected defect, that minimizes the cost function. Hence different cost functions may lead to different resultant profiles. Hence we need to choose cost function with care.

The cost function acts as the evaluation function to describe the error between the model prediction and input signal, which is obtained from the true defect geometry. The most commonly used cost function is based on the  $L_2$  norm defined as

$$F = \sum_{n=1}^{N} |B_n - B_{mn}|^2$$
(6.5)

where  $B_n$  is the model prediction of imaginary part of the normal component of magnetic flux density,  $B_{mn}$  is the corresponding measured signal and N is the number of data points in the signals. The search algorithm developed in the above section is implemented using the cost function defined in Equation (6.4). However this definition does not yield the best results in all cases. An alternative cost function that can be employed is the  $L_{\infty}$  (or Chebychev) norm:

$$F = \max(|B_n - B_{mn}|), i = 1, 2, ... K$$
(6.6)

This cost function is defined as the maximum difference between the input signal and model prediction, among all the data points. The search algorithm is performed with the new cost function. The results show that the new cost function yields more accurate defect profiles than the previous cost function when the defect under consideration is very deep.

Two true defect profiles of larger depth are shown in Figures. 6.12, where Figure 6.12 (a) is top surface defect and 6.12 (b) is bottom surface defect. The reconstructed top surface defect profile obtained with the  $L_2$  cost function in equation (6.5) is

shown in Figure 6.13 (a), and the corresponding result obtained with the new  $L_{\infty}$  cost function in equation (6.6) is shown in Figure 6.13 (b). When the given input signal is noise free, the reconstructed defect profile is seen to be exactly the same as the true profile using the new cost function. The old cost function does not converge to the desired defect profile. Similar results for bottom layer defect are shown in Figure 6.14 (a) and (b), with the old and new cost functions respectively. The reconstructed defect profile gives the true profile using the new cost function.

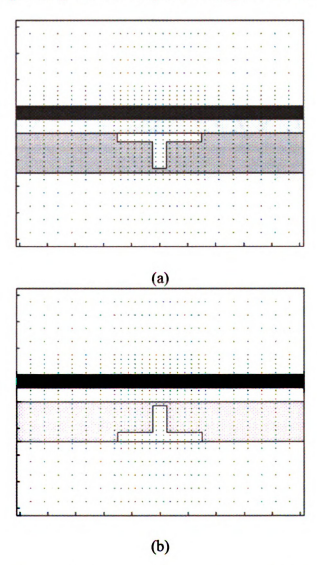


Figure 6.12 True defect profile (a) top surface (b) bottom surface

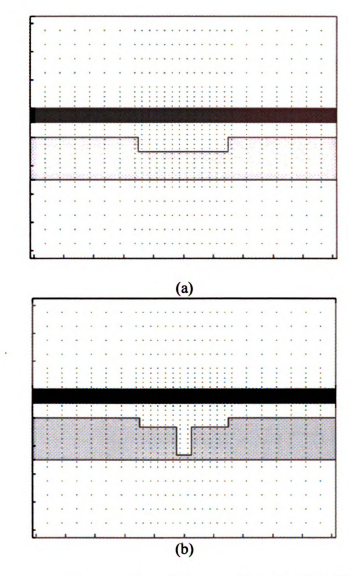


Figure 6.13 Reconstructed top surface defect profiles (a) with old cost function (b) with new cost function

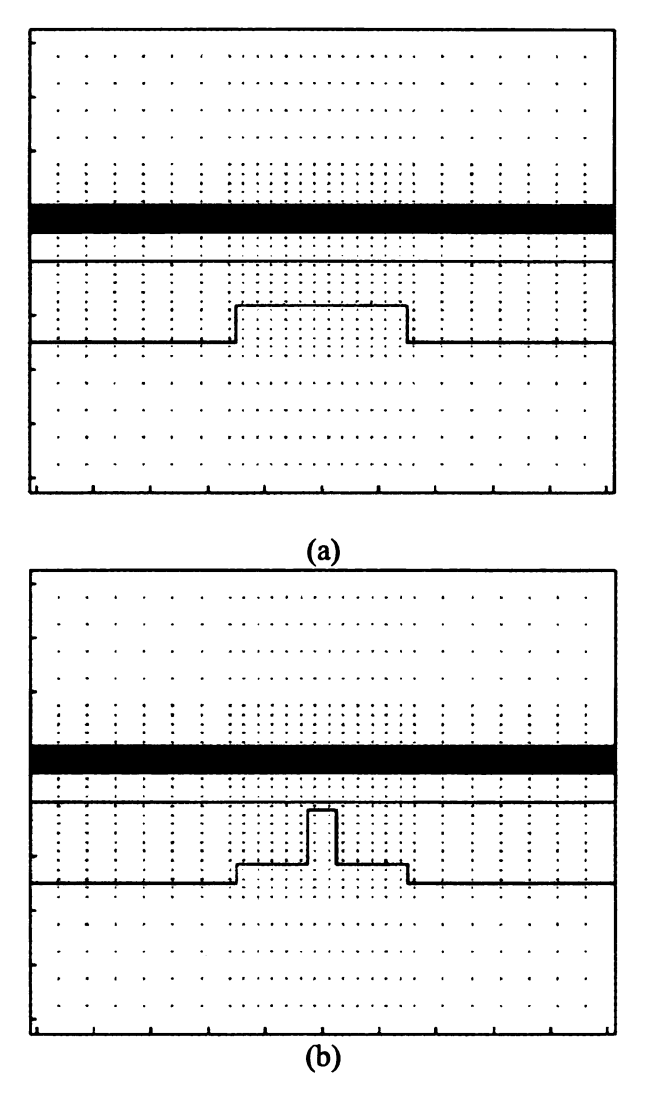


Figure 6.14 Reconstructed bottom surface defect profiles (a) with old cost function (b) with new cost function

#### 6.3.6 Conclusion

An inversion technique using a tree search algorithm is presented and validated for a 2D eddy current problem with foil excitation. Both the surface and subsurface defects are reconstructed using the state space search. The reconstructed defect is shown to be dependent on the choice of cost function minimized.

Implemented of the technique on experimental signals is currently underway. The performance and robustness of the inversion technique will then be evaluated on field signals from aircraft inspection.

# 6.4 Inversion based on Gradient Search using Adjoint Equation for 2D Problem

This section presents a defect update approach that makes use of a gradient search of the multi-dimensional error surface so that the reconstructed defect profile will result in a signal that matches the given measured signal in the least squares sense. As shown in section 6.3, currently, the performance is evaluated for the simulated input signals.

In the gradient based minimization algorithm, the evaluation of the gradient is essential. To evaluate the gradient of the objective function, each of the partial derivatives must be evaluated appropriately. The commonly used methods solve the governing equations each time to calculate each of the partial derivatives. This will result in a long computational time. To solve this problem, an adjoint equation [64] based method is proposed to find all the partial derivatives by solving the governing equations only once. The method reduces the computational time significantly.

When the EFG method is used as forward model, when the defect is updating, the background discretization nodes remain unchanged and only a few nodes to represent the defect parameters need to be updated. This will greatly speed up the forward computation and reduce the time needed in iterative inversion.

This method as well as its robustness is discussed in this section. Preliminary results validating the approach are presented.

#### 6.4.1 The Inversion Scheme in 2D

The overall iterative approach is the same as that shown in Figure 6.1. The geometry for two-dimensional inverse problem is shown in Figure 6.5 along with the x-, y-, z- directions. The defect is represented in terms of nodal coordinates which determines the defect profile on the boundary.

The inverse problem solution is the profile that is obtained by minimizing the cost function is defined as

$$F = \sum_{n=1}^{N} |B_n - B_{mn}|^2$$

(6.7)

where  $B_n$  is the model prediction of imaginary part of the normal component of magnetic flux,  $B_{mn}$  is the corresponding input signal and N is the number of data points in the signals. The cost function is computed for each defect profiles and the best defect profile is selected corresponding to the lowest cost function. The iteration stops when the cost function is minimized and begins to increase.

A typical iteration scheme consists of four components:

- 1. a set of state variables  $\varphi$ ;
- 2. a set of defect parameters X;
- 3. an objective function  $J(\varphi, X)$ ;

4. constraint equations  $F(\varphi, X) = 0$ .

In the above 2D problem,  $\varphi$  represents the magnetic vector potential in the forward model. The defect parameters X are the nodal coordinates defining the defect profile. The objective function is the cost function F in equation (6.7).

The constraint equations is the governing partial differential equation in terms of the parameter set X and unknown  $\varphi$ . The matrix equation obtained in the EFG method is written as

$$F(\varphi, X) = K.\varphi - S = 0 \tag{6.8}$$

where matrix K is the stiffness matrix and S is the source vector.

So the problem can be stated as: iteratively solve the set of equations (6.8) for the defect parameters X such that the objective function  $J(\varphi, X)$  is minimized, subject to the constraint equations  $F(\varphi, X) = 0$ .

The commonly used gradient search method is summarized as follows:

- 1. Assume an initial defect parameter set  $X^{(0)}$
- 2. Solve the constraint equation (6.8), and calculate the predicted signal  $B_i$ , for i=1,2,...M. Calculate the objective function from equation (6.7).
- 3. Compute the gradient of the objective function  $\nabla J$  over X, and determine  $\delta X^{(n)}$  an updating step.
- 4. Update the defect parameters  $X^{(n+1)} = X^{(n)} + \delta X^{(n)}$ .

5. Repeat from step 2, until the cost function is minimized and the stopping criterion is reached.

The details of step 3 are presented below:

Assume 
$$X = [x_1, x_2, ..., x_m]^T$$
 and  $\nabla J = [\frac{\partial J}{\partial x_1}, \frac{\partial J}{\partial x_2}, ..., \frac{\partial J}{\partial x_m}]^T$ 

For each 
$$x_k, k = 1, 2, \dots, m$$
,  $\frac{\partial J}{\partial x_k} = \sum_j \frac{\partial J}{\partial \varphi_j} \cdot \frac{\partial \varphi_j}{\partial x_k} = \left[\frac{\partial J}{\partial \varphi}\right] \cdot \left[\frac{\partial \varphi}{\partial x}\right]$  (6.9)

where  $\left[\frac{\partial J}{\partial \varphi}\right] = \left[\frac{\partial J}{\partial \varphi_1}, \frac{\partial J}{\partial \varphi_2}, \dots, \frac{\partial J}{\partial \varphi_n}\right]^T$ , and n is the number of the unknown  $\varphi$ .

In equation (6.9),  $\left[\frac{\partial \varphi}{\partial x}\right]$  can be easily obtained by differentiating equation (6.8), which gives:

$$[K] \cdot \left[ \frac{\partial \varphi}{\partial x_k} \right] + \left[ \frac{\partial K}{\partial x_k} \right] [\varphi] = 0$$
(6.10)

We also need to compute  $\left[\frac{\partial J}{\partial \varphi}\right]$ , which is done using the adjoint equation [60]. A

constrained cost function  $L(\varphi, X, \wedge)$  is defined by (6.11) as

$$L(\varphi, X, \wedge) = J(\varphi, X) - \langle F(\varphi, X), \wedge \rangle$$
(6.11)

where  $\wedge$  is a set of Lagrangian multipliers. Differentiating equation (6.11) w.r.t. the unknowns we get:

$$\frac{\partial L}{\partial \wedge} = 0 \Rightarrow F(\varphi, X) = 0 \tag{6.12}$$

$$\frac{\partial L}{\partial X} = 0 \Rightarrow \left[ \frac{\partial F}{\partial X} \right] \cdot \left[ \wedge \right] = \left[ \frac{\partial J}{\partial X} \right]$$
(6.13)

$$\frac{\partial L}{\partial \varphi} = 0 \Rightarrow [K]^T \cdot [\wedge] = \left[\frac{\partial J}{\partial \varphi}\right]$$
(6.14)

By substituting (6.13) and (6.14) into equation (6.9), the derivative can be obtained as:

$$\frac{\partial J}{\partial x_k} = [\wedge]^T \cdot [K] \cdot \left[ \frac{\partial \varphi}{\partial x_k} \right] = -[\wedge]^T \cdot \left[ \frac{\partial K}{\partial x_k} \right] \cdot [\varphi]$$
(6.15)

In the gradient search method,  $\delta X^{(n)} = \left[\frac{\partial J}{\partial x_1}, \frac{\partial J}{\partial x_2}, \dots, \frac{\partial J}{\partial x_m}\right]^T$ , so the updating is performed using equation (6.15).

For simplification, we assume the Lagrange multiplier  $\wedge$  is a constant number in each iteration step. Hence equation (6.15) is rewritten as  $\frac{\partial J}{\partial x_k} = -c \cdot \left[ \frac{\partial K}{\partial x_k} \right] \cdot [\varphi]$ , where c is a small constant number, chosen to be equal to 0.1.

#### 6.4.2 Results

The implementation of the above iteration procedure is presented here.

The true defect profile in the aluminum sample (lower strip region) and the excitation current foil (upper strip region) are shown in Figure 6.15 (a). The desired defect is a rectangular defect with the width extending from -0.45 mm to 0.45 mm, and with height 1.0 mm. The initial guess is a crack-free situation as shown in Figure 6.15 (b). The background nodes are the discretization nodes in the EFG method.

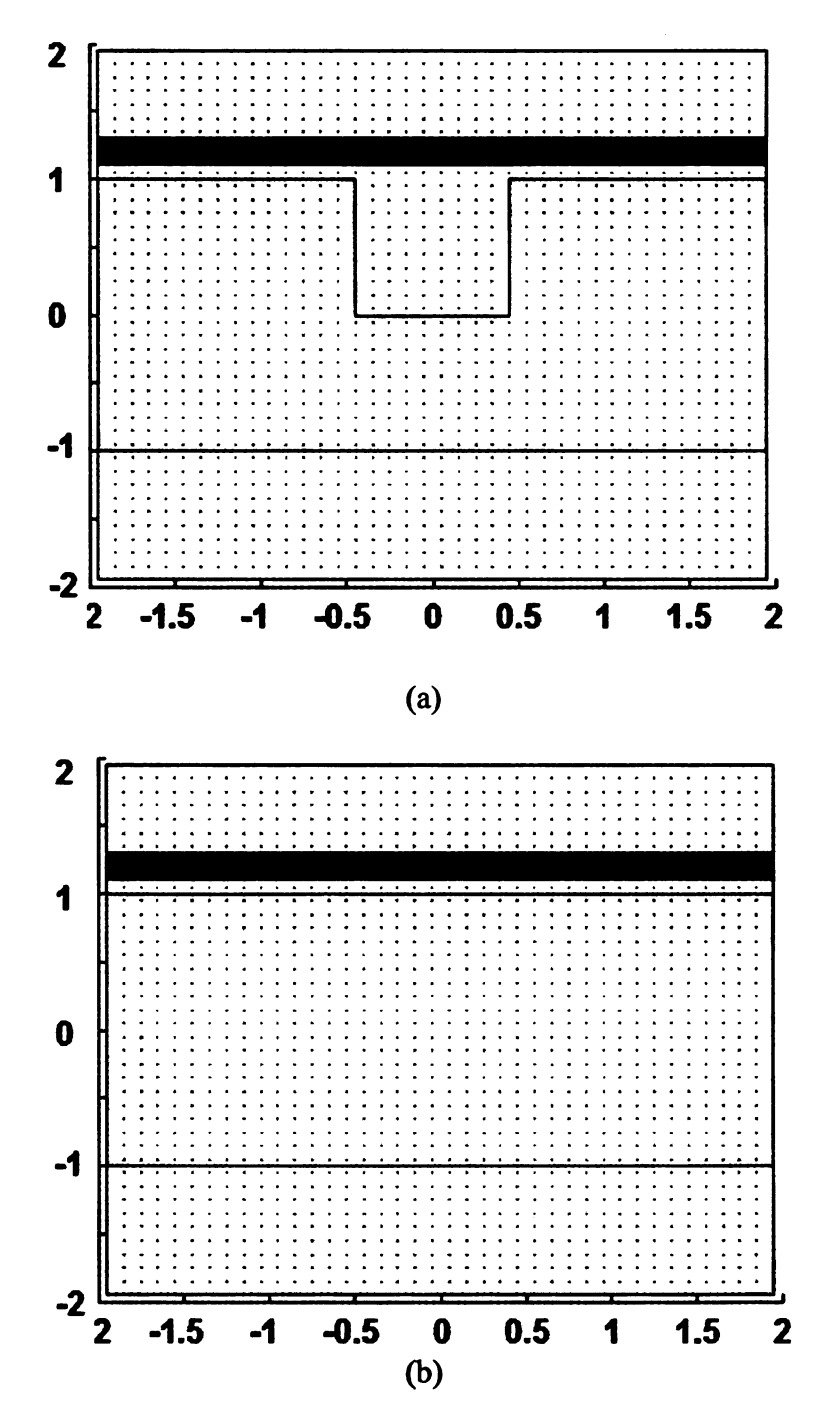


Figure 6.15 (a) The desired defect profile. (b) the initial guess

The iteration steps are summarized below:

- I. Determination of defect location and parameter X
- (a) Assume the crack is surface-breaking (top surface).

- (b) The width of the defect on top surface is determined by the distance between two peaks in the input signal, which is around -0.45 mm to 0.45 mm.
- (c) We assume four nodal points to represents the defect profile. The defect parameter X is defined as  $X = \{x_1, x_2, x_3, x_4, z_1, z_2, z_3, z_4\}$ . For simplification of calculation, the x-coordinates are fixed and equally spaced according to the width of the defect on the surface. So the x-coordinates in this example are -0.45 mm, -0.15 mm, 0.15 mm, and 0.45 mm. The z-coordinates are the variables that need to be optimized.

In Figure 6.16 (a), the four black points represents the position of the initial guess of the defect parameter X.

II. Updating the z-coordinates

(d) From the simplified equation (6.15),  $\frac{\partial J}{\partial z_k} = -c \cdot \left[ \frac{\partial K}{\partial z_k} \right] \cdot [\varphi]$ , the coordinates are

updated as  $Z^{(n+1)} = Z^{(n)} + \frac{\partial J}{\partial z_k^{(n)}}$ . Where the derivative of the matrix K is

calculated numerically as  $\left[\frac{\partial K}{\partial z_k}\right] = \frac{K(z_k + \Delta z_k) - K(z_k)}{(z_k + \Delta z_k) - z_k}$ , here we assume  $\Delta z_k = 0.001$ .

Figures 6.16 (b) to (k) show evolution of four point the defect profile in each iteration.

## III. Check for stopping criteria

(e) In each updating step, the cost function is calculated using equation (6.7). If the cost function keeps decreasing, the searching procedure continues. When the cost

function starts to increase, the iteration procedure stops and the optimum defect profile is obtained corresponding to the minimum cost function.

In Figure 6.16 (1) the optimum defect profile is obtained corresponding to the minimum cost function.

Figure 6.16 The updating status of the defect profile

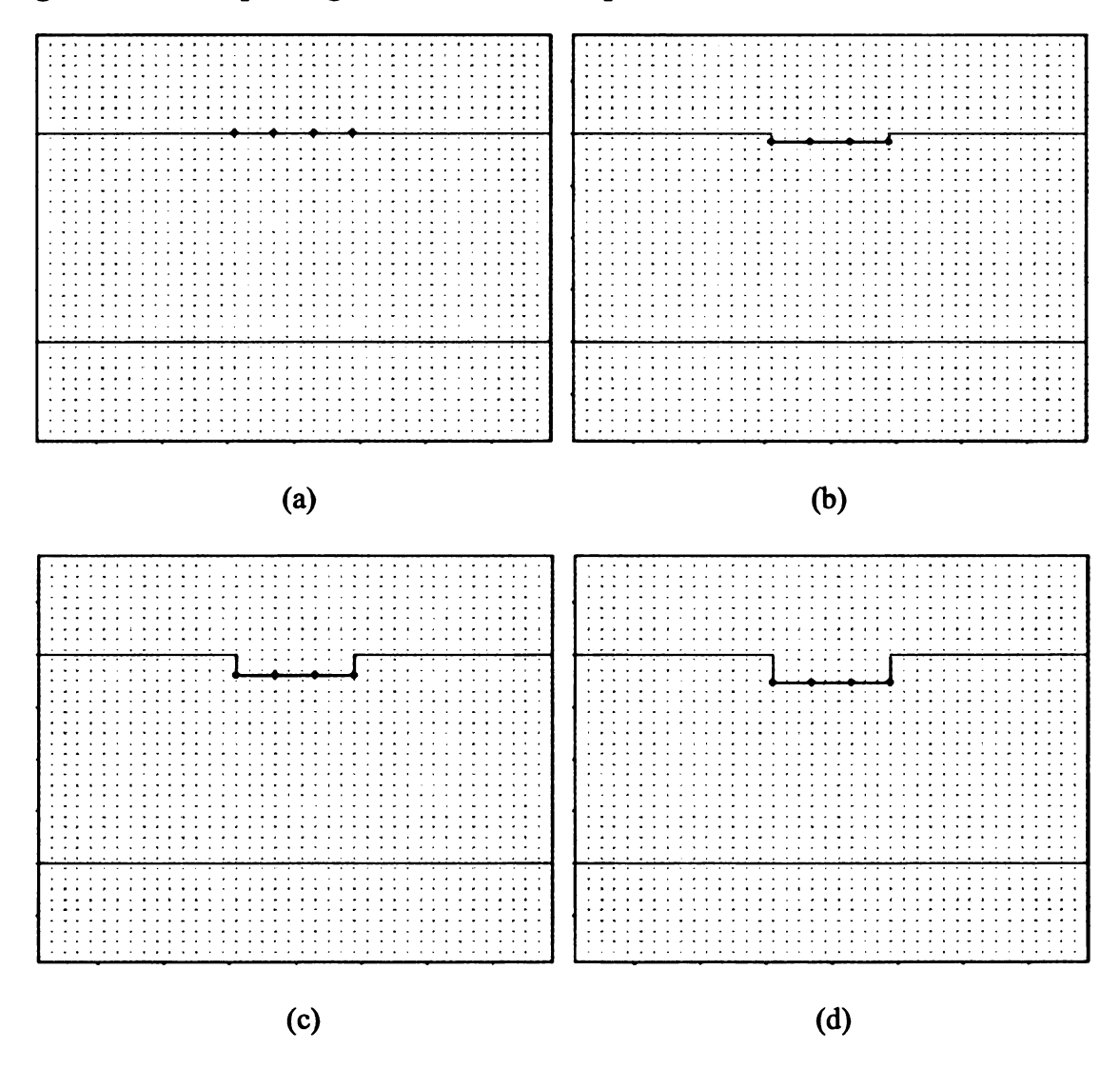


Figure 6.16 continued

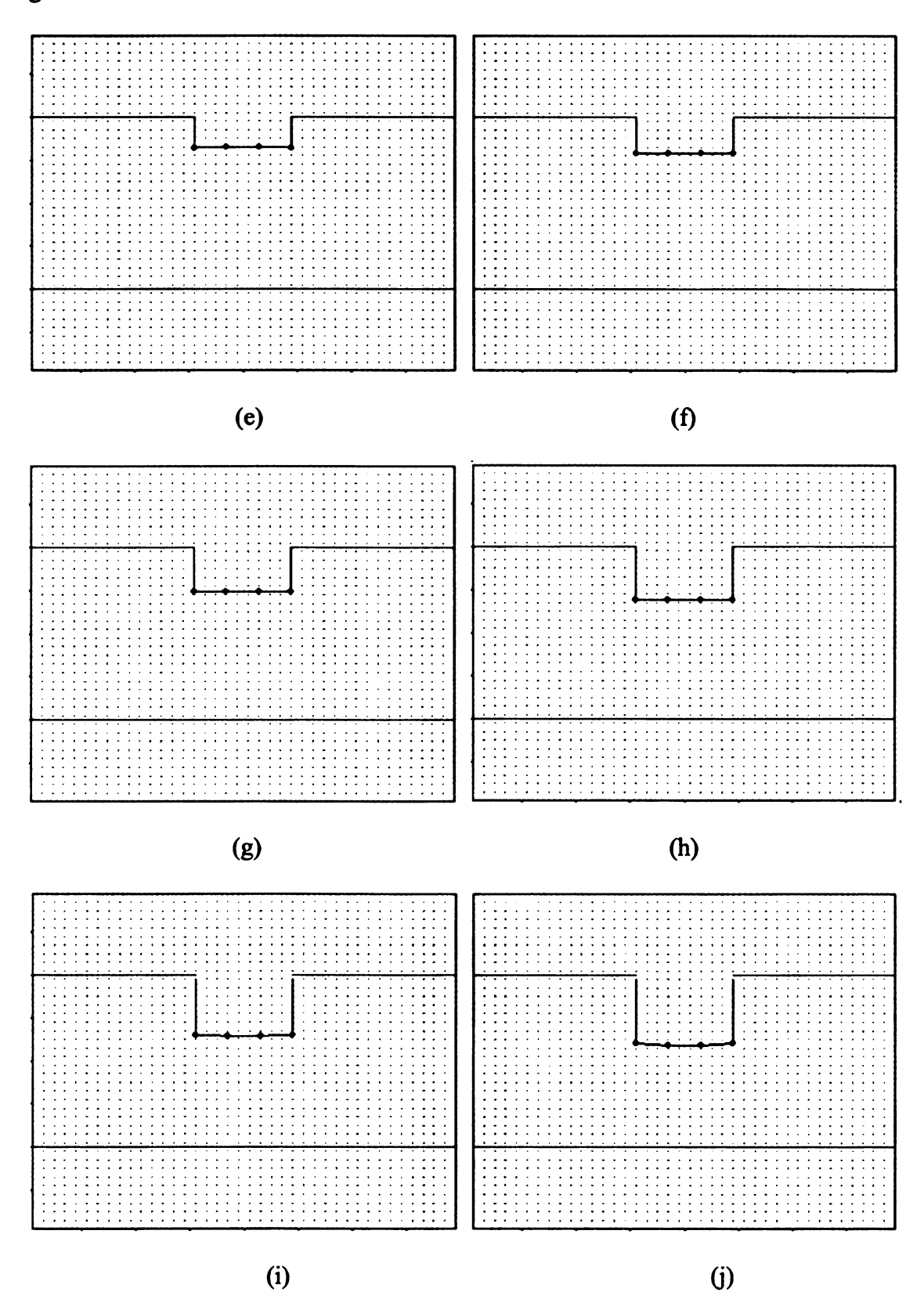
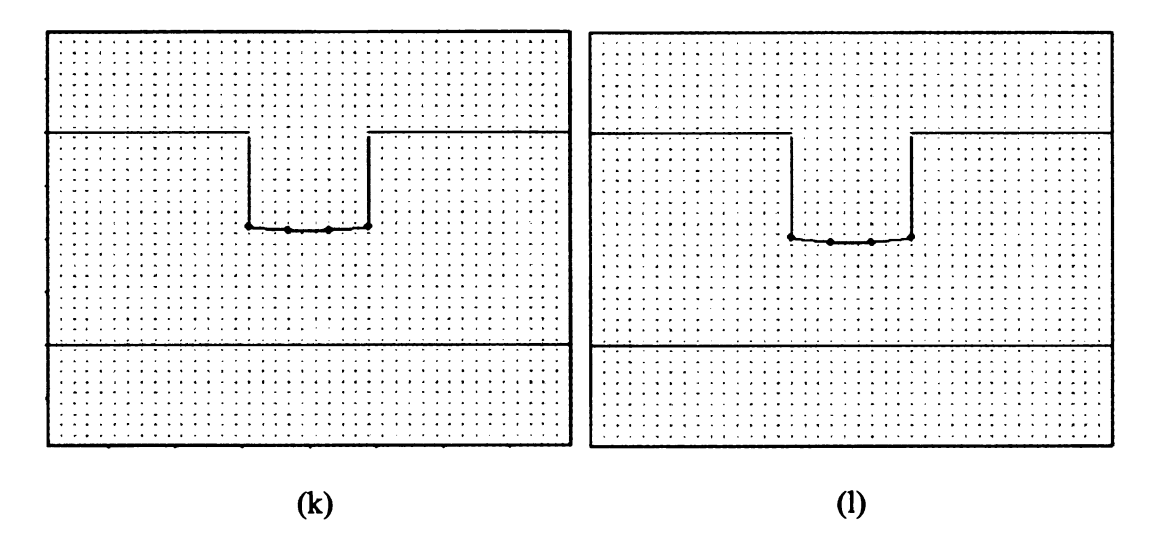


Figure 6.16 continued



# 6.4.3 Effect of Noise Level

The above initial results are obtained when the input signal is noise free. While in realistic problems, the noise level cannot be neglected. The effect of noise on the performance of the gradient search method is studied to test the robustness of the inversion scheme. Random white noise varying from 5% to 30% of the peak signal value was added to the model predicted signal and the corresponding reconstruction defects were generated.

The true defect profile is shown in Figure 6.17.

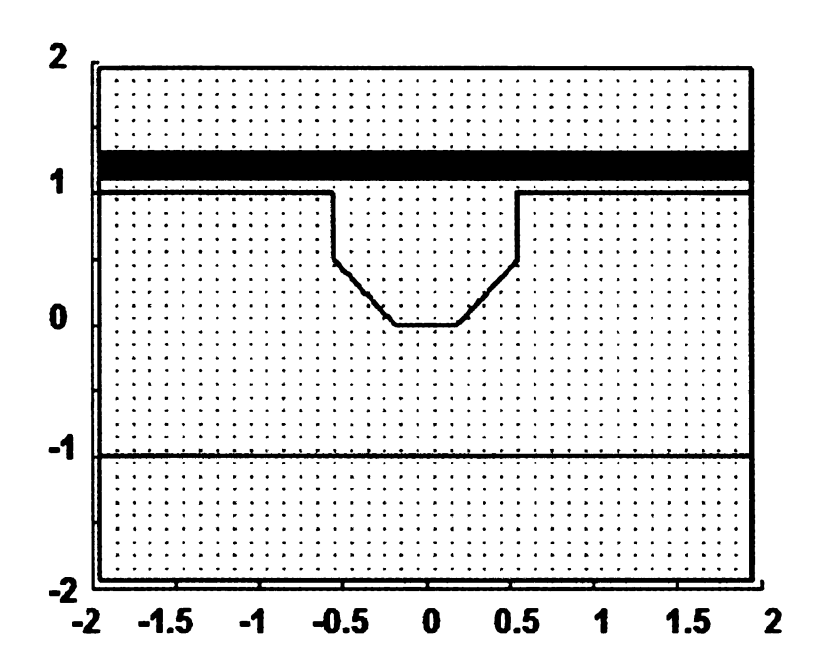


Figure 6.17 True defect

Figures 6.18 (a) to (f) show the signals corrupted with 5.0%, 10.0%, 15.0%, 20.0%, 25.0% and 30.0% random noise.

Figure 6.18 The signal corrupted with (a) 5.0%. (b) 10.0%. (c) 15.0%. (d) 20.0%. (e) 25.0%. (f) 30.0% random noise

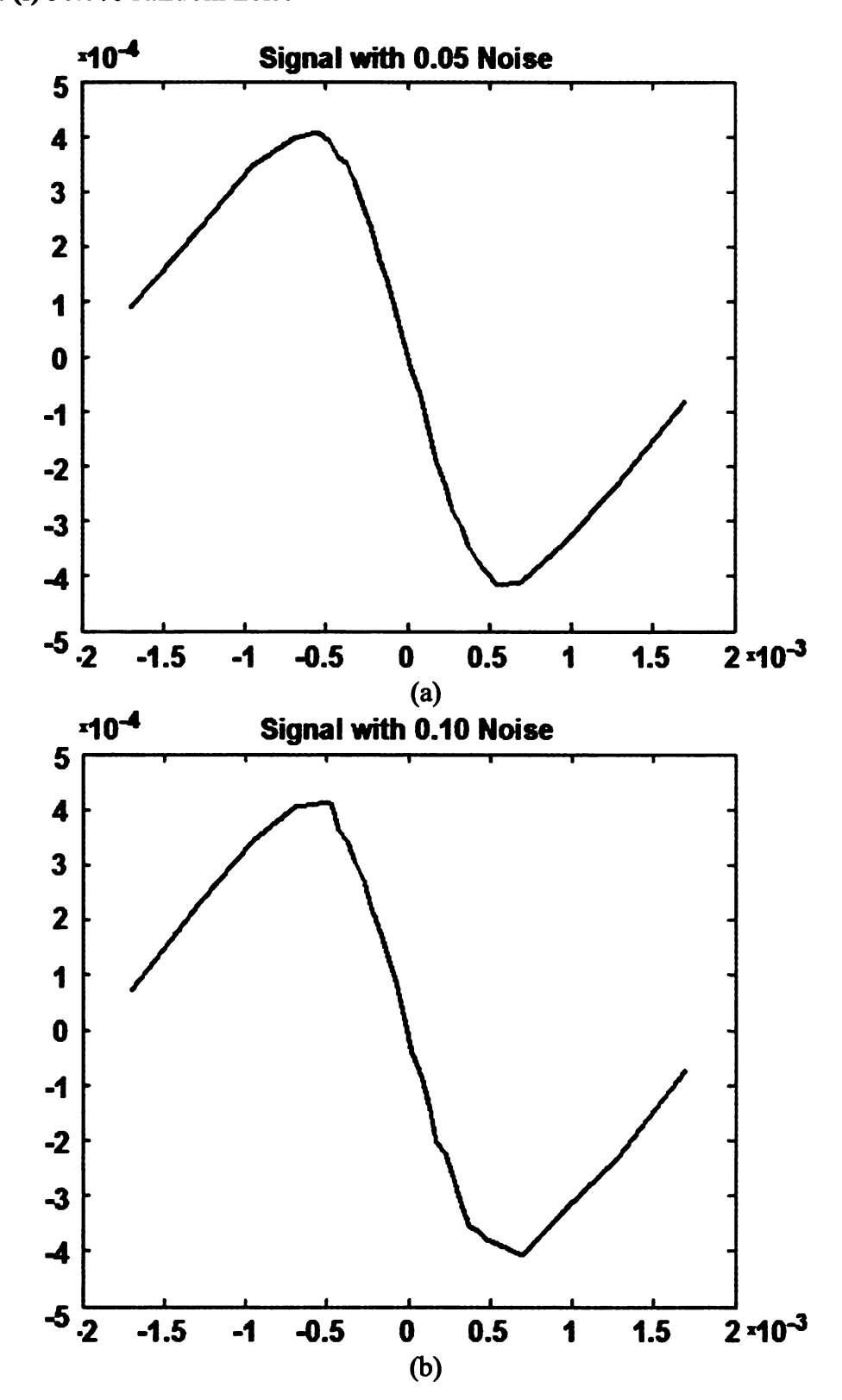
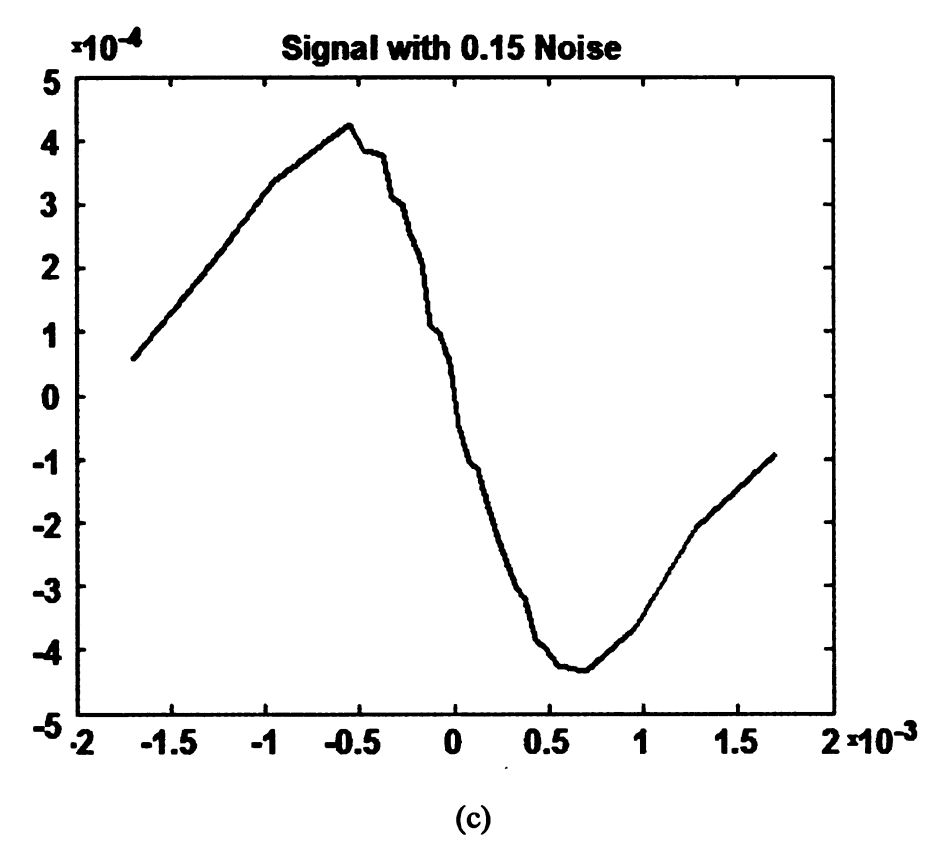


Figure 6.18 continued



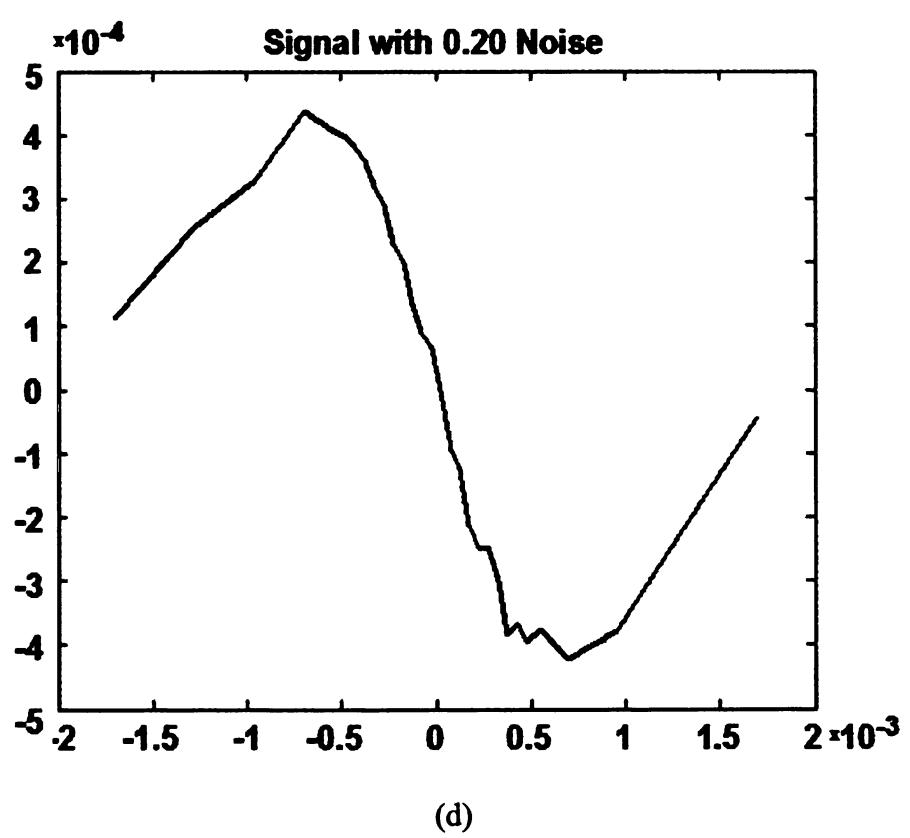
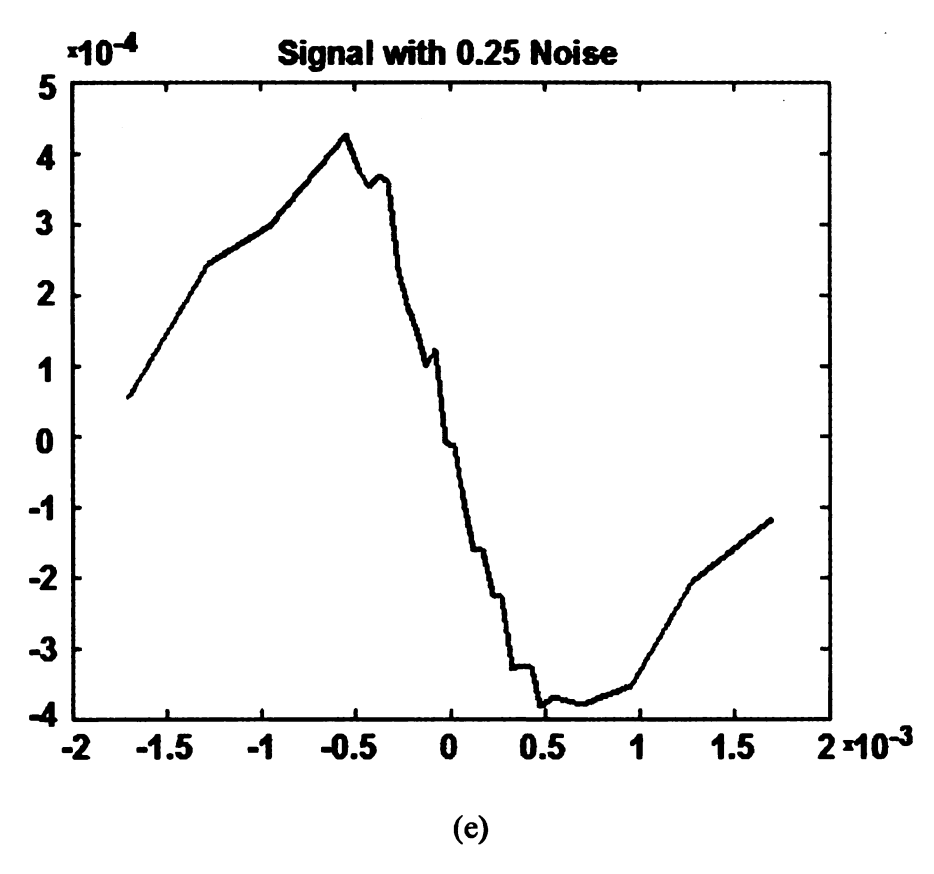
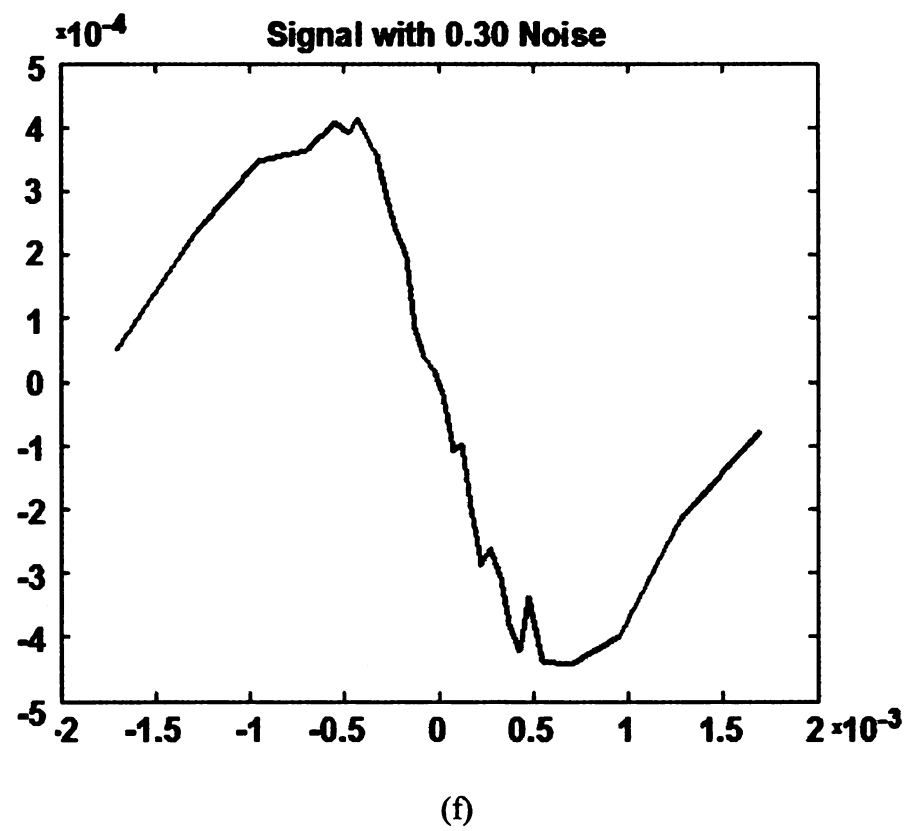


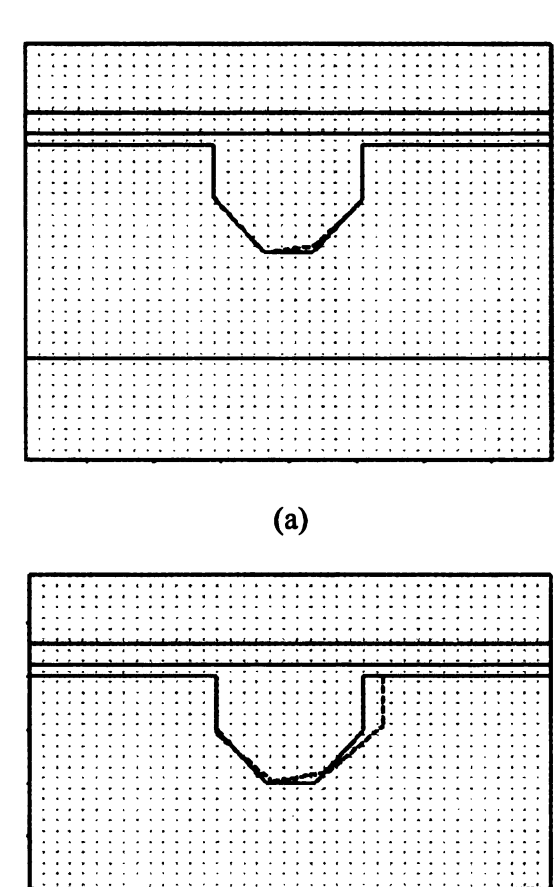
Figure 6.18 continued





Figures 6.19 (a) to (f) show the reconstructed defect profiles (dashed lines) corresponding to the signals in Figure 6.18 which are corrupted with 5.0%, 10.0%, 15.0%, 20.0%, 25.0% and 30.0% random noise. The true defect is plotted in the same figure (solid lines) for comparison.

Figure 6.19 (a) to (f) The reconstructed defect profile (dashed lines) when the signal is corrupted with (a) 5.0%. (b) 10.0%. (c) 15.0%. (d) 20.0%. (e) 25.0%. (f) 30.0% random noise



(b)

Figure 6.19 continued

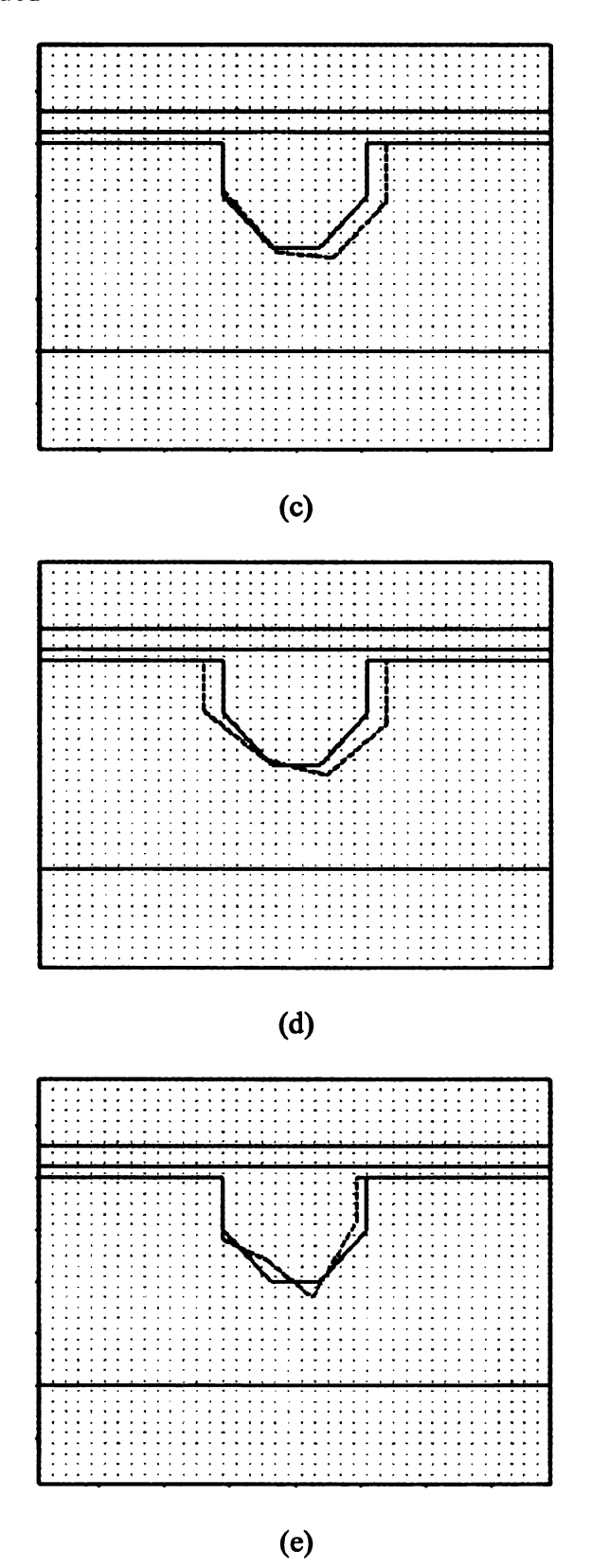
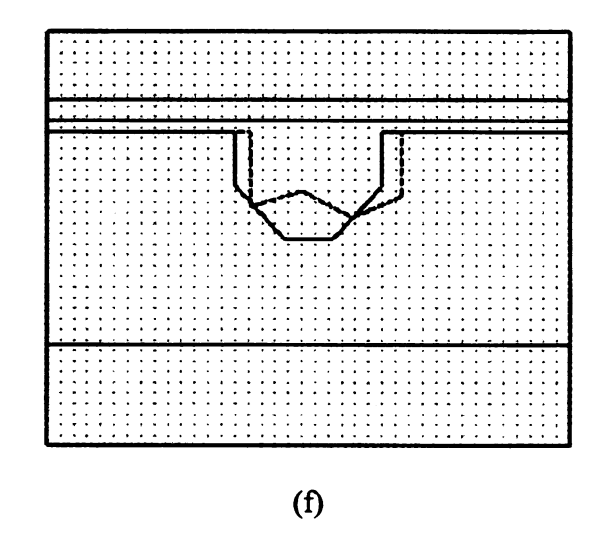


Figure 6.19 continued



### 6.4.4 Conclusion

Model-based inversion technique using the EFG numerical forward model is presented for a 2D problem. The updating scheme using gradient search in conjunction with adjoint equation method is developed for the EFG model. In the iteration procedure only the few coordinates that define the defect profile are updated while the overall background nodes remain unchanged, which simplifies the solution procedure and saves computational time. The gradient search method is a fast and reliable and the results show its robustness in the presence of noise.

# CHAPTER 7. 3D INVERSE PROBLEM USING EFG METHOD

#### 7.1 Introduction

Chapter 6 discussed the development and implementation of several inversion schemes for 1D and 2D defect characterization. However in practice, problems are generally 3D in space, which means that the solution domain and defects are represented in the x-, y-, and z- directions. The high-dimensionality is a major challenge for the inversion scheme [65]-[69]. The defect must be represented by 3D defect parameters, for example, the length, width, and height, which will make the defect reconstruction involve large number of unknowns and hence more complex. The high-dimensional inverse problem is in general ill-posed, since the measured signals lack the continuous and reliable dependence on the defect profiles and also the results can be non-unique.

In this chapter, the three dimensional inverse problem is addressed by modifying the 2D state space search method described in chapter 6. These modifications make it possible for 3D defect reconstruction. Both surface and subsurface defect reconstructions are presented for validation and discussion.

#### 7.2 Problem Statement

Figure 7.1 (a) shows the 3D geometry of an infinite single layer conducting plate with a defect. The time-varying harmonic current in the y-direction is applied using a thin foil as the excitation source. Figure 7.1 (b) is the 2D top view of the defect profile, which is a rectangular shaped surface breaking defect. Figure 7.1 (c) is the cross-section view of the defect profile. As defined before, a subsurface defect can also be modeled when the defect initiates from the bottom layer of the plate.

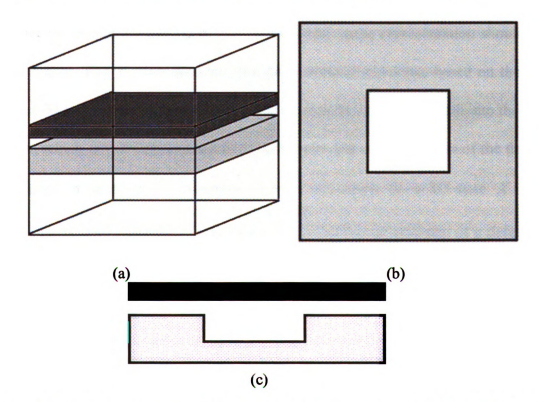


Figure 7.1 The model geometry (a) 3D view, (b) 2D top view and (c) cross-section view

The following parameters are used in the forward model:

- (1) the thickness of the aluminum plate: 4 mm
- (2) the profile of the ideal defect: 3 mm × 3 mm, with depth of 3 mm

- (3) the excitation current density:  $10^8 \text{ A/m}^2$
- (4) the excitation current frequency: 3 kHz
- (5) the solution domain:  $[-15, 15] \text{ mm} \times [-15, 15] \text{ mm} \times [-8, 8] \text{ mm}$
- (6) the sensor thickness: 0.2 mm; liftoff: 0.5 mm

The EFG method is used as forward model to obtain the discrete solution domain.

# 7.3 3D State Space Representation

In order to reconstruct the 3D defect, the 3D state space representation should be first developed. This section describes the three dimensional states based on the 2D definition. The defect is discretized into L layers of nodes along the depth into the test specimen, which is in z - direction; and in each layer, the surface profile of the defect is discretized in terms of M×N discrete cells in xy - plane. So a 3D state X is a M×N×L matrix with element 1 or 0, representing absence or presence of a defect in the corresponding cell, respectively.

The state space now consists of (2<sup>MNL</sup>) possible states.

For simplification we consider a profile of the rectangular defect in Figure 7.1 represented by a  $3\times3$  matrix in xy- plane, and 4 layers of nodes along the depth in z-direction.

For the 3D defect reconstruction, instead of the line plot, the 2D image of the normal component of magnetic flux density  $B_z$ , which is observed at sensor liftoff 0.5 mm, is used in calculating the cost function. Experimental measurements of the

real, and imaginary values of  $B_z$  signals can be obtained from the GMR system. In this thesis however, the input signal from the true defect is simulated using the forward EFG model.

The cost function is defined to search for the best defect profile, which is:

$$F = \sum_{m=1}^{K1} \sum_{n=1}^{K2} |B_{mn} - B_{mmn}|^2$$
(7.1)

where  $B_{mn}$  is the model prediction of the normal component of magnetic flux,  $B_{mmn}$  is the corresponding experimental signal and K1, K2 are the number of signal points in the x- and y-direction in the raster scan. The cost function is computed for all the possible states of all layers, and the defect corresponding to the lowest cost function is selected as the objective defect.

#### 7.4 Search Procedure

The search procedure is based on the same criterion as the tree search explained in the Figure 6.7. Since the total number of state (2<sup>MNL</sup>) is large, to avoid the tedious exhaustive search, the search is constrained based on the following assumptions: (a) the defect grows vertically downwards; (b) the surface defect profile is in a squared region; (c) the defect grows narrower with depth.

The search procedure is performed layer by layer in z-direction; at each layer, the 3×3 node is expanded to generate the different profiles allowed by the assumption. In

order to reduce expansion into all the 2<sup>9</sup> possible nodes a simplification is introduced as illustrated in Figure 7.2.

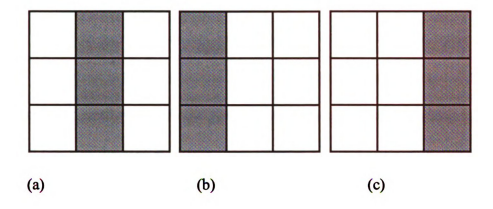


Figure 7.2 3×3 state space in each layer with three sub-state space

In the first layer, the search starts from the "middle defect" as shown in Figure 7.2 (a), which can be one of six possible defect profiles as shown in Figure 7.3 from (a) to (f). The optimum defect profile is selected as the one that minimizes the cost function.

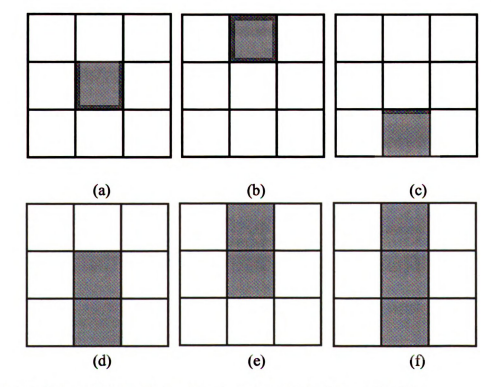


Figure 7.3 The candidate state space for sub-state in Figure 7.2 (a)

Once the optimum defect from the "middle defect" is estimated, then connected cells from the "left" and "right" defects corresponding to minimum cost function value are added to grow the defect in the current layer. When the optimum defect profile at the current layer is estimated, the search procedure is repeated with the cells in the next layer, until we reach the global minimum cost function which corresponds to the leaf node in the tree structure. The desired defect profile is reconstructed and the search stops.

#### 7.5 The Detailed Search Procedure

The detailed search procedure is divided into the following steps:

1. Estimation of the initial state d<sup>(0)</sup>;

This step involves determining whether defect location is on the top or bottom surface.

In the case of the 2D defect a simple peak detection algorithm on the data (imaginary part of  $B_z$ ) is used to determine the defect location and the peak-to-peak separation in the input signal is used to estimate the defect region in the initial layer. In the 3D inversion scheme, the peak-to-peak separation in the imaginary part of  $B_z$  is seen to vary with frequency whereas the real part is constant for both surface and subsurface defects. Figure 7.4 (a) and Figure 7.4 (b) show the estimated defect region

when the frequency is varied from 500 Hz to 5000 Hz for surface and subsurface defects.

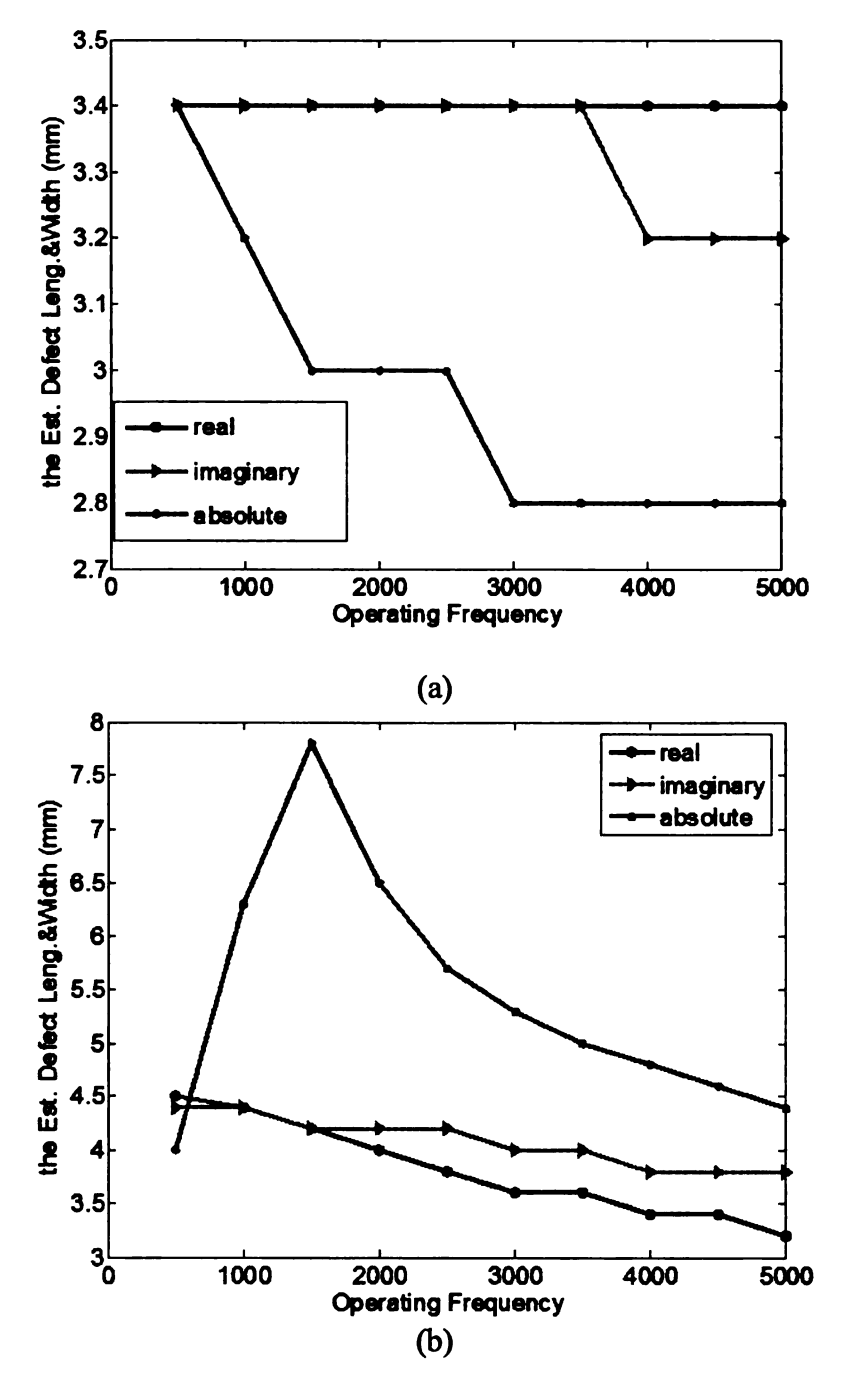


Figure 7.4 Plot of estimated defect region using real, imaginary and absolute data,
(a) surface defect, (b) subsurface defect

The initial node for the tree search (top or bottom) was therefore determined using real part of  $B_z$ . When the operating frequency is 3000 Hz, the defect region of the initial state is 3.4 mm × 3.4 mm for surface defect and 3.6 mm × 3.6 mm for the subsurface defect. Then the estimated defect region is divided into  $3\times3$  state space in equal size cells. Both the initial defects,  $d^{(0)}$  surface and  $d^{(0)}$  subsurface are modeled, the signals and corresponding cost functions are generated and node with lower cost function chosen as  $d^{(0)}$  determines if the defect to be reconstructed is top surface or bottom surface defect.

#### 2. Profiling the defect depth

Perform the search procedure in each layer. Generate the possible allowed defect shapes in current layer (expand the tree node) using the defect assumptions and compute the associated cost function using the forward model prediction and measured signal. The defect boundary corresponding to the minimum cost function is selected to be expanded in the next level.

# 3. Checking for stopping criteria

If the minimum cost function in a layer is larger than the corresponding minimum cost function in the layer above it the search stops. The geometry with the global minimum cost function provides the desired defect profile or is the solution to the inverse problem.

#### 7.6 Initial Results

The inversion strategy is implemented on two defect profiles. First, the  $3\times3\times3$  mm surface defect is assumed to be the true defect as shown in Figure 7.1, and the operating frequency is 3000 Hz. The measured signal is obtained for the true defect profile by simulating the EFG forward model and the corresponding real and imaginary part of Bz are shown in Figure 7.5.

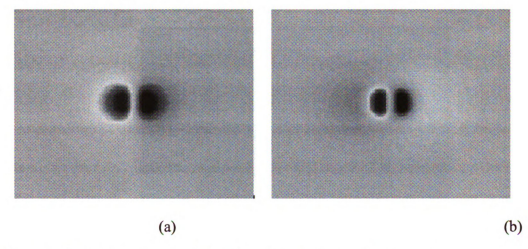


Figure 7.5 The ideal signal of Bz (a) real part (b) imaginary part

The real part of  $B_z$  is used to estimate the defect boundary in the initial layer and the imaginary part of  $B_z$  is used to calculate the cost function for minimization.

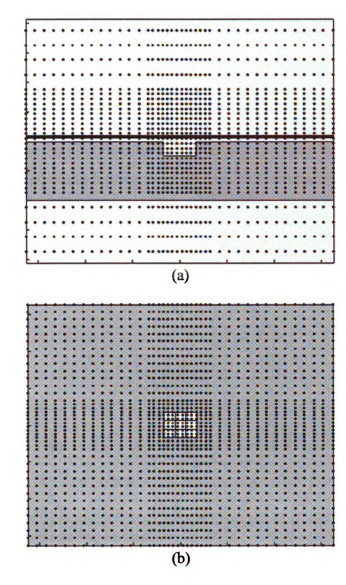


Figure 7.6 Initial guess of a top surface defect (a) cross-section view (b) top view

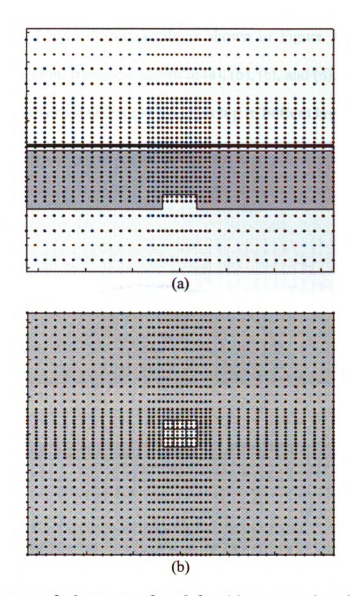


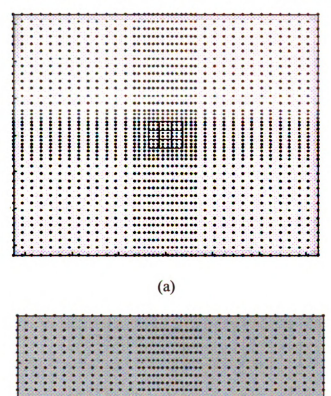
Figure 7.7 Initial guess of a bottom surface defect (a) cross-section view (b) top view

Top surface defect - Using the peak-to-peak distance to estimate the initial state, a top surface defect of size  $3.4 \text{ mm} \times 3.4 \text{ mm}$  and bottom surface defect, of size  $3.6 \text{ mm} \times 3.6 \text{ mm}$  as shown in Figure 7.6 (a) and (b) and Fig. 7.7 (a) and (b) respectively were simulated.

The cost function of top surface defect was 0.2569 whereas the cost function of the bottom surface defect was 0.5251. This led  $d^{(0)}$  to be a top surface defect.

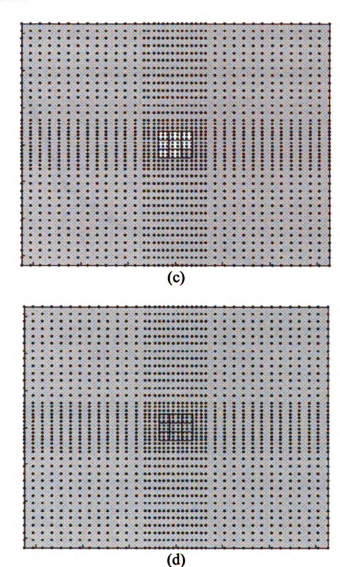
The reconstructed 4-layer defect profile is shown in Figure 7.8 and the defect profiles from top to bottom layers are shown in (a), (b), (c), and (d), respectively.

Figure 7.8 The reconstructed defect profile from top to bottom layer



(b)

Figure 7.8 continued



The minimum cost function nodes in each layer and the associated cost functions are plotted in Figure 7.9. The x-axis represents the all the intermediate nodes obtained from considering "middle", "left" and "right" states shown in Figure 7.2.

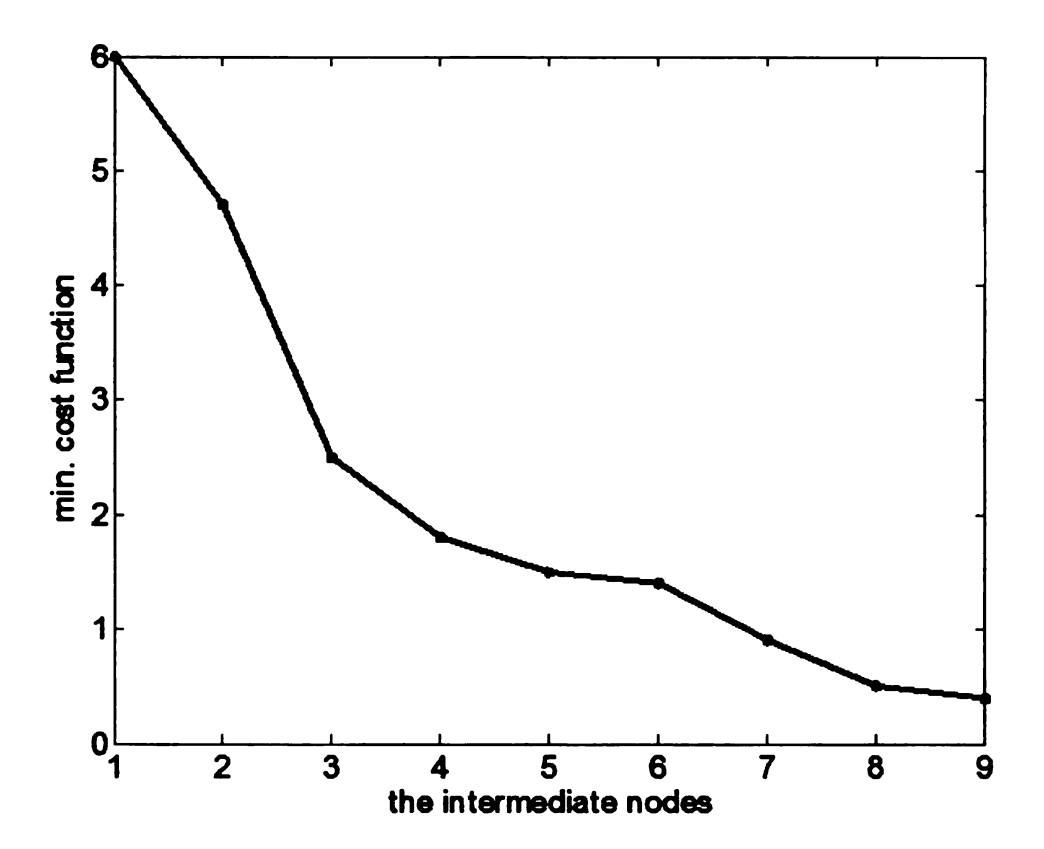


Figure 7.9 The cost function vs. node

Similar results for bottom surface defect are obtained. The true defect is a  $3 \times 3 \times 3$  mm subsurface defect. The operating frequency is 3000 Hz. The initial defect profile is determined as a bottom surface defect using a minimum of two cost functions corresponding to top surface and bottom surface defects respectively. The defect size corresponding to the initial node is node is 3.6 mm  $\times$  3.6 mm.

The reconstructed 4-layer defect profile is shown in Figure 7.10 and the defect profiles from bottom to top layers are shown in (a), (b), (c), and (d), respectively.

Figure 7.10 The reconstructed defect profile from bottom to top layer

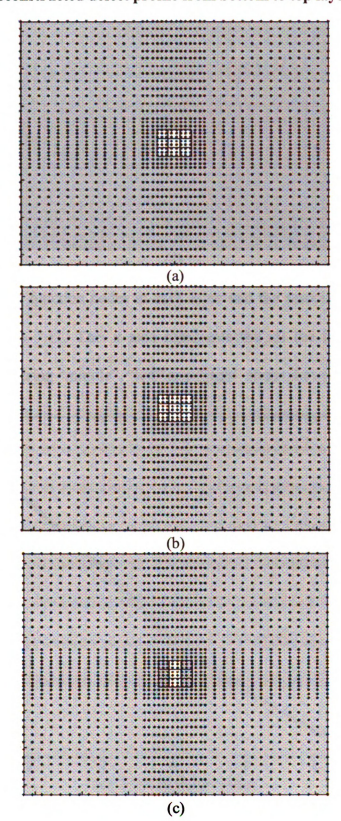
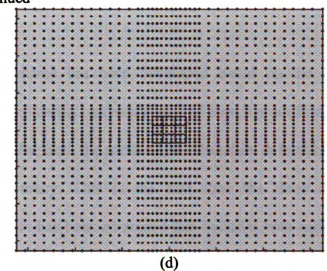


Figure 7.10 continued



The minimum cost function nodes in each layer and the associated cost functions are plotted in Figure 7.11. The x-axis represents the all the intermediate nodes obtained from considering "middle", "left" and "right" states shown in Figure 7.2.

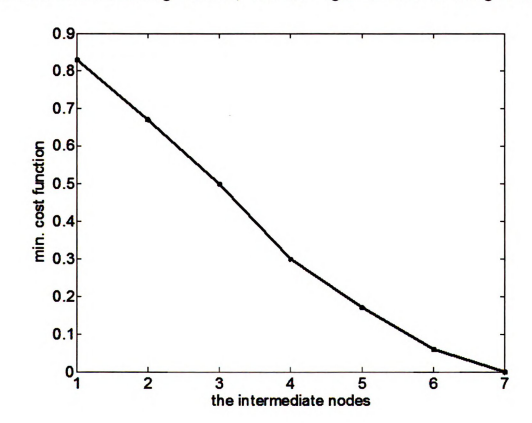


Figure 7.11 The cost function vs. node

# 7.7 Conclusion

A 3D inversion scheme has been developed based on the state space search algorithm. The detailed defect representation and search procedure are addressed with initial validation results. Both the surface and subsurface defects can be reconstructed with reasonable accuracy. This is the first time the three dimensional defect reconstruction problem has been attempted that includes both surface and subsurface defects. However, a lot of work remains to be done to optimize the parameters of different steps involved in the overall procedure.

# CHAPTER 8. CONCLUSIONS AND FUTURE WORK

# 8.1 Original Contributions to the Field

An accurate and efficient numerical forward using the element free Galerkin method has been developed, validated and applied to real 3D airframe geometry. The forward model has been used to understand the underlying physics and visualize the induced eddy currents in the case of different defect geometries. Development of model based strategies for signal inversion to reconstruct the defect profile in electromagnetic NDE is the primary objective of this dissertation.

The research carried out during the course of the dissertation has made the following contributions to the field:

- (1). The development and improvement of the Element-Free Galerkin (EFG) method for electromagnetic field computations. The improvements include the asymmetric domain of influence, the orthogonal basis function, and the Penalty boundary condition. 1D, 2D, and 3D models for Poisson equation and diffusion equation, describing static or low frequency quasi-static problems, have been presented as examples to illustrate the validity and effectiveness of EFG method. This method is shown to be better suited for modeling the complex solution domain compared with the traditional mesh-based methods.
- (2). The use of EFG method in signal inversion has also been investigated and applied to reconstructing various one and two dimensional defect profiles by means of

parametric and non parametric inversion schemes. An iterative parametric algorithm for one dimensional tight crack reconstruction was demonstrated. Two iterative nonparametric algorithms are proposed, namely a state space search method and an adjoint based gradient minimization method. These algorithms been validated and perform with excellent accuracy in the prediction of the length and depth profile of defects.

(3). The state space search method is modified and used in the three dimensional defect reconstruction. These modified state space search scheme are fast and efficient and avoid the tedious exhaustive search procedure without compromising the performance. Both the surface and subsurface defects can be reconstructed with acceptable accuracy.

#### 8.2 Future Work

This dissertation addresses the inverse problem of predicting the defect profiles using simulated signals using different approaches. However, the application to inversion of experimental signals needs to be carried out.

Future work includes:

(1). Validation of the inversion schemes using the experimental Giant Magneto-resistance data. Signal pre-processing may be needed before the data can be used for inversion. Several experimental parameters need to be considered, such as the GMR sensor bias, the effect of the scanning liftoff, the GMR sensor characteristics to map the voltage signal back to the magnetic flux density fields.

More rigorous study of the cost function must be carried out to control the accuracy of the solution.

- (2). Inverse algorithms in this work are developed for the case of a single defect. The possibility of multiple defects in practice, which are close to each other, will be more challenging and needs to be addressed. This is left as a future work to investigate the physical interaction of fields due to multiple defects.
- (3). The inversion scheme needs to be optimized in each stage to improve the efficiency for online processing after the inspection is completed.

## REFERENCES

- [1] D. E. Bray and R. K. Stanley, Nondestructive Evaluation, McGraw Hill, 1989
- [2] R. B. Thompson and D. O. Thompson, "Ultrasonics in Nondestructive Evaluation", Proceedings of the IEEE, Vol. 73, No. 12, Dec 1985
- [3] D. E. Bray and R. K. Stanley, Nondestructive Evaluation, a Tool for Design, Manufacturing, and Service, McGraw-Hill, 1989
- [4] B. Yang, P. K. Liaw, H. Wang, J. Y. Huang, R. C. Kuo, and J. G. Huang, Thermography: A New Nondestructive Evaluation Method in Fatigue Damage, JOM, 2003
- [5] R. Pradeep, "Neural Network Based Iterative Approaches for Electromagnetic NDE", Ph.D Dissertation, Iowa State University, 2001
- [6] J. Benson, Automated Analysis of Rotating Probe Eddy Current Data, Interim Report, Dec. 2003
- [7] S. Udpa and L. Udpa, "Eddy Current Nondestructive Evaluation", Encyclopedia of Electrical and Electronics Engineering, John G. Webster, Editor, John Wiley, 1999
- [8] C. Chen, "Finite Element Modeling of MOI for NDE Applications", Master Thesis, Iowa State University, 2000
- [9] J. D. Jackson, Classical Electrodynamics, John Wiley & Sons Inc, New York, 1998
- [10] L. Udpa and S. S. Udpa, "Application of Signal Processing and Pattern Recognition Techniques to Inverse Problems in NDE", International Journal of Applied Electromagnetics and Mechanics, Vol. 8, pp. 99-117, 1997
- [11] M. Yan, M. Afzal, S. S. Udpa, S. Mandayam, Y. Sun, L. Udpa, and P. Sacks, "Iterative Algorithms for Electromagnetic NDE Signal Inversion", ENDE' 97, Reggio Calabria, Italy, Sep. 1997
- [12] S. Hoole, S. Subramaniam, R. Saldanha, J. Coulomb, and J. Sabonnadiere, "Inverse Problem Methodology and Finite Elements in the Identification of Cracks, Sources, Materials and their Geometry in Inaccessible Locations", IEEE Transactions on Magnetics, Vol. 27, No. 3, 1991
- [13] H. A. Sabbagh, L. D. Sabbagh, and T. M. Roberts, "An Eddy-Current Model and

- Algorithm for Three-dimensional Nondestructive Evaluation of Advanced Composites", IEEE Transactions on Magnetics, Vol. 24, No. 6, pp. 3201-3212, Nov. 1988
- [14] Jacques Hadamard, Princeton University Bulletin, pp. 49-52
- [15] Satish Udpa, "Handbook on Electromagnetic NDE Methods"
- [16] J. Salon and J. Schneider, "A Comparison of Boundary Integral and Finite Element Formulations of the Eddy Current Problems", IEEE Transactions on Power Systems, Vol. 100, pp. 1473-1479, 1981
- [17] Nathan Ida, Numerical Modeling for Electromagnetic Non-Destructive Evaluation, Chapman & Hall, McGraw Hill, 1984
- [18] Oliver Rübenkönig, The Finite Difference Method (FDM)-An Introduction, Albert Ludwigs University of Freiburg, 2006
- [19] J. H. Hwang and W. Lord, "Finite Element Modeling of Magnetic Field/Defect Interactions", ASNT Journal of Testing and Evaluation, Vol. 3, No. 1, pp 21-25, 1975
- [20] J. H. Hwang and W. Lord, "Magnetic Leakage Field Signatures of Material Discontinuities", Proceedings of the 10<sup>th</sup> Symposium on NDE, San Antonio, Texas, 1975
- [21] W. C. Yen, "Finite Element Characterization of Residual Leakage Fields", Master Thesis, Colorado State University, 1978
- [22] K. Ishibashi, "Nonlinear Eddy Current Analysis by the Integral Equation Method", IEEE Transactions of Magnetics, Vol. 30, No. 5, Sep. 1994
- [23] N. Esposito et al, "Modeling of Three-Dimensional Nonlinear Eddy Current Problems with Conductors in Motion by an Integral Formulation", IEEE Transactions on Magnetics, Vol. 32, No. 3, May 1996
- [24] J. R. Bowler, Y. Yoshida, and N. Harfield, "Vector-Potential Boundary-Integral Evaluation of Eddy-Current Interaction with a Crack", IEEE Transactions on Magnetics, Vol. 33, No. 5, Sep. 1997
- [25] Y. Yoshida and J. R. Bowler, "Vector Potential Integral Formulation for Eddy-Current Probe Response to Cracks", IEEE Transactions on Magnetics, Vol. 36, No. 2, Mar. 2000
- [26] T. Belytschko, Y. Krongauz, D. Organ, M. Fleming, and P. Krysl, "Meshless Methods: An Overview and Recent Developments", Computer Methods in Applied Mechanics and Engineering, Vol. 139, Issues 1-4, pp. 3-47, 1996

- [27] R. A. Gingold and J. J. Monaghan, "Smoothed Particle Hydrodynamics: Theory and Application to Non-spherical Stars", Royal Astronomical Society, Monthly Notices, Vol. 181, pp. 375-389, Nov. 1977
- [28] B. Nayroles1, G. Touzot, and P. Villon, "Generalizing the Finite Element Method: Diffuse Approximation and Diffuse Elements", Computational Mechanics, Vol. 10, No. 5, pp. 307-318, Sep. 1992
- [29] W. K. Liu, Y. Chen, S. Jun, J. S. Chen, T. Belytschko, C. Pan, R. A. Uras, and C. T. Chang, "Overview and Applications of the Reproducing Kernel Particle Methods", Archives of Computational Methods in Engineering, Vol. 3, No. 1, pp. 3-80, Mar. 1996
- [30] J. M. Melenk and I. Babuska, "The Partition of Unity Finite Element Method: Basic Theory and Applications", Computer Methods in Applied Mechanics and Engineering, Vol. 139, Issues 1-4, pp. 289-314, Dec. 1996
- [31] C. A. M. Duarte and J. T. Oden, "Hp Clouds-an Hp Meshless Method", Numerical Methods for Partial Differential Equations, Vol. 12, pp. 673-705, 1996
- [32] N. Sukumar, B. Moran, and T. Belytschko, "The Natural Element Method in Solid Mechanics", International Journal for Numerical Methods in Engineering, Vol. 43, No. 5, pp. 839-887, Nov. 1998
- [33] H. Wendland, "Meshless Galerkin Methods using Radial Basis Functions", Mathematics of Computation, Vol. 68, No. 228, pp. 1521-1531, 1999
- [34] T. Belytschko, Y. Y. Lu, and L. Gu, "Element-Free Galerkin methods", International Journal for Numerical Methods in Engineering, Vol. 37, pp. 229-256, 1994
- [35] J. Dolbow and T. Belytschko, "An Introduction to Programming the Meshless Element Free Galerkin Method", Archives in Computational Mechanics, Vol. 5, No. 3, pp. 207-241, 1998
- [36] V. Cingoski, N. Miyamoto, and H. Yamashita, "Element-free Galerkin Method for Electromagnetic Field Computations", IEEE Transactions on Magnetics, Vol. 34, No. 5, pp. 3236–3239, 1998
- [37] S. A. Viana and R. C. Mesquita, "Moving Least Square Reproducing Kernel Method for Electromagnetic Field Computation", IEEE Transactions on Magnetics, Vol. 35, No. 3, pp. 1372–1375, 1999
- [38] S. L. Ho, S. Yang, J. M. Machado, and H. C. Wong, "Applications of a Meshless Method in Electromagnetics", IEEE Transactions on Magnetics, Vol. 37, No. 5, pp. 3198–3202, 2001

- [39] L. Xuan, Z. Zeng, B. Shanker, and L. Udpa, "Element-free Galerkin Method for Static and Quasi-Static Electromagnetic Field Computation", IEEE Transactions on Magnetics, Vol. 40, No. 1, pp. 12-20, Jan. 2004
- [40] Liang Xuan, "Finite Element and Meshless Methods in NDT Applications", Ph. D Dissertation, Iowa State University, 2002
- [41] S. Liu, Q. Yang, H, Chen, G. Xu, and F. Liu, "Improvement of the Element -Free Galerkin Method for Electromagnetic Field Calculation", IEEE Transactions on Applied Superconductor, Vol. 14, No. 2, pp. 1866-1869, Jun. 2004
- [42] Y. Zhang, K. R. Shao, D. X. Xie, and J. D. Lavers, "Meshless Method Based on Orthogonal Basis for Computational Electromagnetics", IEEE Transactions on Magnetics, Vol. 41, No. 5, pp. 1432-1435, May 2005
- [43] Suzhen Liu, Qingxin Yang, Haiyan Chen, Guizhi Xu, and Fugui Liu, "Improvement of the Element-Free Galerkin Method for Electromagnetic Field Calculation", IEEE Transactions on Applied Superconductivity, Vol. 14, No. 2, pp. 1866-1869, Jun. 2004
- [44] C. Herault and Y. Marechal, "Boundary and Interface Conditions in Meshless Methods", IEEE Transactions on Magnetics, Vol. 35, No. 4, pp. 1450-1453, 1999
- [45] T. Belytschko, D. Organ, and Y.Krongauz, "A Coupled Finite Element—Free Galerkin Method", Computational Mathematics, Vol. 17, pp. 186-195, 1995
- [46] W. M. Xue and S. N. Atluri, "Hybrid and Mixed Finite Element Methods", Proceedings of the Winter Annual Meeting, Miami Beach, FL, pp. 91-112, Nov. 1985
- [47] T. Belytschko and Y. Krongauz, "Enforcement of Essential Boundary Conditions in Meshless Approximations using Finite Elements", Computer Methods in Applied Mechanics and Engineering, Vol. 131, pp. 133-145, 1996
- [48] G. Yagawa and T. Furukawa, "Recent Developments of Free Mesh Method", International Journal for Numerical Methods in Engineering, 47, No.2, pp. 1419-1443, 2000
- [49] G. L. Fitzpatrick, D. K. Thome, R. L. Skaugset, E. Y. C. Shih, and W. C. L. Shih, "Magneto-Optic/Eddy Current Imaging of Aging Aircraft: A New NDI Technique", Material Evaluation, Vol. 51, No. 12, pp. 1402-1407, Dec. 1993
- [50] L. Xuan, B. Shanker, L. Udpa, W. C. L. Shih, and G. L. Fitzpatrick, "Finite Element Model for MOI Applications Using A-V Formulation", Review of Progress in Quantitative Nondestructive Evaluation, AIP, Vol. 557(1), pp. 385-391, Apr. 2001
- [51] G. Rubinacci, A. Tamburrino, A. Ventre, F. Villone, L. Udpa, L. Xuan, and Z.

- Zeng, "Numerical Simulation of Magneto-Optic Eddy Current Imaging", 8<sup>th</sup> International Workship on Electromagnetic Nondestructive Evaluations, Saarbrucken, Germany, Jun. 2001
- [52] R. Albanese et al, "A Comparative Study of Finite Element Models for Magneto Optic Imaging Applications", 6<sup>th</sup> International Workshop on Electromagnetic Nondestructive Evaluations, Budapest, Hungary, Jun. 2000
- [53] R. W. Freund, "Transpose-Free Quasi-Minimal Residual Methods for Non-Hermitian Linear Systems," Advances in Computer Methods for Partial Differential Equations, pp. 258-264, IMACS, 1992
- [54] L. Udpa, R. Pradeep, J, Benson, and S. Udpa, "Automated Analysis of Eddy Current Signals in Steam Generator Tube Inspection," 16<sup>th</sup> World Conference on Nondestructive Evaluation
- [55] R. Sikora, J. Sikora, E. Cardelli, and T. Chady, "Artificial Neural Network Application for Material Evaluation by Electromagnetic Methods", Proceedings of the International Joint Conference on Neural Networks, Vol. 6, pp. 4027-4032, 1999
- [56] W. Qing, S. Xueqin, Y. Qingxin, and Y. Weili, "Using Wavelet Neural Networks for the Optimal Design of Electromagnetic Devices", IEEE Transactions on Magnetics, Vol. 33, No. 2, pp. 1928-1930, Mar. 1997
- [57] S. Hoole, "Artificial Neural Networks in the Solution of Inverse Electromagnetic Field Problems", IEEE Transactions on Magnetics, Vol. 29, pp. 1931-1934, 1993
- [58] R. Popa, and K. Miya, "A Data Processing and Neural Network Approach for Inverse Problems in ECT", ENDE, R. Albanese et al. eds., IOS Press, pp. 297-305, 1998
- [59] R. Sikora, T. Chady, and J. Sikora, "Neural Network Approach to Crack Identification", International Journal of Applied Electromagnetics and Mechanics, Vol. 9, pp. 391-398, 1997
- [60] Yue Li, "Edge Based Finite Element Simulation of Eddy Current Phenomenon and its Application to Defect Characterization", Ph. D Dissertation, Iowa State University, 2001
- [61] Guizhong Liu, Yue Li, Y. Sun, P. Sacks, and S. Udpa, "An Iterative Algorithm for Eddy Current Inversion", Review of Progress in Quantitative Nondestructive Evaluation, Vol. 19(A), pp. 497-504
- [62] L. Udpa, "An Iterative Numerical Algorithm for the Inversion of Eddy Current NDT Data", Electrosoft, Vol. 2, No. 23, 1991

- [63] L. Upda and W. Lord, "A Search-Based Imaging System for Electromagnetic Nondestructive Testing", Expert, IEEE, Vol. 4, Issue 4, pp. 18-26, 1989
- [64] M. Gunzburger, "Adjoint Equation based Methods for Control Problems in Incompressible Viscous Flows", Design Optimal et MDO, Center de Recherche en Calcul Applique, Montreal, pp. 1-25, 1998
- [65] Y. Li, L. Udpa, and S. S. Udpa, "Three-Dimensional Defect Reconstruction from Eddy Current NDE Signals", IEEE Transactions on Magnetics, Vol. 40, Issue 2, pp. 410-417, 2004
- [66] P. Ramuhalli, L. Udpa, and S. S. Udpa, "Electromagnetic NDE signal inversion by function-approximation neural networks", IEEE Transactions on Magnetics, Vol. 38, Issue 6, pp. 3633-3642, 2002
- [67] S. M. Nair and J. H. Rose, "Reconstruction of Three-Dimensional Conductivity Variations from Eddy Current (Electromagnetic Induction) Data", Inverse Problems 6, pp. 1007-1030, 1990
- [68] A. Tamburrino, R. Fresa, S. S. Udpa, and Y. Tian, "Three-Dimensional Defect Localization from Time-of-Flight/Eddy Current Testing Data", IEEE Transactions on Magnetics, Vol. 40, Issue 2, pp. 1148-1151, 2004
- [69] A. Joshi, L. Udpa, and S. S. Udpa, "Use of Radial Basis Function Neural Network to Predict 3-Dimensional Depth Profile from Magnetic Flux Leakage Inspection", National Seminar on NDT by Indian Society of Nondestructive Testing (ISNT), Dec. 20

